Simulations on an angular-selective photoelectron source and on an active transverse energy filter for the KATRIN experiment

Master's Thesis

Richard W. J. Salomon

Westfälische Wilhelms-Universität Münster
Institut für Kernphysik
AG Weinheimer

First Referee: Prof. Dr. Christian Weinheimer
Second Referee: Prof. Dr. Anton Andronic

Münster, April 19, 2022

Eidesstattliche Erklärung

Hiermit versichere ich, *Richard Wilhelm Julius Salomon*, dass ich die vorliegende Arbeit selbstständig verfasst und keine anderen als die angegebenen Quellen und Hilfsmittel verwendet habe. Gedanklich, inhaltlich oder wörtlich Übernommenes habe ich durch Angabe von Herkunft und Text oder Anmerkung belegt bzw. kenntlich gemacht. Dies gilt in gleicher Weise für Bilder, Tabellen, Zeichnungen und Skizzen, die nicht von mir selbst erstellt wurden.

Münster, 19. April 2022

Richard Wilhelm Julius Salomon

Contents

1 Introduction

Although the postulation of the neutrino by W. Pauli [Pau64] dates back more than 90 years, the determination of the fundamental properties of this elementary particle remains one of the most difficult tasks of modern physics. Being the most abundant discovered particle in the universe, neutrinos could provide information about important cosmological events such as early structure formation. Several Nobel Prizes have been awarded to scientists in the field of neutrino physics, such as Frederick Reines for the first experimental observation [Nob95] in 1995 or, most recently, Arthur B. McDonald and Takaaki Kajita for the discovery of neutrino oscillations [Nob15]. The latter phenomenon shows that neutrinos possess a non-zero mass, which contradicts early predictions of the Standard Model of particle physics. Despite numerous collaborative efforts using different approaches, the absolute neutrino mass is yet to be measured.

The Karlsruhe Tritium Neutrino Experiment (KATRIN) aims at determining the electron neutrino mass with a sensitivity of 0.2 eV/c^2 (90% C.L.) from a precision measurement of the tritium β-decay spectrum [Ang+05]. Its world-leading model-independent approach recently set a new upper limit on the neutrino mass of [KAT22]

$$m(\nu) < 0.8\,\mathrm{eV/c^2} \qquad (90\,\%\ \mathrm{C.L.}),$$

which significantly improves the results of its predecessor experiments Mainz and Troitsk [Kra+05; Ase+11]. To achieve the sensitivity goal, a thorough understanding and minimization of its background components as well as its systematic uncertainties is required. The goal of this thesis is to support the development of two crucial technologies that aim at improving KATRIN's sensitivity.

One of the leading systematic uncertainties is connected to inelastic electron scattering inside the tritium source [Mac20]. To investigate the energy loss function at energies up to 32 keV a new electron source, which is able to sustain the required voltages, has been developed and commissioning measurements were performed. The measurement environment with an off-axis detector required a shift of the electron beam via non-axial magnetic fields. Hence, in

this thesis particle tracking simulations are presented to support the evidence of the functionality of the electron source as well as understand the impact of the altered electromagnetic field configuration.

In contrast to this, one of the dominant backgrounds identified at KATRIN is the ionization of highly-excited Rydberg atoms inside the main spectrometer [Frä+22; Tro18]. As the electrons emitted by ionized Rydberg atoms - in contrast to most signal electrons from tritium β-decay - possess only a small transverse momentum relative to the magnetic guiding field, an angular-selective detector might be able to distinguish between this specific background and actual signal. In order to test this novel detection technique, active transverse energy filter (aTEF) prototypes consisting of microstructured Si p-i-n diodes are investigated in a test setup in Münster. This thesis focuses on the accompanying particle tracking simulations which are not only essential for the analysis and interpretation of measurement data but also help to optimize the setup.

The thesis is structured as follows:
Chapter 2 gives an introduction to neutrino physics, discussing selected experiments and motivating the KATRIN experiment. The KATRIN experiment and important related concepts are introduced in chapter 3. The simulation software Kassiopeia, as well as the used configurations, are presented in chapter 4. With this as basis, particle tracking simulations regarding the commissioning measurements of the new electron source and the test setup for the diode prototypes are shown in chapters 5 and 6. Eventually, chapter 7 concludes the thesis and gives an outlook.

2 Neutrino Physics

The theoretical description of neutrinos remains an active field of research. Despite nearing a century since the particle's postulation in the 1930's, basic properties such as the hierarchy of mass states and the absolute mass scale are still left to be observed. This chapter shall give a brief introduction to the history of neutrino physics, including the theoretical concept and important experimental observations.
Therefore, section 2.1 discusses the experimental discovery of the three neutrino flavors. Section 2.2, presents the concept of neutrino oscillation, which implies that neutrinos possess a non-zero mass. Hence, section 2.3 introduces different concepts to experimentally determine the neutrino mass.

2.1 Postulation and experimental discovery

Having been familiar with the discrete spectra following α- and γ-decays, the observation of a continuous energy spectrum of electrons resulting from a β-decay by J. Chadwick in 1914 [Cha14] was a surprise at first. As only an electron and the corresponding daughter nucleus of the decay was detectable, the β-decay was also considered to be a two-body decay. This supposition, however, was not reconcilable with the measured spectra, as it would violate the conservation of energy.
To solve this mystery, Wolfgang Pauli proposed in 1930 [Pau64] the existence of an additional particle taking part in the β-decay. Enrico Fermi adopted this idea and later formulated the "Fermi theory of beta decay" [Fer34] in which he also manifested the name "neutrino".
Due to the small interaction cross-section of the neutrino, the first experimental confirmation of its existence came only in 1956 with the Reines-Cowan neutrino experiment [RC53]. Here, the very distinct signature of the inverse beta decay

$$\bar{\nu} + p \rightarrow n + e^{+} \tag{2.1}$$

together with a large neutrino flux from a nuclear reactor was used. In more detail, the emitted positron annihilates quickly with a nearby electron, creating two gamma rays of

511 keV each in opposite directions. The neutron is (after moderation) captured by a cadmium atom from the surrounding scintillator material, which, in turn, releases an additional third photon. A coincidence between the two back-to-back emitted photons and the subsequent neutron capture decay photon made it possible to distinguish this rare process from background. Following the success of the experiment, Frederick Reines was awarded with the Nobel Prize in 1995.

The discovery of the neutrino built the foundation for a wide variety of experiments. Important for later discussion in this chapter are the experimental discoveries of the muon neutrino [Dan+62] as well as the tau neutrino [Kod+01], proving that there is more than one family of neutrinos.

In 1962 a group of scientists led by L. M. Lederman, M. Schwartz and J. Steinberger at the Brookhaven National Laboratory shot a proton beam at a beryllium target. The collisions produced a shower of pi-mesons, which decayed via

$$\pi^{\pm} \rightarrow \mu^{\pm} + (\nu_{\mu}/\bar{\nu}_{\mu}). \tag{2.2}$$

A 13 m thick steel shielding extracted the rarely interacting neutrinos from the particle shower. A few of the transmitted neutrinos then reacted with matter inside a spark chamber. The photographs of these interactions showed distinct particle tracks, indicating the production of muons rather than electrons, which would create electromagnetic showers, producing more particles in the process. The muon neutrino was discovered. The three scientists were awarded the Nobel Prize in 1988, not only due to their discovery, but also for being the first group to produce a high-energy neutrino beam.

With the discovery of the tau lepton in 1975 [Per+75] the existence of its associated neutrino was also postulated. However, it took until the year 2000 that its existence could be verified via direct measurement. The DONUT (Direct Observation of a Nu Tau) experiment at Fermilab [Kod+01] used a similar approach to the one used at Brookhaven, which involved an accelerator induced neutrino beam. A total of nine ν_{τ}-events were reported in the final publication in 2008 [Kod+08] confirming the existence of three neutrino families.

2.2 Neutrino oscillation

Knowing that neutrinos interact by inverse β-decay, another experiment was conducted at Brookhaven Laboratory between 1965 and 1967 with the goal of measuring the solar neutrino flux [Cle+98]. To minimize background by cosmic radiation, the experiment was based in the

Homestake mine, about 1500 m underground. It featured a 400.000 l tank of perchloroethylene making it possible to detect neutrinos via

$$\nu_e + {}^{37}\mathrm{Cl} \rightarrow {}^{37}\mathrm{Ar} + e^{-}. \tag{2.3}$$

A chlorine based experiment had many advantages, such as the affordability of the liquid as well as the noble gas characteristics of the produced Argon, which made it easy to extract. The Homestake experiment [Cle+98], however, found only a third of the predicted number of solar neutrinos. This result was confirmed by other radiochemical experiments, for instance Gallex in 1999 [Ham+99] and SAGE in 2009 [Abd+09]. The result became famous as the so-called "solar neutrino problem", which to this day, shapes our understanding of neutrinos. The emergence of water Cherenkov detectors was an important asset to the understanding of this phenomenon. In 1999, the Sudbury Neutrino Observatory (SNO) [Aha+13], a Cherenkov detector filled with 1000 t of heavy water (D_2O), began data taking. The usage of heavy water was particularly beneficial as the three interaction channels

$$\begin{aligned} \nu_x + e^{-} &\longrightarrow \nu_x + e^{-} && \text{(Elastic Scattering)}, \\ \nu_e + d &\longrightarrow p + p + e^{-} && \text{(Charged Current)}, \\ \nu_x + d &\longrightarrow \nu_x + p + n && \text{(Neutral Current)} \end{aligned}$$

enabled the detection of all neutrino flavors (ν_e, ν_μ, ν_τ).
The two important results from this experiment are, on the one hand, the good agreement with the data of the Homestake experiment and, on the other hand, the observed total neutrino flux matching the theoretical predictions. The latter was - in combination with our knowledge that muon and tau neutrinos are not produced in the sun - a confirmation of the longstanding theory of B. Pontecorvo [Pon58] in which he explains the possibility of neutrino oscillation.
This term implies that a neutrino emitted in a weak interaction with a particular flavor ν_i can be detected, carrying a different flavor ν_j. For this to happen neutrinos need to be massive particles, which propagate as mass eigenstates ν_1, ν_2 and ν_3. The relation between the two bases is described mathematically via the unitary Pontecorvo–Maki–Nakagawa–Sakata (PMNS) matrix [MNS62]

$$\begin{pmatrix} \nu_e \\ \nu_\mu \\ \nu_\tau \end{pmatrix} = \begin{pmatrix} U_{e1} & U_{e2} & U_{e3} \\ U_{\mu 1} & U_{\mu 2} & U_{\mu 3} \\ U_{\tau 1} & U_{\tau 2} & U_{\tau 3} \end{pmatrix} \cdot \begin{pmatrix} \nu_1 \\ \nu_2 \\ \nu_3 \end{pmatrix}. \tag{2.4}$$

Therefore, when a neutrino is created in a weak interaction process, its state can be described by the coherent linear superposition of mass eigenstates and, analogously, the time evolution of its wavefunction is given by the time evolution of the mass eigenstates [Tho13]. Consequently, it is reasonable to formulate the survival probability of a flavor eigenstate, where one finds exemplarily for the electron neutrino

$$\begin{aligned} P(\nu_e \to \nu_e) = 1 &- 4\,|U_{e1}|^2\,|U_{e2}|^2 \sin^2 \Delta_{21} \\ &- 4\,|U_{e1}|^2\,|U_{e3}|^2 \sin^2 \Delta_{31} \\ &- 4\,|U_{e2}|^2\,|U_{e3}|^2 \sin^2 \Delta_{32} \end{aligned} \tag{2.5}$$

with

$$\Delta_{ji} = \frac{\left(m_j^2 - m_i^2\right) L}{4E_\nu}, \tag{2.6}$$

where m_j and m_i are the masses of the corresponding mass eigenstates, L denotes the flight distance and E_ν is the kinetic energy of the neutrino. Here, it is also obvious that phase differences between the mass eigenstates only develop if $\Delta m_{ji} = m_j - m_i \neq 0$. It is thereby possible to measure - along with the other oscillation parameters of the PMNS matrix which shall not be covered here - the differences of the squared neutrino masses.

There are two different approaches to determining the PMNS matrix elements. Knowing the neutrino flux from the respective source, *appearance* experiments search for flavors which have not initially been present in the beam, while *disappearance* experiments are sensitive to the flavor that is emitted from the source. Important to note here is that the oscillation length depends on L/E_ν, thus the distance of the experiment to the neutrino source with respect to the neutrino energy determines whether it is sensitive to *appearance* or *disappearance*. Neutrino oscillation experiments can therefore be categorized by their neutrino source and distance. For example, short-baseline reactor experiments (e.g. Daya Bay [Lu+20]), operate at differences on the scale of $\mathcal{O}(1)\,\mathrm{km}$ and are sensitive to Δm^2_{32}, whereas long-baseline reactor experiments (e.g. KamLAND [Gan+11]), which are located at distances of $\mathcal{O}(100)\,\mathrm{km}$, are sensitive to Δm^2_{21}. Measurements of solar or atmospheric neutrinos, as well as neutrinos originating from accelerators, can also contribute to determining the mass splittings.

From these measurements emerge two possible mass orderings. In normal ordering (NO) one finds $m_3 > m_2 > m_1$ while the inverted ordering is $m_2 > m_1 > m_3$ (IO). The best fit values from a global fit of many oscillation experiments by de Salas et al. [Sal+21], published in 2020, are depicted in table 2.1.

Table 2.1: Best fit values of the neutrino mass splittings taken from [Sal+21].

parameter	best fit value $\pm 1\sigma$
Δm^2_{21}	$7.50^{+0.22}_{-0.20}\,10^{-5}\mathrm{eV}^2$
$\left\lvert\Delta m^2_{31}\right\rvert$ (NO)	$2.55^{+0.02}_{-0.03}\,10^{-3}\mathrm{eV}^2$
$\left\lvert\Delta m^2_{31}\right\rvert$ (IO)	$2.45^{+0.02}_{-0.03}\,10^{-3}\mathrm{eV}^2$

2.3 Neutrino mass experiments

Oscillation experiments described in section 2.2 are not able to measure the absolute mass scale of neutrinos and, thus, are not capable of investigating the neutrino mass hierarchy. However, these experiments give clear signs towards beyond the Standard Model physics (BSM). As neutrinos are the most abundant particle in the universe, knowledge of this property is key to understanding the fundamentals of our universe. In recent years, there have been several efforts to determine the absolute neutrino mass scale, yet so far only upper limits have been formulated.

One field that could give access to the neutrino mass is cosmology. Several experiments, such as the measurement of anisotropies in the power spectrum of the cosmic microwave background (CMB) suggest that neutrinos played an important role in the Big Bang, leaving for example an imprint in cosmic structure formation and a background radiation known as the cosmic neutrino background. Thus, data from cosmological observations are an important asset to extract and constrain numerous neutrino properties. A stringent constraint is given by the Planck collaboration with $\sum_i m_{\nu_i} < 0.12\,\mathrm{eV}$ [Agh+20]. A detailed discussion of cosmological neutrino mass constraints can be found in [Tan+18]. While these values lead a promising path to determining the absolute neutrino mass, they are also highly model-dependent.
A different approach towards measuring the neutrino mass given by the search for neutrinoless double-beta decay ($0\nu\beta\beta$) where a nucleus with atomic number Z and mass number A decays via

$$(Z, A) \rightarrow (Z + 2, A) + 2e^-. \tag{2.7}$$

This decay can only happen if two conditions are met. On the one hand, the neutrino needs to be a Majorana-particle, meaning that it is its own anti-particle, while, on the other hand, its helicity state needs to be able to change. The latter can only be possible, if the neutrino is a massive particle. Calculating the expected decay rate yields a dependency on the effective Majorana mass $\langle m_{\beta\beta}\rangle = \left|\sum_i U^2_{ei} m_i\right|$, thus, making this kind of measurement also sensitive to the absolute neutrino mass scale.

Until now, however, this decay has not been measured and only lower limits for $T_{1/2}$ have been given. As an example, the final results of the GERDA (Germanium Detector Array) experiment, which investigated the double-beta decay of ^{76}Ge, show $T_{1/2} > 1.8 \cdot 10^{26}\,\mathrm{yr}$ and set a limit of $m_{\beta\beta} < (79-180)\,\mathrm{meV}$ at 90% C.L. [Ago+20]. The successor to this experiment, LEGEND, is planning to feature a sensitivity of up to $10^{28}\,\mathrm{yr}$, which corresponds to an upper limit in the range of $(9-21)\,\mathrm{meV}$ [Abg+21].
Nevertheless, these results are, due to the Majorana-hypothesis and the assumption of a light-neutrino exchange, also model-dependent[1]. Therefore, a direct, model-independent measurement of the neutrino mass might be a more favorable approach.

A direct neutrino mass measurement can be realized via a precise measurement of the endpoint of a β-decay spectrum, where the kinematics and spectral model are well understood problems. From *Fermi's Golden Rule* the differential β-decay spectrum

$$\frac{\mathrm{d}\Gamma}{\mathrm{d}E} = \frac{G_F^2 \cos^2(\theta_C)}{2\pi^3} |\mathbf{M}|^2 F(Z,E)\, p\,(E+m_e) \sum_{i=1}^{3} |U_{ei}|^2 \epsilon \sqrt{\epsilon^2 - m_i^2}\, \Theta(\epsilon - m_i), \tag{2.8}$$

can be inferred. Here, the Fermi constant G_F, the Cabbibo angle θ_C, the nuclear transition matrix element $\mathbf{M}$, as well as the electron's momentum p, energy E and rest mass m_e are used. The Fermi function $F(Z,E)$ describes the Coulomb-interaction between daughter nucleus and electron. The Heaviside step function Θ ensures energy conservation and $\epsilon = E_0 - E$ denotes the difference between electron energy and the spectral endpoint E_0. The neutrino mass eigenstates enter the equation via m_i^2 so that the relevant observable is actually the incoherent sum over the neutrino mass eigenstates $m_\nu^2 = \sum_{i=1}^{3} |U_{ei}|^2 m_i^2$. From figure 2.1 it can be seen that small neutrino mass contributions not only shift the endpoint by their corresponding energy but also have a non-negligible effect on the shape of the spectrum close to the endpoint. Therefore, measuring the endpoint region of the spectrum with sufficient sensitivity could solve the neutrino mass problem.
There are several radioisotopes which can be used for such a precision measurement. Experiments using the isotopes ^{163}Ho (electron capture) and ^{187}Re (beta decay) take advantage of their low endpoint energies at around 2.5 keV. This leads to a higher probability that the decay lies in the region of interest, compared to isotopes with a larger E_0. However, the count rate is limited due to their long half-lives of around 4750 yr [Fer+15] and $4 \cdot 10^{10}\,\mathrm{yr}$ [Gal+00], which makes a high amount of material needed to gain a sufficient amount of statistics.
Experiments that utilize these isotopes include MARE [Nc+12], HOLMES [Nuc+18] and ECHo [Gas+17], all of which use the calorimetric detection principle and aim for sensitivities

[1] $\langle m_{\beta\beta} \rangle$ is also influenced by CP-violating and Majorana phases of the PMNS matrix which can lead to a cancellation of mass eigenstates and thus a reduction of $\langle m_{\beta\beta} \rangle$.

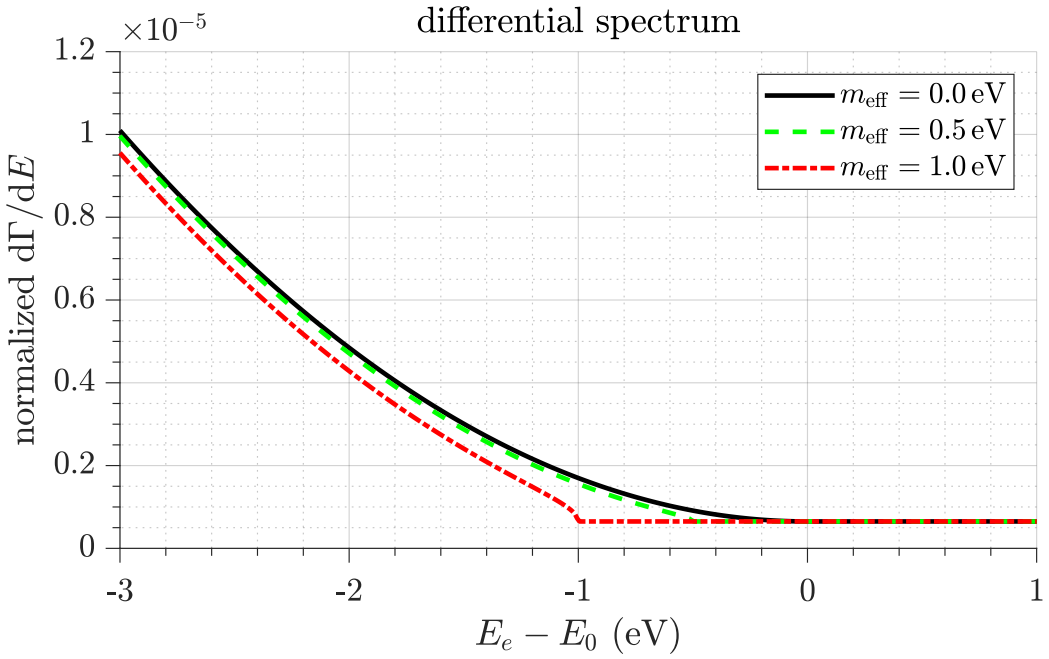

Figure 2.1: Differential tritium beta decay spectrum for three different incoherent sums of neutrino masses m_{eff} zoomed in around the endpoint E_0. Figure from [KAT].

in the sub-eV range.

The hydrogen isotope ^{3}H is another candidate for the neutrino mass search and is also the isotope used in the KATRIN (KArlsruhe TRitium Neutrino) experiment. The isotope decays via

$$^3\mathrm{H} \rightarrow {}^3\mathrm{He}^+ + e^- + \bar{\nu}_e \tag{2.9}$$

with a half-life of 12.3 yr and an endpoint energy of $E_0 = 18.57\,\mathrm{keV}$ putting it in a sweet spot concerning the count rate towards the end of the spectrum. Tritium has been successfully used in KATRIN's predecessor experiments Mainz and Troitsk, which have set upper limits of 2.3 eV [Kra+05] and 2.05 eV [Ase+11] (both 95% C.L.) using the MAC-E filter technique, which will be discussed in detail in the following chapter.

The most recent results from KATRIN yield a refined upper limit of $m_\nu < 0.8\,\mathrm{eV}$ at 90% C.L. [KAT22].

3 KATRIN experiment

The previous chapter gave a brief history on neutrino physics, discussing also the necessity for direct neutrino mass measurements. The Karlsruhe Tritium Neutrino experiment (KATRIN) currently offers the world's best upper limit on the neutrino mass from direct measurement. It aims to reach a sensitivity of 0.2 eV (90% C.L.) within the next years, reaching a total measurement time of 1000 days [Ang+05; Ake+21b]. Many challenges still need to be overcome, before this goal can be achieved. This includes a thorough understanding of the experiment's systematic uncertainties as well as its background signals.
Sections 3.1 and 3.2 provide an overview of the KATRIN experiment and the working principle of its spectrometer. The objective of this thesis is to support the development of technologies to improve the sensitivity of KATRIN with the aid of simulations. Therefore, section 3.3 describes the systematic and background component relevant to this work. As all simulations involve the usage of an angular-selective monoenergetic photoelectron source, the concept of such a device is presented in section 3.4. The chapter concludes in section 3.5 with the description of an active transverse energy filter (aTEF) which is being developed to mitigate the remaining main background source of KATRIN.

3.1 General overview of the experiment

As discussed in section 2.3 the KATRIN experiment is designed to precisely measure the endpoint region of the tritium beta decay. An overview of the experiment is shown in figure 3.1. It consists of the **Windowless Gaseous Tritium Source** (WGTS), **Transport System**, **Spectrometer System**, **Focal Plane Detector** (FPD), **Rear Section** (named Rear System in figure 3.1) and **Monitor Spectrometer** [Ake+21b].

Electrons from tritium β-decay start in the WGTS. Here, numerous control systems secure the constant circulation of high-purity gaseous molecular tritium (T_2) at precisely defined conditions [Bab+12]. Approximately 10^{11} electrons per second are generated from tritium β^--decay. These electrons are guided magnetically by various superconducting solenoids towards the spectrometer. The WGTS is also able to host gaseous Krypton (^{83m}Kr) which can

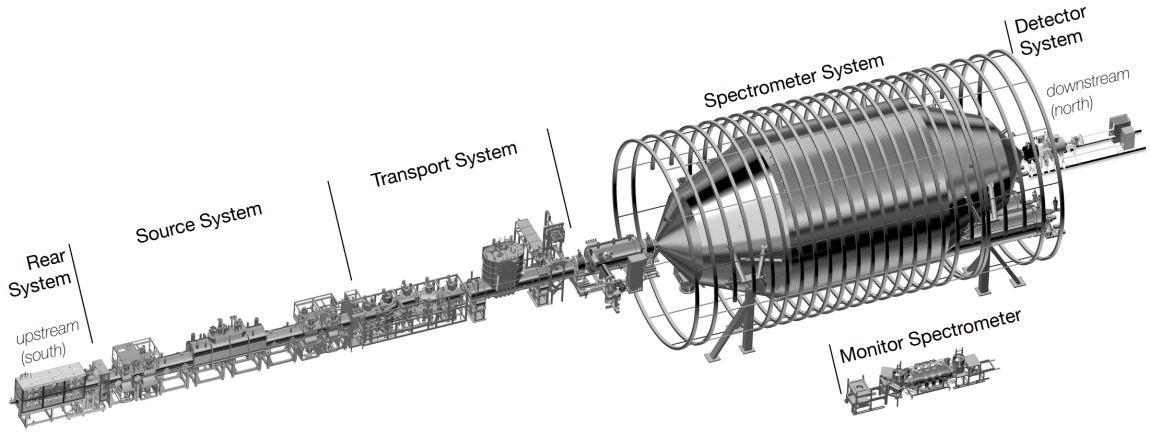

Figure 3.1: Overview of the KATRIN experiment depicting the full beamline as well as the monitor spectrometer which is separated from the main experiment and used for high-voltage calibration and other measurements. Figure from [Ake+21b].

be used for calibration measurements.

The main task of the transport system, consisting of the Differential Pumping Section (DPS) [Mar+21] and the Cryogenic Pumping Section (CPS) [Gil+09], is not only to adiabatically (see section 3.2) guide the electrons towards the spectrometer but also to reduce tritium flow by around 14 orders of magnitude. This ensures a low tritium background rate of less than $1 \cdot 10^{-3}$ cps inside the main spectrometer.

The spectrometer system is responsible for the analysis of the kinetic energy of incoming electrons. It consists of two spectrometers, a smaller pre-spectrometer and the large main spectrometer which are both of the MAC-E filter (Magnetic Adiabatic Collimation with Electrostatic filtering) type. The working principle of this technique was first shown in [HH76] and will be introduced in detail in section 3.2. In short, the MAC-E filters act as a high-pass filter with an energy resolution depending on the magnetic field setting. Thus, only electrons with a sufficient kinetic energy pass both spectrometers.

In figure 3.1 a third spectrometer can be seen. This so-called monitor spectrometer is based on the hardware from the former Mainz neutrino experiment [Kra+05]. Its main purpose is the monitoring of the high voltage stability of the main experiment [Erh+14] but it can also be used for test measurements of different components. The monitor spectrometer was used for the commissioning measurements of a new photoelectron source. The results of the corresponding simulations are presented in chapter 5.

Electrons that traverse the main spectrometer ultimately reach the focal plane detector where they are counted. This multi-pixel silicon p-i-n diode array with a total of 148 pixels is optimized for the detection of KATRIN's low energy electrons [Ams+15].

Furthermore, there is a separated rear section at the upstream side of the experiment. This section is equipped with an angular-selective photoelectron source (see section 3.4

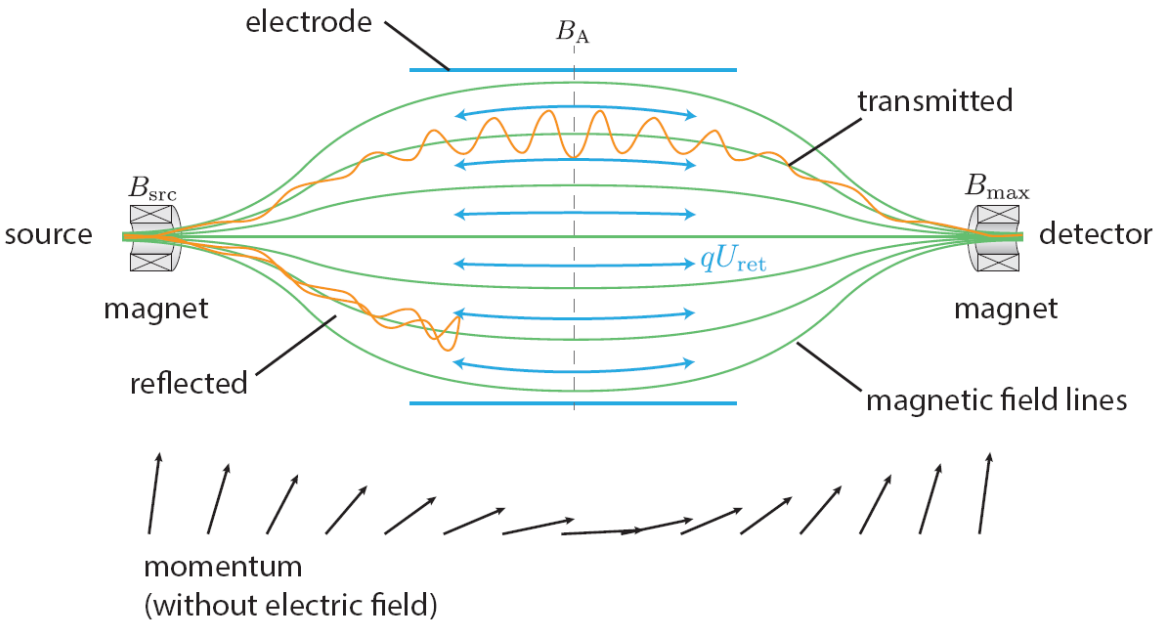

Figure 3.2: Schematic illustration of the MAC-E filter concept. Electrons enter the spectrometer from a well-defined source magnetic field (B_{src}). Propagating in a continuous cyclotron motion (orange) around the magnetic field lines (green), the slowly reducing magnetic field collimates the electron momenta so that their relative angle to the respective magnetic field line nearly vanishes. At the minimum of the magnetic field (B_A), the electrostatic potential (blue) is maximal, causing the electron to be either transmitted or reflected. Figure from [Sch21].

and [Beh+17]) which enables the possibility for various calibration and monitoring measurements.

3.2 Adiabatic collimation and transmission function

In this section, the principle of magnetic adiabatic collimation will be presented. As this concept is not only used in the main spectrometer to achieve the eV-scale energy resolution but also in the monitor spectrometer and the aTEF test setup (see chapter 6), a thorough understanding of it is important.

The working principle of a MAC-E filter can be understood with figure 3.2. Electrons are emitted in a precisely known magnetic field with strength B_{src}. Propagating in a cyclotron motion around the magnetic field lines, their absolute momenta p can be split into a component parallel as well as perpendicular to the guiding magnetic field B

$$p_{\parallel} = p \cdot \cos(\theta) \tag{3.1}$$

$$p_{\perp} = p \cdot \sin(\theta) \tag{3.2}$$

with the pitch angle

$$\theta = \theta\angle(\vec{p}, \vec{B}) = \arccos\left(\frac{\vec{p}\cdot\vec{B}}{\|\vec{p}\|\left\|\vec{B}\right\|}\right) \tag{3.3}$$

and $p^2 = p_\parallel^2 + p_\perp^2$. Hence, it follows that, although energy is not a vector quantity, one can split the total kinetic energy E of an electron into $E = E_\parallel + E_\perp$, where

$$E_\parallel = E \cdot \cos^2(\theta) \tag{3.4}$$

$$E_\perp = E \cdot \sin^2(\theta). \tag{3.5}$$

As the electron performs a gyrating motion, it is also useful to calculate the cyclotron radius r_c as well as the cyclotron frequency ω_c. With the Lorentz force $F_L = eB \cdot v_\perp$ it follows that

$$r_c = \frac{\sqrt{2m_e E_\perp}}{eB} \tag{3.6}$$

and

$$\omega_c = \frac{eB}{m_e}, \tag{3.7}$$

with e being the charge of an electron, and m_e being the electron mass. It has been shown in the case of static magnetic fields and vanishing electric fields that, if the change of the magnetic field during one cyclotron motion is small

$$\left|\frac{1}{B}\frac{\mathrm{d}B}{\mathrm{d}t}\right| \ll \frac{\omega_c}{2\pi} \tag{3.8}$$

there are three conserved quantities of the electron motion [Jac99]

$$\left.\begin{array}{c} Br_c^2 \\ p_\perp^2/B \\ \gamma\mu \end{array}\right\} = \text{adiabatic invariants.} \tag{3.9}$$

The relevant expression for the following calculations is $\gamma\mu$, where μ is the magnetic moment of the particle and $\gamma = 1/\sqrt{1-(v/c)^2}$ is the relativistic Lorentz factor. As the kinetic energy of electrons at the endpoint of the tritium beta-decay at 18.6 keV corresponds to $\gamma = 1.04 \approx 1$, the calculations in this section are treated non-relativistically. In the context of KATRIN, μ is mostly defined via the transverse energy component $E_\perp$

$$\mu = \frac{E_\perp}{B} = \frac{m_e v_\perp^2}{2B} = \text{const.} \tag{3.10}$$

which is convenient, as the transverse energy component is directly connected to the pitch angle. This enables precise predictions for θ. It has to be noted though, that a thorough calculation reveals that the adiabatic invariant is actually an asymptotic series

$$\mu = \mu_0 + \epsilon\mu_1 + \epsilon^2\mu_2 + \mathcal{O}(\epsilon^3) \tag{3.11}$$

with the smallness parameter $\epsilon = m_e/q$. Only in the non-relativistic case with constant magnetic fields and small electric fields is the magnetic moment defined in equation (3.10) equal to μ_0 [NT60; Nor63].
With equation (3.10) it becomes apparent that the pitch angle of electrons changes depending on the magnetic field strength. It directly follows that

$$\frac{E_\perp}{B} = \frac{E'_\perp}{B'} \tag{3.12}$$

which can be transformed to

$$\sin^2\theta' = \sin^2\theta \cdot \frac{B'}{B} \tag{3.13}$$

using equation (3.5). In a MAC-E filter the electrostatic retarding potential qU creates a repelling force so that only electrons (with charge $q = -e$) that satisfy

$$E_\parallel(z) - qU(z) > 0 \tag{3.14}$$

at any position z are transmitted. Therefore, to achieve the eV-scale energy resolution, the electron momenta need to be collimated before they are analyzed by the retarding potential. Using equation (3.12), it is possible to calculate the maximum remaining transverse energy in the analyzing plane $E_{\perp,\max}$, which is the energy resolution ΔE of the spectrometer:

$$\Delta E = E_{\perp,\max} = E_{\max} \cdot \frac{B_A}{B_{\max}}. \tag{3.15}$$

Here, $E_{\max}$ is the maximum kinetic energy, B_A the magnetic field in the analyzing plane and $B_{\max}$ the maximum magnetic field. Rewriting the original transmission condition from equation (3.14) using equations (3.12) and (3.13), it follows that[1]

$$E - E \cdot \sin^2\theta \, \frac{B(z)}{B_{\text{src}}} - qU(z) > 0 \tag{3.16}$$

[1] Source potential variations are neglected here.

where B_{src} corresponds to the magnetic field in the source. As in the current setup $B_{\mathrm{max}} > B_{\mathrm{src}}$, this equation also shows that electrons emitted with large pitch angles are reflected magnetically before reaching the detector. The maximum pitch angle is given by

$$\theta_{\mathrm{max}} = \arcsin\left(\sqrt{\frac{B_{\mathrm{src}}}{B_{\mathrm{max}}}}\right). \tag{3.17}$$

For an isotropically emitting source the transmission function can then be calculated to [Kle+19]

$$T(E, qU) = \begin{cases} 0, & \text{for } E < qU \\ 1 - \sqrt{1 - \frac{E-qU}{E}\frac{B_{\mathrm{src}}}{B_{\mathrm{ana}}}}, & \text{for } qU \leq E \leq qU + \Delta E \\ 1 - \sqrt{1 - \frac{B_{\mathrm{src}}}{B_{\mathrm{max}}}}, & \text{for } qU + \Delta E < E \end{cases}. \tag{3.18}$$

The magnetic field configuration used in the second measurement campaign ($B_A = 6.3{\cdot}10^{-4}\,\mathrm{T}$, $B_{\mathrm{src}} = 2.5\,\mathrm{T}$ and $B_{\mathrm{max}} = 4.2\,\mathrm{T}$ with $E_{\mathrm{max}} = 18.6\,\mathrm{keV}$) results in an energy resolution of $\Delta E = 2.8\,\mathrm{eV}$ and a maximum pitch angle of $\theta_{\mathrm{max}} = 50.4°$ [KAT22]. The corresponding transmission function is depicted in figure 3.3.

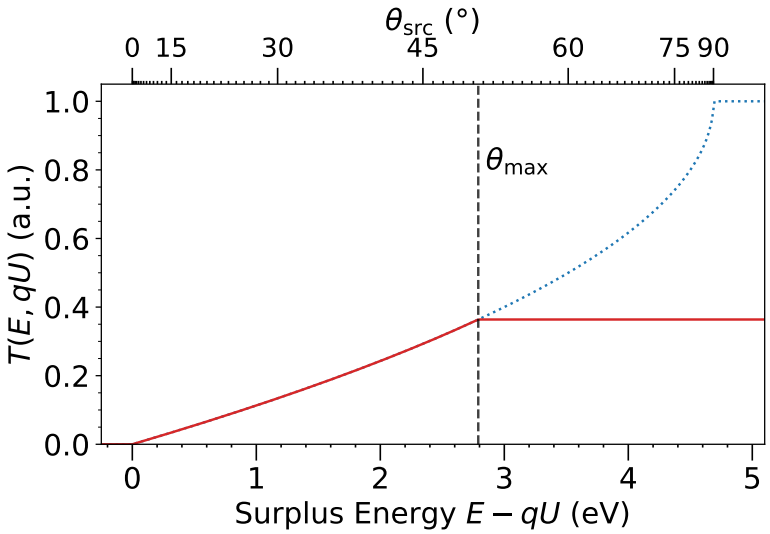

Figure 3.3: Transmission function $T(E, qU)$ of the main spectrometer using the configuration of the second neutrino mass measurement campaign [KAT22] for electrons near the tritium endpoint energy emitted from an isotropic source (red). The secondary x-axis on top indicates the maximum pitch angle θ_{src} inside the WGTS for which these electrons are transmitted. Magnetic reflection occurs at $\theta_{\mathrm{max}} = 50.4°$ (see equation (3.17)). If the magnetic field configuration was altered, so that electrons started already in the maximum magnetic field ($B_{\mathrm{src}} = B_{\mathrm{max}} = 2.5\,\mathrm{T}$), the magnetic mirror effect would not occur (blue, dotted). Although this would benefit the angular acceptance of the spectrometer, it would also increase the energy resolution to $\Delta E = 4.69\,\mathrm{eV}$ (see equation (3.15)).

While the characteristics of the spectrometer are of great importance for KATRIN's neutrino mass sensitivity, many other experimental details need to be considered. Therefore, the following section introduces important characteristics relevant to this work that affect the neutrino mass sensitivity.

3.3 Sensitivity limiting effects at KATRIN

To achieve its design sensitivity of $0.2\,\mathrm{eV/c^2}$, several steps need to be taken to characterize and reduce the neutrino mass uncertainty. While a lot of work has been dedicated to the understanding and reduction of background and systematic uncertainties [Frä+17; Lok+22; Rod+22; Ake+21a], some aspects still remain. The largest contributions originate from the plasma uncertainty as well as a specific background component limiting the statistical uncertainty. Since the goal of this work is to support the development of technologies designed to reduce both of these sensitivity limitations, the following section will provide information on the origin of these.

3.3.1 Plasma uncertainty

At KATRIN, the measured integral spectrum is a convolution of the theoretical differential β-decay spectrum $\frac{\mathrm{d}\dot{N}}{\mathrm{d}E}$ with the response function $R(E,\, qU,\, r)$ of the experiment [KAT22]

$$\dot{N}(qU) \propto \int_{-\infty}^{\infty} \frac{\mathrm{d}\dot{N}}{\mathrm{d}E}(E) \cdot R(E,\, qU,\, r)\,\mathrm{d}E. \tag{3.19}$$

As the system response combines all relevant systematic effects, knowledge of this function is of extreme importance for achieving KATRIN's design sensitivity.
A large contributing factor is connected to the source plasma. Although absolute and radial potential variations inside the source are effectively absorbed by the spectral endpoint being a free fit parameter and the ringwise spectrum calculation, other influences of the source potential need to be treated more carefully. To investigate the plasma characteristics, $^{83\mathrm{m}}$Kr gas is used, which can be added to the tritium gas circulation of the WGTS. The mono-energetic conversion lines between 7 keV and 32 keV allow to assess different plasma characteristics such as possible inhomogeneities or instabilities, which lead to a broadening σ of the natural line width and, thus, to a neutrino mass shift.
In addition, electrons are subject to elastic and, more importantly for neutrino mass analysis, inelastic scattering with gas atoms as they travel through the source. Thereby, the scattering probability is dependent on the starting position of the respective electron. Electrons starting at the beginning of the source have a higher scattering probability than electrons

emitted further downstream. As the starting potential of the electrons can vary along the beam line, one can define the mean starting potential $\langle V \rangle_i$ of electrons with different scattering multiplicities i. The difference of the mean starting potentials of one-time scattered and unscattered electrons is defined as $\Delta_{10} = \langle V \rangle_1 - \langle V \rangle_0$ and can also be interpreted as the change of the position of the first scattering peak to its expectation value of approximately 13 eV. It contributes to the neutrino mass shift via

$$\Delta m_\nu^2 = -\epsilon_1 \Delta_{10} - 2\sigma^2, \tag{3.20}$$

with ϵ_1 being a proportionality factor [Mac20]. Determining Δ_{10} is highly dependent on the underlying energy loss model. Krypton measurements are only able to provide an upper limit on Δ_{10}. The energy loss function at 18.6 keV has already been measured using a monoenergetic photoelectron source [Ake+21a]. However, extrapolation to the higher energetic Krypton line positions at up to 32 keV is not trivially possible. A measurement of the energy loss function at this energy range is needed and could provide a significant improvement to the total plasma uncertainty. For this, the current electron source needs to be exchanged by a new one, which is able to provide the needed electron energy. The general concept of the photoelectron source is presented in section 3.4.

3.3.2 Rydberg background

One of the dominant backgrounds identified is the ionization of highly-excited (Rydberg) atoms inside the main spectrometer [Frä+22]. During the commissioning phase of the main spectrometer, it has been exposed to ^{222}Rn, which decays in multiple steps into the long-lived radionuclide ^{210}Pb ($T_{1/2} = 22.2$ yr [Bas14]). One of its progenies is the α-emitting ^{210}Po. Implanted by earlier α-decay into the spectrometer wall, atoms can be sputtered off due to the high nuclear recoil of its daughter nucleus ^{206}Pb. While ionized atoms cannot overcome the inner electrode system, which is set to a more negative voltage than the spectrometer vessel, neutral atoms can propagate into the main spectrometer volume. If these atoms reach the spectrometer wall on the other side, more particles can be sputtered off. The sputtering process is able to leave them in a highly excited state, which makes ionization, for example, by black body radiation possible. If ionization takes place inside the magnetic flux tube as well as behind the analyzing plane, the generated electrons are accelerated towards the detector. Since the electrons from Rydberg atoms carry very small initial kinetic energies after ionization, the following acceleration by the retarding potential leaves them energetically indistinguishable form signal electrons at the detector [Tro18]. Moreover, due to the electromagnetic conditions inside the main spectrometer, their maximum transverse energy

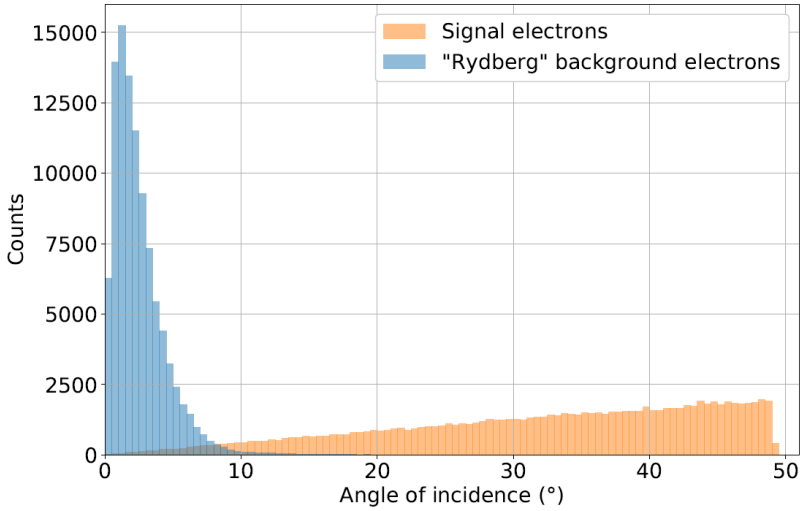

Figure 3.4: Simulated angular distributions of signal electrons (orange) and background electrons originating from the ionization of highly excited Rydberg atoms (blue). Image from [Gau+22]

is limited. It is currently suggested that the angular distribution of electrons originating from the ionization of Rydberg atoms differs significantly from the angular distribution of signal electrons. This is indicated by figure 3.4, which shows a simulated angular distribution of Rydberg electrons at the FPD.

As the Rydberg background is directly connected to the flux tube volume behind the analyzing plane, measures have already been taken to shift the analyzing plane further towards the detector. Although this also harms the energy resolution of the spectrometer, the shifted analyzing plane (SAP) mode [Lok+22] reduces background by a factor two and has taken over as the main setting during neutrino mass measurements.

A further idea, which aims to exploit the angular distribution of background electrons originating from Rydberg atoms, utilizes their small cyclotron radii. This so-called aTEF detection principle is presented in section 3.5.

3.4 Angular-selective photoelectron source

As stated in section 3.3, knowledge of the energy loss function for kinetic energies at around 30 keV is necessary to reduce the uncertainty related to the plasma inside the WGTS. For this measurement, a monoenergetic and angular-selective photoelectron source, which is able to create electrons in the desired energetic range in a stable manner is required. The currently utilized electron source is only able to achieve energies up to 21 keV [Sac20] which disqualifies it for this task. Hence, an upgraded version of this photoelectron source was developed in Münster.

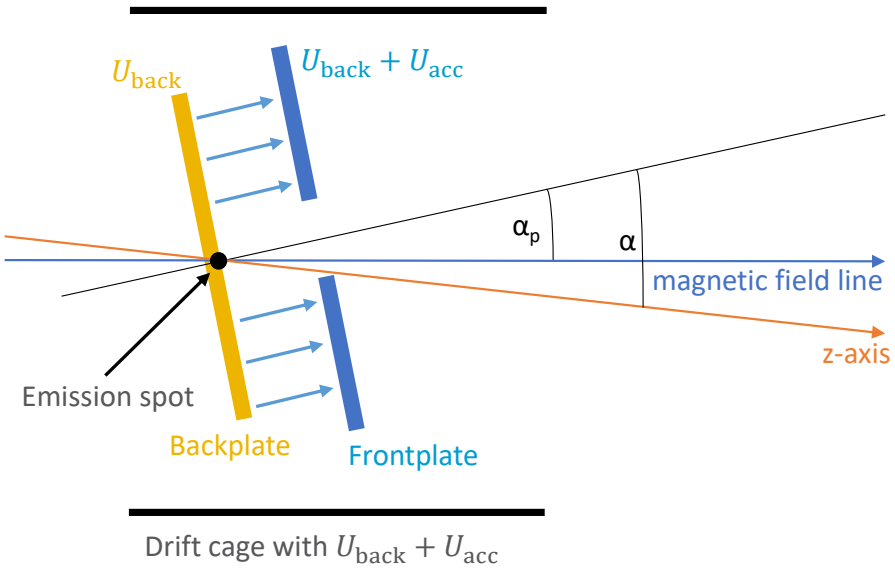

Figure 3.5: Schematic illustration of the geometry an angular selective photoelectron source. Emitted via photoeffect from a photocathode on the backplate, electrons are accelerated non-adiabatically by a strong electric field between the backplate (with voltage U_{back}) and the frontplate (with voltage $U_{\text{back}} + U_{\text{acc}}$). The plates can be tilted mechanically to achieve an angle α_p relative to the guiding magnetic field and α relative to the z-axis. For the upgraded electron source, a drift cage, which cannot be tilted, is set to the frontplate potential to provide a more homogeneous electric field. In the rear section the drift cage is omitted due to dedicated post-acceleration electrodes providing a homogeneous electric field.

This kind of electron source is, however, not only relevant for the task described above, but it also finds application in the test setup used for the development of the aTEF. In this thesis, both the upgraded and the electron source from [Beh+17] are used in this setup. Therefore, this section provides a brief general overview of the working principle of these angular-selective monoenergetic photoelectron sources.

A schematic overview of the working principle of a photoelectron source is shown in figure 3.5. Electrons are emitted via the photoelectric effect at the center of the backplate. For this, photons from a UV light source with energy E_γ are guided through an optical fiber towards the backside of a several nanometer thin photocathode usually made of gold. The kinetic energy of an emitted electron can be calculated in a simplified model using the work function of the photocathode material Φ via

$$E_{\text{kin}}(e^-) = E_\gamma - \Phi = \frac{hc}{\lambda} - \Phi \tag{3.21}$$

where h is the Planck constant, c is the speed of light in vacuum and λ is the wavelength of the photon. A photon source that matches the energy of the work function is desired for a

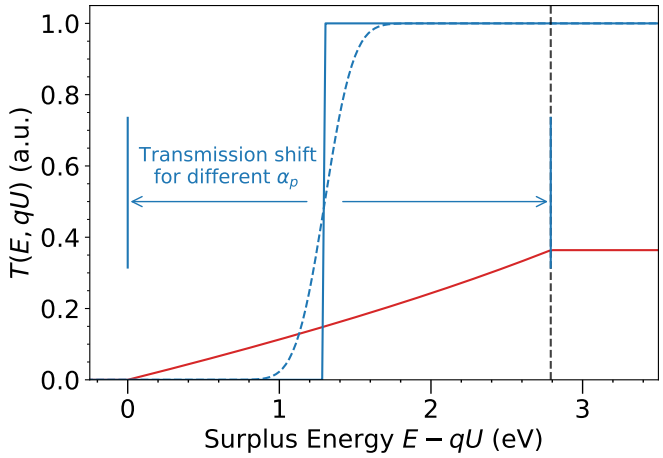

Figure 3.6: Transmission functions of the main spectrometer for different sources. The transmission function of a monoenergetic isotropic source (red) is equal to the one depicted in figure 3.3. The transmission function of an angular-selective monoenergetic electron source with no angular or energy spread reduces to a step function (blue, solid). Due to the small but non-zero kinetic energy of electrons emitted via photoeffect, the step function is broadened and can be approximated by an error function (blue, dashed). However, it has to be noted that this is a simplified model, which does not take all effects into account. Different plate angles α_p relative to the magnetic field allow to shift the transmission function within the energy resolution of the spectrometer (here: $\Delta E = 2.8\,\mathrm{eV}$).

narrow kinetic energy distribution.

After emission, the electrons are accelerated by a strong homogeneous electric field, which is created by the voltage difference $U_{\mathrm{acc}} = U_{\mathrm{front}} - U_{\mathrm{back}}$ between two electrodes. Electron propagation in an electromagnetic field is described by the Lorentz force

$$F_L = q\left(\vec{E} + \vec{v} \times \vec{B}\right). \tag{3.22}$$

The early acceleration phase is therefore dominated by the strong electric field where the electron gains a large amount of kinetic energy. Hence, the acceleration is strongly non-adiabatic. In combination with a plate angle $\alpha_p > 0$ with respect to the guiding magnetic field, this allows the electron to build up a transverse momentum component relative to the magnetic field and, thus, a pitch angle θ. Since the magnetic field is not necessarily aligned with the symmetry axis of the setup, the plate angle can also be given relative to the z-axis. Then the plate angle is referred to as α. After the initial acceleration phase, electrons are able to pass the frontplate through a narrow slit (or hole). With increasing velocity and decreasing electric field the motion is now dominated by the magnetic field and the electron starts to propagate in an adiabatic cyclotron motion.

The properties of this type of electron source have a strong influence on the transmission

function of the MAC-E filter. For an ideal mono-energetic electron source with no angular spread, the transmission function would effectively reduce to a step function as depicted in figure 3.6. In reality, however, a finite energy and angular spread needs to be taken into account. The transmission function $T(E)$ is calculated via the integral of the underlying distribution $T'(E)$

$$T(E) = \int_E^\infty T'(\epsilon)\,\mathrm{d}\epsilon. \tag{3.23}$$

In a simple purely mathematical approximation, where both the angular distribution as well as the energy spread are following a Gaussian distribution, the transmission function smears out to an error-function. The broadening is then given by the widths of the underlying distributions. In a more refined model, it was shown that the energy distribution can be modeled via a generalized Gaussian distribution while the angular distribution can be modeled by the sum of two Gaussians [Beh+17].

3.5 Active transverse energy filter concept

In the previous chapter, the impact of ionizing Rydberg atoms was discussed. Since the kinetic energy at the detector of the emitted electrons is of the same order as that of the signal electrons, they can hardly be distinguished. However, comparison of measurement data with simulations shows a significant difference of the underlying angular distribution [Tro18]. Therefore, the concept of a transverse energy filter is proposed [Gau+22].
In section 3.2 adiabatic collimation was introduced. One key element in this concept is that the state of the electronic cyclotron motion in a well-known magnetic field can be defined via the total kinetic energy and the pitch angle relative to the guiding magnetic field line. Larger pitch angles therefore automatically lead to larger cyclotron radii compared to smaller pitch angles (compare equation (3.6)). This enables the possibility to geometrically distinguish the pitch angle of incoming electrons based on their cyclotron radius. Two general strategies have been tested for the application of this concept, *active* and *passive* filtering.
A passive filter can be exemplarily realized by a sequence of two (or possibly more) slit arrays which feature a well-defined slit width and spacing. Proper alignment of these slits would result in absorption of (background) electrons with small cyclotron radii while (signal) electrons with large radii would bypass the slits and thus be transmitted. Simulations have shown that such a configuration could indeed lead to a significant reduction of Rydberg background by about 95%. However, this is also coupled with a reduction of signal electron rate by about 75% [Rob19]. As the loss of sensitivity due to the reduced statistics would outweigh the gain from the improved background, a passive transverse energy filter is not suited for background

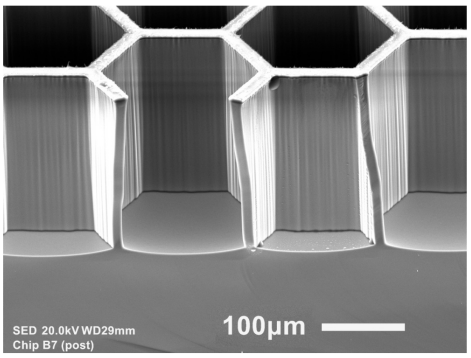

Figure 3.7: Picture of an exemplary hexagonal silicon structure captured by a JEOL11 JSM-IT100 scanning electron microscope. The channels are designed with a side length of 100 µm, wall thickness of 10 µm and etched depth of 225 µm. Image taken from [Gau+22]

reduction at KATRIN.

Building upon initial ideas on transverse energy filters from R.G.H. Robertson, the concept of an active filter was put forward by C. Weinheimer. The key point is the direct signal creation or amplification of electrons depending on their pitch angle. Specifically, this means that a filter consisting of an array of channels absorbs electrons with large pitch angles, creating, for example, an avalanche of secondary electrons, while electrons with small angles are transmitted without interaction. This corresponds to the operating principle of a microchannel plate detector (MCP) if the bias angle of commercially available MCPs is neglected. Measurements using such a device have already demonstrated the functionality of angular-selective electron detection using MCP-aTEFs [Gau+22; Oel21; Kön21]. However, commercial MCPs have several drawbacks which disfavor them as an aTEF in the measurement environment of KATRIN. Several parameters, such as the open area ratio, channel radius and depth, as well as dark count rate need to be optimized.

For this reason, there are efforts to self-manufacture a detector featuring active transverse energy filtering. One of these efforts is based on silicon (Si) p-i-n diodes which can be microstructured with hexagonal channels to enable transverse energy filtering. The choice of material is advantageous due to the radiochemical purity and, thus, low intrinsic background rate of Si. The structure of the material can be modified via cryo-etching procedures such as inductively coupled plasma reactive-ion etching (ICP-RIE) [HWS09; De +02; Jan+09] to create channels with well-defined parameters. To increase the open area ratio compared to round channels, a honeycomb-like hexagonal structure is deemed to be optimal. Figure 3.7 shows an exemplary etched honeycomb-like silicon structure. The detection principle can be understood with figure 3.8 which shows a Monte-Carlo simulation of signal and background electron tracks. As in the case of an MCP-based aTEF, electrons with large pitch angles hit

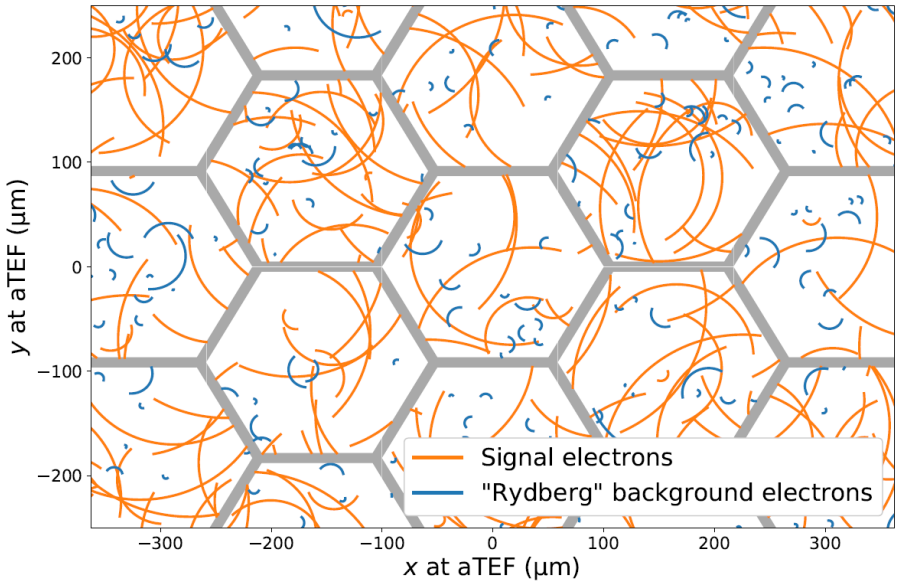

Figure 3.8: Top view of an aTEF with hexagonal structure with simulated cyclotron tracks of signal (orange) electrons with large pitch angles and Rydberg background electrons with small pitch angles (blue). Simulation starts at the entrance of the structure in an underlying magnetic field of 2.4 T which corresponds to the magnetic field at the FPD at KATRIN. Electrons propagate in viewing direction while the magnetic field vector points in opposite direction. The angular distribution is based on figure 3.4. The channels have a side length of 100 µm, wall thickness of 10 µm and a depth of 400 µm. Image from [Gau+22]

the channel walls and trigger a detectable signal (in this case via the creation of electron-hole pairs), while electrons with small pitch angles hit the passive channel bottom with no detectable response.

According to the current Rydberg background model [Tro18] it is estimated that a functioning aTEF device can significantly reduce the rate from Rydberg background electrons. As the statistical uncertainty of Δm_ν^2 is proportional to $b^{1/6}$ [OW08], where b is the background rate, an estimated reduction by a factor 10 in background rate due to the aTEF yields an improvement of a factor 1.5 for Δm_ν^2. Therefore, the successful development of an active transverse energy filter could provide an important step towards achieving the sensitivity goal of KATRIN.

4 Precise electron tracking with Kassiopeia

The simulations presented in this thesis were all computed using the simulation software Kassiopeia [Fur+17]. This framework, written in C++, was created by the KATRIN collaboration and offers many key features needed for precise particle tracking in complex electromagnetic environments.
In the following chapter a brief overview over the most important features of Kassiopeia is given, before the configuration of the most important simulation parameters and geometries used for this work is presented. The results of the simulations will be presented and discussed in chapters 5 and 6.

4.1 Feature overview

The simulation process within Kassiopeia can be split up into three central parts: Implementation of the relevant geometry, calculation of the electromagnetic field and particle tracking from start to finish.
Kassiopeia allows to implement geometries of arbitrary complexity. For this, it not only provides several pre-defined elements which cover the most important geometric structures (such as tubes, cylinders, etc.) but it also allows to build more complex elements by defining a set of points which are then connected via lines or arcs. Each geometry element that is included in the simulation is stored inside a tree-like data structure. This makes it possible to displace or rotate different shapes or geometric groups relative to the particular parent space.
Calculation of the static electric field is done via the boundary element method (BEM) [Cor14]. For this, each geometry element that is included in the field computation is required to have a mesh extension, specifying the amount of mesh elements and their density distribution. These mesh elements represent discretized boundary elements to calculate the charge density function of the whole surface which is then used to calculate the electric potential and field at any given point of the system. Choosing the right discretization level is very important, as more boundary elements usually lead to more accurate calculations but also require more computing power. Usage of axial symmetry can speed up the calculation of

both, the charge density as well as the electrostatic field. Furthermore, it has to be noted that the actual computation of the electric field is only performed during particle tracking. The magnetic field calculation is substantially faster, as there are no charge densities that need to be calculated beforehand. Furthermore, most magnetic fields mostly consist of axisymmetric coils where the zonal harmonic expansion method can be applied. Otherwise the Biot-Savart formula can be integrated directly.
The simulation itself can be categorized into four different levels: **run**, **event**, **track** and **step**. Every simulation for a fixed configuration contains exactly one **run** which is able to contain multiple events. Each **event** then contains a primary particle which, if interactions are activated in the configuration, can also create secondary particles that can also produce more secondary particles. All of these related particles are grouped in one **event**[1]. Each particle is, from its generation until its termination, associated with a **track** that can be split into steps. **Steps**, therefore, form the lowest level of particle tracking. The equations of motion are solved for each step individually. The step length can be controlled, using e.g. a fixed value or using a dynamic evaluation where the length is adjusted to limit numerical errors. Different control methods can also be combined.
All primary particles must be produced by a pre-configured generator which defines the starting parameters. These parameters include time, position, energy and direction. The corresponding values can be drawn from a user-defined distribution.
In Kassiopeia, particle trajectories can be calculated using different levels of approximation, ranging from a pseudo-particle following a magnetic fieldline (magnetic trajectory) over an adiabatic trajectory calculating just the guiding center motion to an exact calculation solving the full equation of motion (exact trajectory). The latter is most relevant for this thesis as adiabaticity cannot be generally assumed in these cases. A motivation, why a certain trajectory type is used in the simulation will be given in the respective sections 4.2.2 and 4.2.3.
For an in-depth description of all relevant Kassiopeia features, the reader is referred to [Fur+17] and [Beh17].

4.2 Implementation of relevant geometries and simulation parameters

This section is going to provide the most important simulation parameters used for the results presented in chapters 5 and 6.

[1] As interactions are not considered in this thesis, each event is going to contain only one particle.

4.2.1 Electron source geometries and parameters

In the scope of this thesis, two different angular-selective monoenergetic photoelectron sources were used. This includes the source from [Beh+17; Beh17], which will be referred to as 18 keV source, as well as the upgraded photoelectron source, which will be referred to as 32 keV source as it is capable of producing electrons up to a kinetic energy of 32 keV. The former is exclusively implemented in the simulation of the aTEF test setup, while for the latter commissioning measurements were done at the monitor spectrometer and it was applied to the aTEF test setup. Hence, it is used in both environments.

18 keV source properties

The simulation geometry files of the 18 keV source were created by J. Behrens and have already been used in an earlier work [Sal19]. A picture of the source can be found in figure 4.1. This electron source features two circular electrodes with the same radius of 3 cm placed in a distance of 1 cm from each other. Electrons are able to pass the frontplate through a circular hole with radius 3 mm. The plates can be tilted around the emission spot in the middle of the backplate to achieve angular selectivity. A grounded source cage encloses both plates. As it follows the plate rotation, it ensures equal electrostatic acceleration conditions for any tilt angle.

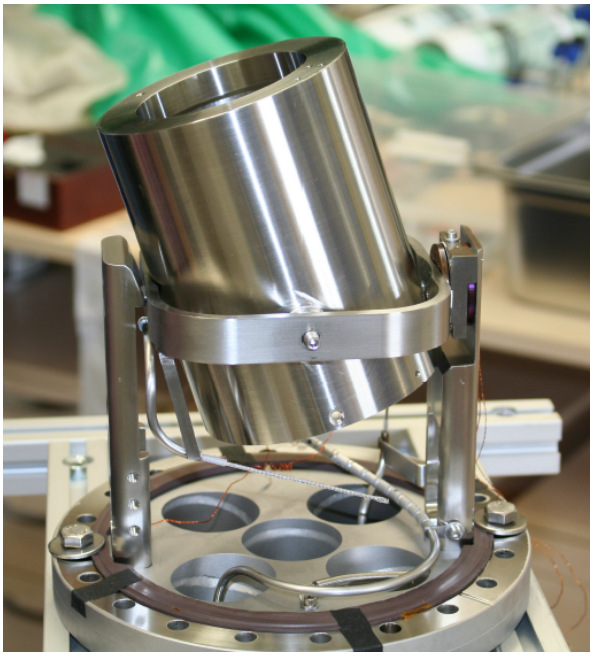

Figure 4.1: Picture of the 18 keV angular-selective monoenergetic electron source. Image taken from [Beh17].

32 keV source properties

A CAD drawing of the geometry of the upgraded photoelectron source is depicted in figure 4.2. To be able to sustain the high voltages up to −32 kV, the source geometry was revised compared to the previously installed photoelectron source in the rear section [Sac20]. This includes, for example, the backplate that was reduced in size (from 5 cm to 3 cm radius). This made it necessary to equip it with a bead to increase the homogeneity of the electric field. Furthermore, the distance between front- and backplate has been increased to 2 cm to allow higher acceleration voltages and thereby reduce the absolute voltage on the frontplate. To still allow electrons to pass through the frontplate, the size and shape of the opening needed to be modified. Instead of a circular hole, the width has been increased so that it now resembles a slit with round edges (see figure 4.2(b)). A driftcage can be installed enclosing the plates. However, it cannot be tilted.
These modifications as a whole significantly change the electrostatic conditions during the acceleration process and, thus, affect important characteristics of the electron source such as the energy or angular distribution. Therefore, in the scope of this thesis a precise representation of the geometry was created and mesh optimizations for the computation of the electrostatic field were performed.

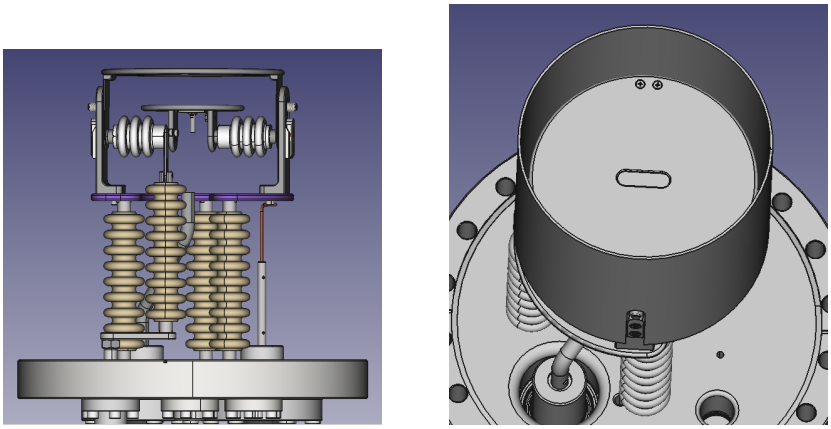

(a) Side view without driftcage

(b) Frontplate slit geometry including driftcage

Figure 4.2: CAD drawing of the upgraded angular-selective photoelectron source, provided by H.W. Ortjohann.

The full XML configuration of the 32 keV source can be found in appendix A.1. As the changes concerning the backplate were only minor, the focus has been on the design and optimization of the frontplate. Based on the CAD drawings, the simulation geometry consists of a base structure onto which finer structures such as the roundings of the slit are modeled. The frontplate mesh has been optimized for fast computation whilst retaining precise

electrostatic field calculation. To test the mesh, a map of the calculated potential on the surface of the far side of the frontplate (facing away from the backplate) was calculated and is displayed in figure 4.3. The outline of the frontplate with potential $U_{\text{front}} = -18\,240\,\text{V}$ and radius 5 cm is clearly visible. As the colorbar is symmetric around U_{front}, potential variations can be spotted easily. In this case, variations are generally below 0.25 V. Furthermore, the largest variations are located towards the outer areas of the plate. The slit geometry can also be spotted in the middle of the plate where an area with lower potential is encompassed by a slim area with larger potential. The former is dominated by the influence of the backplate which is set to $U_{\text{back}} = -32\,\text{kV}$. Due to the complex slit geometry, which has a larger radius towards the side facing the backplate than towards the side facing away from the backplate, the field from the backplate is shielded so that the potential in this small area is larger than the general frontplate potential.

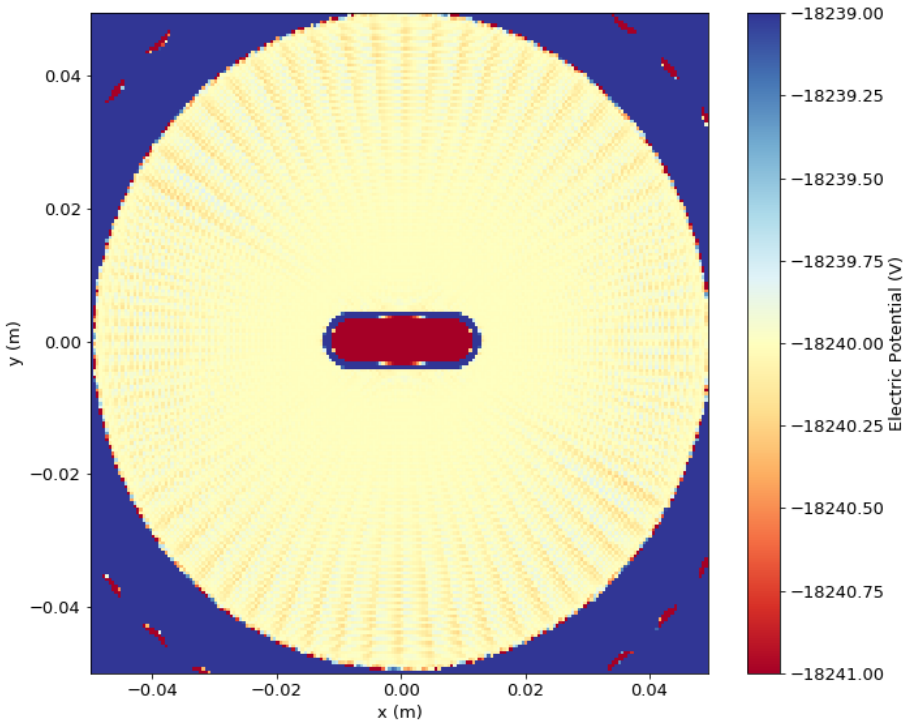

Figure 4.3: Electric potential on the surface of the frontplate of the 32 keV electron source with optimized boundary element mesh. With the backplate voltage $U_{\text{back}} = -32\,\text{kV}$ a frontplate voltage of $U_{\text{front}} = 0.57 \cdot U_{\text{back}} = 0.57 \cdot -32\,\text{kV} = -18\,240\,\text{V}$ was applied. The resolution of this potential map is 0.5 mm.

Electron generation for both sources

Another important aspect of the source configuration comprises the starting parameters such as the electron's initial position, momentum vector or energy as these can significantly alter the simulation outcome. All simulations containing either the 18 keV source or the 32 keV source follow a Monte-Carlo approach, where a random value for each component is drawn from a particular distribution. The corresponding parameters were largely taken over from J. Behrens [Beh17] who did a lot of fundamental work to determine these properties and to represent them in the simulation. Table 4.1 shows the used configuration for the generation of electrons at the backplate.

Table 4.1: Monte-Carlo generator settings used for the creation of electrons on the backplate of the used electron sources.

Parameter	Distribution	Values
Position (cylindrical coordinates)	r: uniform	min: 0 m, max: 100e-6 m
	ϕ: uniform	min: 0°, max: 360°
	z: gauss	min: 1e-9 m, max: 1e-7 m, mean: 1e-8 m, σ: 2e-8 m
Direction (spherical coordinates)	θ: cosine	min: 0°, max: 90°
	ϕ: uniform	min: 0°, max: 360°
Energy	gauss	min: 0 eV, max: 0.4 eV, mean: 0.15 eV, σ: 0.075 eV

4.2.2 Configuration of the monitor spectrometer simulation

The geometry of the monitor spectrometer (MoS) was already mostly implemented in Kassiopeia as a part of the KASPER framework, which is the main development framework of the KATRIN experiment. For its commissioning measurements the 32 keV electron source was attached to the MoS beamtube at the upstream side of the spectrometer. Hence, it was necessary to modify this part of the simulation geometry. A cross-section along the y-z plane of the geometry can be found in figure 4.4. This graphic specifically shows the source section of the MoS. All elements before $z = -2.395$ m, which marks the beginning of the axially symmetric geometry of the spectrometer itself, were added in the scope of this thesis. The MAC-E filter geometry as well as the solenoids at the entrance and the exit of the spectrometer have been available from KASPER.

The 32 keV electron source was placed inside a CF160 tube at the beginning of the beamline. A half pipe with outer radius 80 mm, a thickness of 1 mm and a length of 120 mm was placed as a dipole electrode at a distance of 8.5 cm from the frontplate to remove stored electrons. The dipole electrode was installed at the edge towards a larger vacuum chamber ("Elipot") which holds several additional ports used for e.g. pressure measurement. As this chamber is

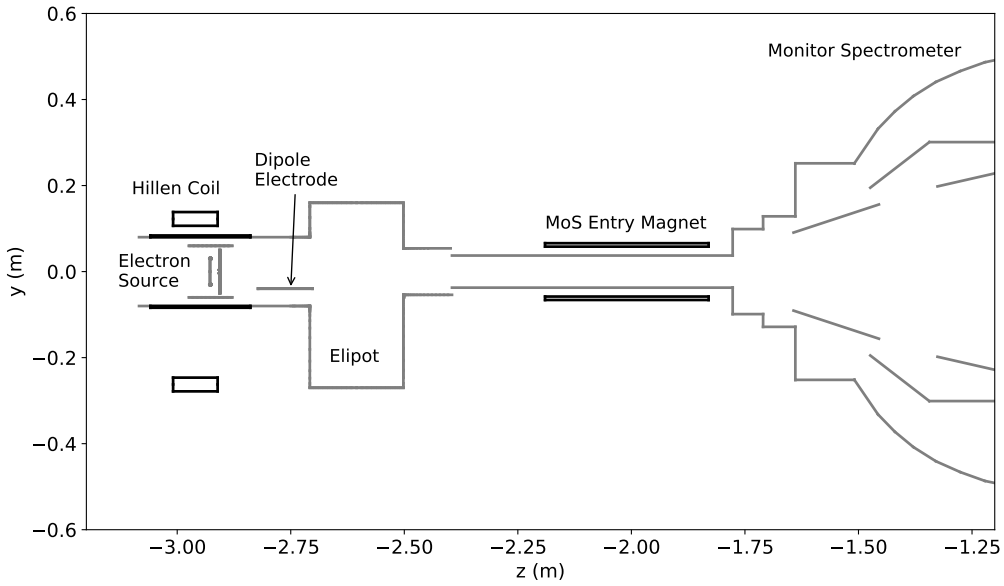

Figure 4.4: Cross-section of the MoS source section geometry along the y-z plane. Displayed are all relevant electrodes (gray) and magnets (black) used for the calculation of the electrostatic and magnetic field.

expected to have a significant effect on the shape of the electric field, the elipot was implemented as well.

The added geometries overall break the axial symmetry of the rest of the spectrometer. Therefore, to speed up the computation, the calculation of charge densities was split up into two sections which can be inferred from figure 4.5: The source section with all the added geometric elements and the MAC-E filter section using the KASPER elements. Splitting the computation of charge densities is usually not the preferred method, as the charge density distribution of one electrode has an influence on all other electrodes. However, this influence decreases with increased distance. Between the source section and the MAC-E filter, there is a region, where the electric potential is roughly constant with $U \approx 0\,\mathrm{V}$. A change between the two computation methods in this region is therefore only going to have a minor effect. A small overlap of geometries used for the electrostatic field computation between both regions further ensures smaller numerical errors at the break point at $z = -2.3\,\mathrm{m}$ where the field calculation methods are swapped. As the electric potential changes abruptly from one step to another, a discrete step of the potential is visible. This numerical error can be investigated with the following method.

During particle tracking the total kinetic energy can be expressed via

$$E_{\mathrm{tot}} = E_{\mathrm{kin}} + qU \tag{4.1}$$

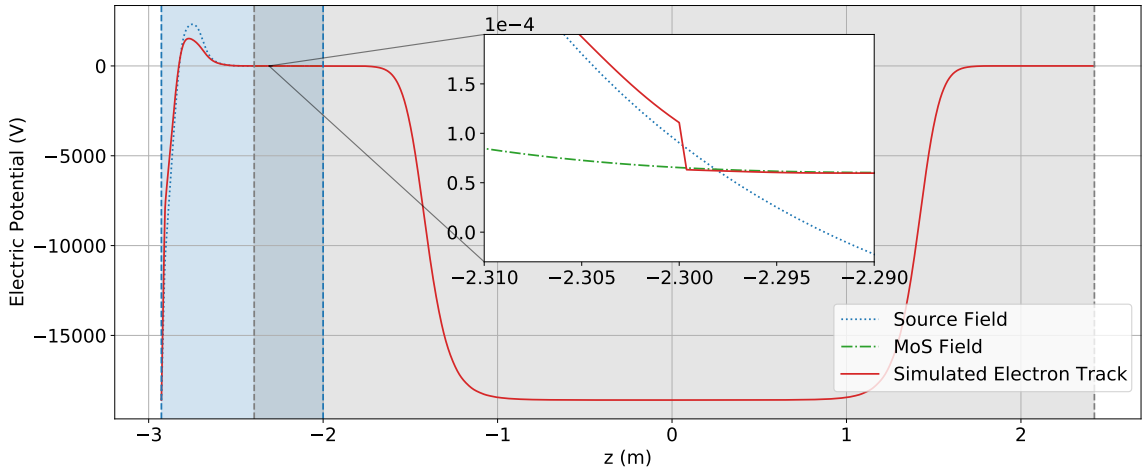

Figure 4.5: Electric potential as a function of the z-coordinate in the monitor spectrometer (MoS). To speed up the simulation, the computation of the charge densities was split up between the first section where the electron source is located (indicated by the blue area) and the second section which contains the MAC-E filter (indicated by the gray area). The electric potential was calculated on the z-axis ($x = y = 0$) using only the charge densities of the source region (blue), as well as only using the MAC-E filter region (green). An electron starting from the source backplate with 0° tilt angle propagates in a small non-negligible cyclotron motion so that the electric potential varies slightly from the ones along the z-axis. The inset shows the break point at $z = -2.3\,\mathrm{m}$ where the source region is swapped with the MAC-E filter section for electric field computation, causing a step of the simulated electrostatic potential. An overlap of geometry elements between both regions (indicated by the gray and blue area) ensures small step sizes.
Here, a backplate voltage of $-18600\,\mathrm{V}$ and a dipole voltage of $3500\,\mathrm{V}$ is used.

and should be conserved for the whole track. At the break point, this energy conservation cannot be ensured, due to the sudden change of qU. By calculating

$$\Delta E_{\mathrm{tot}} = E_{\mathrm{tot}}(\vec{r}) - E_{\mathrm{tot}}(\vec{r_0}) \tag{4.2}$$

where $\vec{r}$ is the position of the particle and $\vec{r_0}$ a defined reference point (here: starting position), one can extract the numerical inaccuracy. In figure 4.6, this relation is depicted for various particle tracks with different starting angles α. The numeric energy violation arising from the split electric field calculation is visible as a step at $z = -2.3\,\mathrm{m}$. Its contribution is $\ll 1\,\mathrm{meV}$ and can therefore be neglected. Beyond this step a continuous loss of energy around $z = \pm 2\,\mathrm{m}$ can be spotted. Two superconducting solenoids which create a maximum magnetic field of $6\,\mathrm{T}$ are located at these positions. This numerical influence is limited, as the step size of the particles is regulated by the software to limit the numerical energy violation per step (The upper limit for the relative energy violation per step is set to 10^{-12}). As the total energy violation over the course of the setup is at maximum on the scale of $1\,\mathrm{meV}$, which is

much smaller than the eV-scale energy resolution of the MoS, numerical inaccuracies can be neglected for analysis.

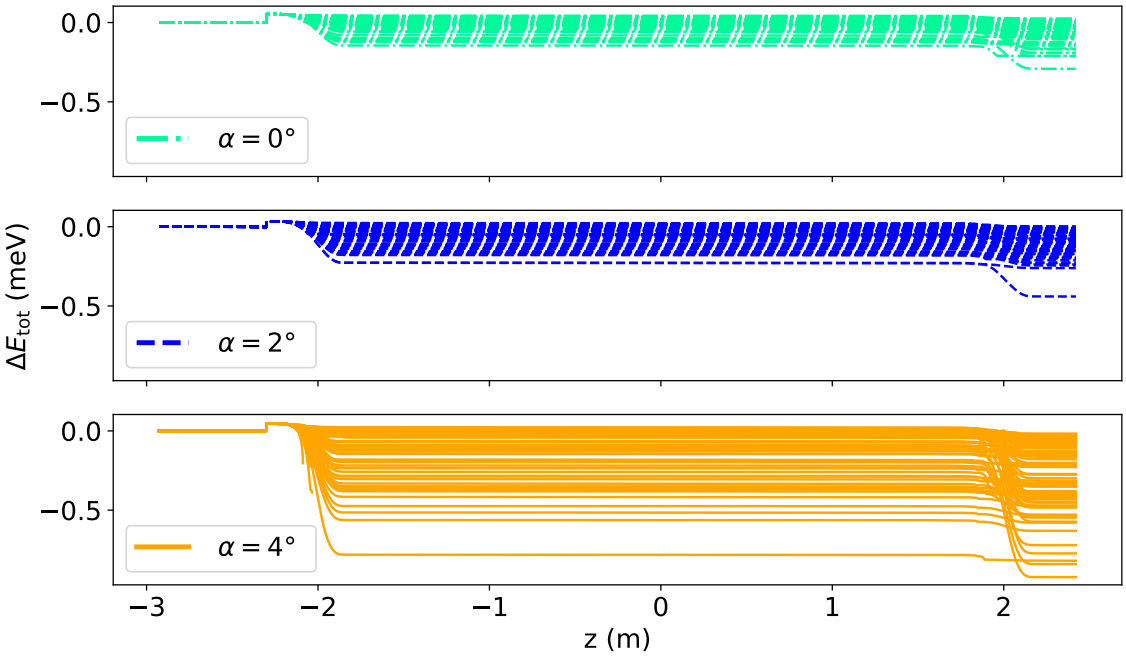

Figure 4.6: Energy violation in the MoS simulation for different plate angles $\alpha = 0°, 2°, 4°$ according to equation (4.2). The simulations used the same settings as in figure 4.5.

The exact tracking method was used over the whole setup. Although this increases computation time, it was shown by earlier studies that simulations including angular-selective electron sources of the type presented in section 3.4 should use exact tracking not only in the source region where the non-adiabatic acceleration process happens [Zac15]. During the commissioning measurements, the source suffered from instability issues at electron energies $> 20\,\mathrm{keV}$. Due to the unique magnetic configuration during the measurements (see section 5.1) and as it was unclear, what the origin of this problem was, electron tracking was performed over the whole setup up to the detector to spot possible sources of the observed effects.

4.2.3 Configuration of the aTEF test setup simulation

The simulation files for the aTEF test setup were already created in an earlier work [Sal19]. In the scope of this thesis, the geometric as well as the general configuration have been refined to further improve the simulation.

A first improvement of the simulation code structure enables an easy interchangeability of the two electron sources. In the latest version, it is possible to switch between both electron sources used in this thesis by simply changing a parameter `egun` from `0` (18 keV source) to `1`

(32 keV source).

Secondly, all changes that have been made to the experiment have been implemented into the simulation. Details on the experimental conditions will be given in chapter 6.

As in the previous chapter, exact tracking along with the step size regulation based on energy violation was used for the entire length of the setup. It has been found that the adiabatic invariant μ (see equation (3.10)) is not necessarily preserved, hence adiabatic tracking, which reduces the computational load but assumes adiabaticity, cannot be used [Sal19].

Due to this configuration, the total numerical energy violation, which is depicted in figure 4.7, is on the order of 0.001 meV and can therefore be neglected.

The simulations include the non-negligible impact of the earth magnetic field. The corresponding values are obtained from the Helmholtz Centre Potsdam [Geo] and are implemented in the simulation as a static magnetic field component with $B_x = -19 \times 10^{-6}\,\mathrm{T}$, $B_y = -45 \times 10^{-6}\,\mathrm{T}$, $B_z = 1 \times 10^{-6}\,\mathrm{T}$, where the axes are defined as depicted and described in figure 6.1.

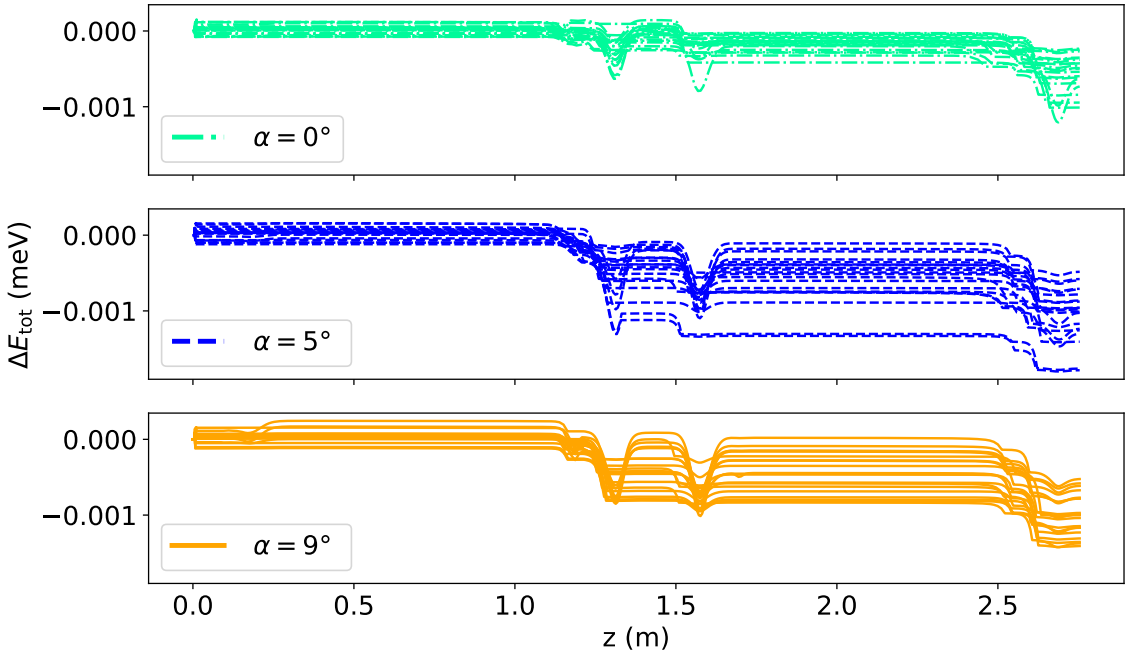

Figure 4.7: Energy conservation violation in the aTEF test setup simulation at different electron source plate angles $\alpha = 0°, 5°, 9°$ according to equation (4.2). These exemplary settings were simulated using the 18 keV source with a backplate voltage of −14 keV and are presented in more detail in section 6.2.

5 Simulations on the upgraded angular-selective electron source at the monitor spectrometer

The development of a 32 keV angular-selective monoenergetic electron source is a crucial asset towards reducing the plasma uncertainty of the KATRIN experiment. First commissioning measurements with the new 32 keV electron source, which was developed in Münster, were performed by L. Schimpf and S. Schneidewind at the monitor spectrometer (MoS) in July 2021. The following chapter is going to present the corresponding particle tracking simulations which complement the analysis of measurement data.
The magnetic field configuration involved the use of coils placed asymmetrically around the beam tube at the electron source position in order to shift the electron beam. The properties of this specific configuration will be presented in section 5.1. Simulation results that present the impact of these on electron transmission are the subject of section 5.2. Finally, in section 5.3 the results are discussed and compared to the measurements.

5.1 Electromagnetic configuration at the monitor spectrometer

The MAC-E filter characteristics of the monitor spectrometer are primarily defined by two superconducting solenoid coils at the entrance and exit of the spectrometer, providing a magnetic field of 6 T. Furthermore, four air coils towards the middle of the spectrometer can be used to control the magnetic field inside the spectrometer. For the following simulations a 3 G setting for the magnetic field in the analyzing plane was used. For the standard energy of 18.6 keV, with which most measurements were performed, this results in an energy resolution of $\Delta E = 18.6\,\mathrm{keV} \cdot \frac{3\times10^{-4}\,\mathrm{T}}{6\,\mathrm{T}} = 0.93\,\mathrm{eV}$.
During the commissioning measurements, the installed detector was, in contrast to the electron source, located off-axis in the upper right quadrant of the flux tube (towards positive x and y). Hence, measures needed to be taken to be able to consistently hit the detector. The easiest solution involved modification of the magnetic field properties at the electron source. Therefore, in addition to an on-axis coil, a further coil (referred to as Hillen coil in

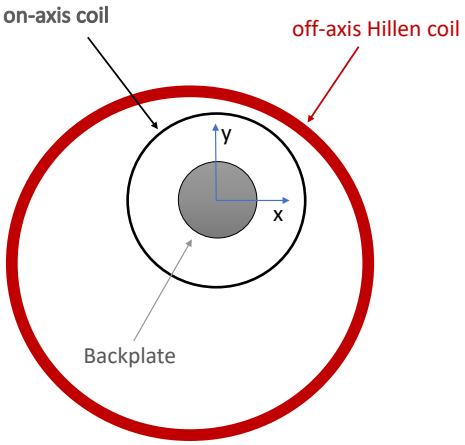

Figure 5.1: Schematic cross-section of the setup geometry at the MoS around the electron source. To be able to hit the detector in the upper right quadrant, the magnetic field at the source needed to be adjusted. Therefore, in addition to an on-axis coil, a further coil ("Hillen coil") was placed off-center, so that the electron source lies in the upper right quadrant of the magnetic fluxtube.

the following [Hil11]) was installed off-axis around the source. A schematic illustration of this configuration is shown in figure 5.1. The shift of the Hillen coil as it is implemented in the simulation is -1.8 cm in x-direction and -6.3 cm in y-direction. This information was measured by hand and can therefore deviate by several mm from the measurement conditions. The position of the Hillen coil effectively shifts the magnetic fluxtube so that electrons starting on the backplate of the electron source follow magnetic field lines that terminate on the off-axis detector.

In the following, the on-axis coil is operated at 10 A and the Hillen coil at 47.5 A, which results (including stray field from 6 T solenoid) in a magnetic field of 35 mT at the electron source.

As the frontplate of the electron source is not rotationally symmetric, information on how the source was installed is important. In the following, the source is either installed with the wide side of the slit parallel to the y-axis (vertical) or with the wide side of the slit parallel to the x-axis (horizontal). Tilting in the simulation can be performed both in x-direction (left and right) or in y-direction (up and down).

Since this approach, where an off-axis coil directly affects the acceleration process of electrons from an angular-selective photoelectron source, has never been tested before, simulations are needed to understand the measurement results.

5.2 Angular selectivity simulations

In the context of the commissioning measurements of the 32 keV electron source, the following simulation results aim to qualitatively describe the transmission properties of the electron source using the novel off-axis coil configuration. As the magnetic field of a cylindrical coil is highly inhomogeneous in outer regions of the flux, the corresponding magnetic field lines exhibit an angle towards the z-axis. Therefore, in section 5.2.1 zero angle simulations aim to show how this inhomogeneity impacts the produced electron angles. In sections 5.2.2 and 5.2.3 simulations investigating the transmission properties at different source conditions are presented.

5.2.1 Zero angle

As discussed in section 3.4, the plate capacitor setup of the electron source can be tilted in different directions to imprint a pitch angle θ relative to the magnetic field on the generated electrons. The plate angle α_p is defined with respect to the direction of the magnetic field. However, as the magnetic field in this case is highly inhomogeneous, α_p can vary by several degrees from the geometrically defined angle α, which is defined relative to the z-axis. To produce electrons with minimal pitch angles θ, one must therefore first determine the so-called zero angle α where $\alpha_p = 0$. This information is furthermore very useful to be able to interpret the simulations on transmission properties in the next sections.

To determine the zero angle, the spectrometer must be set to half-transmission where the transmission probability is ≈ 0.5 (compare figure 3.6). Here, the transmission probability is most sensitive to changes of the electron angle so that variation of the plate angle results in a noticeable change of the electron rate. The resulting distribution can be approximated with a Gaussian distribution

$$f(\alpha) = \frac{A}{\sqrt{2\pi\sigma^2}} \exp\left[-\frac{(-\alpha - \alpha_0)^2}{2\sigma^2}\right] \tag{5.1}$$

to calculate the zero angle α_0 with amplitude A and width σ [Beh17]. As the simulation does not include background, a constant offset can be omitted.

Simulations for the zero angle were carried out using $N = 1000$ Monte-Carlo generated electrons per plate angle setting. Plate angles were independently varied both in x- and y-direction (α_x, α_y). An acceleration voltage of $U_{\text{acc}} = 11\,\text{kV}$ at $U_{\text{back}} = -18.6\,\text{kV}$ was set and dipole voltages were varied between 2500 V and 3500 V. The results are depicted in figure 5.2. The plot shows the transmission ratio N_t/N where N_t is the number of transmitted electrons. Error bars indicate $\sqrt{N_\text{t}}$. The fits are calculated with the `curve_fit()`-function of the scipy package [Vir+20] which uses the least squares method. The fitted zero angles are depicted in table 5.1.

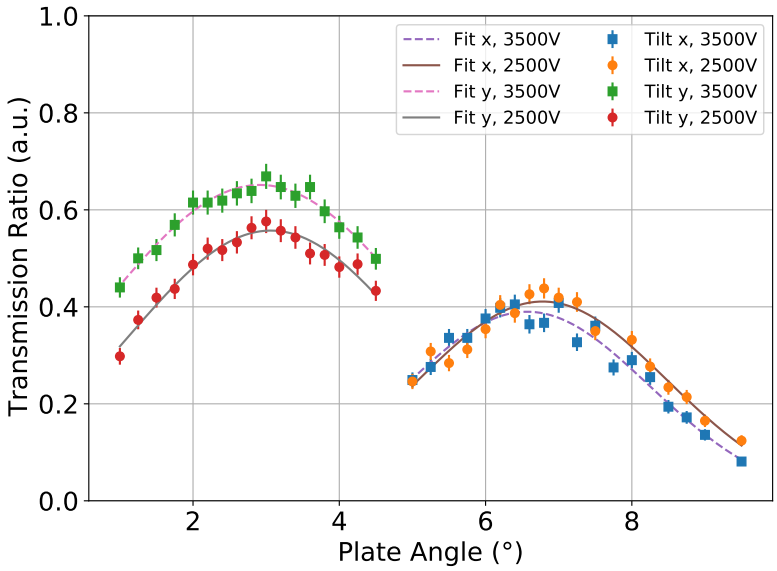

Figure 5.2: Simulation of the transmission ratio as a function of the plate angle to calculate the zero angle for the MoS configuration with off-axis Hillen coil. The electron source was installed vertically and tilted in x- and y-direction. The backplate voltage is set to $U_{\text{back}} = -18.6\,\text{kV}$ with an acceleration voltage of $U_{\text{acc}} = 11\,\text{kV}$. Simulations were carried out with different dipole voltages 2500 V and 3500 V which indicate the impact of the dipole electrode on electron transmission. Per setting, 1000 electrons were simulated. Determination of the zero angle is most sensitive when the retarding voltage is set to the half-transmission point. Therefore, a retarding voltage of $-18600.3\,\text{V}$ was applied when tilting in x-direction and $-18599.9\,\text{V}$ was applied when tilting in y-direction. Positive angles correspond to tilting upwards (y) or rightwards (x).

The simulations depict a clear dependency of the transmission ratio on the plate angle. Both tilt directions show a clear offset from 0° which indicates the impact of the off-axis Hillen coil. Thereby, a larger offset is found for tilting in x-direction (approx. 3.7°) which is unexpected as the shift of the Hillen coil is larger in y-direction than in x-direction. However, since the center of the Hillen coil lies 3 cm behind the photocathode (see figure 4.4), the magnetic field around the frontplate is highly inhomogeneous. This simulation therefore shows the non-triviality of the problem at hand.

Furthermore, the dipole electrode also has a significant impact on the pitch angle, causing a difference of $(0.15 \pm 0.07)°$ in y-direction and $(0.21 \pm 0.06)°$ in x-direction. A larger dipole voltage thereby corresponds to a smaller zero angle. This is also indicated by the increased transmission at 3500 V.

This study showed that the off-axis coil configuration has a significant impact on the pitch angle and therefore on transmission properties. It therefore gives a general idea on the pitch angle generation and can be used as a baseline for further transmission studies that are

Table 5.1: Simulated zero angles at different dipole voltage settings.

Dipole Voltage	Tilt Direction	Fit Values
3500 V	x	$(6.57 \pm 0.05)°$
	y	$(2.91 \pm 0.03)°$
2500 V	x	$(6.78 \pm 0.04)°$
	y	$(3.06 \pm 0.06)°$

presented in the next sections. It has to be noted, though, that the zero angle is in principle affected by every change of electromagnetic field properties around the source. Hence, the results depend on the chosen settings and therefore cannot be universally applied to all of the simulations presented in the next subchapters. However, they give a basis for comparisons and a clear indication of what is to be expected from further simulations.

5.2.2 Magnetic cutoff

Magnetic reflection simulations are another useful tool to investigate the produced pitch angles. In section 3.2 it was discussed that, when an electron adiabatically moves into a region with higher magnetic field, the pitch angle increases. If it exceeds 90°, magnetic reflection occurs. Due to the magnetic field $B_{\mathrm{src}} = 35\,\mathrm{mT} \ll B_{\mathrm{max}} = 6\,\mathrm{T}$, the required pitch angle in the source magnetic field can be significantly smaller to achieve 90° pitch angle at the superconducting solenoids. Since angular-selectivity over the full angular range up to 90° at the maximum magnetic field is a critical factor regarding the functionality of the electron source, knowledge of this property is especially important in this special electromagnetic environment. Hence, in the following, simulations that investigate the magnetic cutoff are presented.

For investigations of the magnetic cutoff angle, the spectrometer must be set to full transmission, meaning that a constant retarding potential well below the electrostatic transmission edge is applied. This guarantees that the transmission ratio is only affected by magnetic reflection and not influenced by any electrostatic reflection. In the following, the spectrometer voltage was set to a surplus voltage of 2 eV or a retarding voltage of −18598 V. To match measurement settings, a voltage of 3500 V was applied to the dipole electrode. The electron source was installed with the slit parallel to the x-axis (horizontal) and parallel to the y-axis (vertical). For the former, tilting was done in x-direction (around y-axis) while for the latter tilting was done in y-direction (around x-axis). Positive plate angles correspond to tilting rightwards or upwards, respectively.

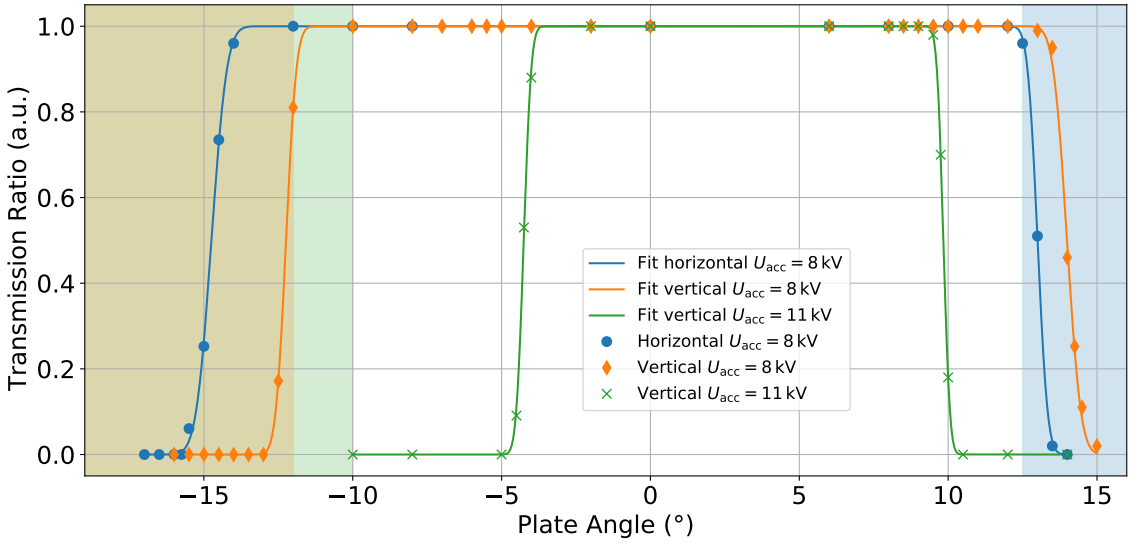

Figure 5.3: Simulated magnetic cutoff scans for different electron source installations and acceleration voltages U_{acc} with corresponding fit. In the horizontal setting, the source was installed with the frontplate opening slit parallel to the x-axis and tilting was performed in x-direction while in the vertical setting the slit is parallel to the y-axis and tilting was performed in y-direction. The colored zones indicate settings where at least one electron could not exit the source through the opening of the frontplate. 100 electrons were simulated per plate angle. The dipole voltage was set to 3500 V, with the retarding potential at −18598 V, which corresponds to a surplus energy of 2 eV.

Figure 5.3 shows the result of three magnetic cutoff simulations at $U_{\mathrm{back}} = -18.6\,\mathrm{kV}$ featuring both tilt directions at acceleration voltage $U_{\mathrm{acc}} = 8\,\mathrm{kV}$ and, furthermore $U_{\mathrm{acc}} = 11\,\mathrm{kV}$ in vertical direction. As the respective tilt directions were also investigated for positive and negative angles, two transmission edges are visible. The data was therefore modeled via

$$f(\alpha) = 1 - \frac{1}{2}\left[1 + \mathrm{erf}\left(\frac{\alpha - \alpha_-}{\sqrt{2}\sigma_-}\right)\right] - \left[1 - \frac{1}{2}\left(1 + \mathrm{erf}\left(\frac{\alpha - \alpha_+}{\sqrt{2}\sigma_+}\right)\right)\right] \tag{5.2}$$

where α_+, σ_+ are the magnetic cutoff angle and transmission width for positive plate angles, whereas α_-, σ_- are the respective parameters for negative plate angles and erf is the Gauss error function. The corresponding fit values can be found in table 5.2. Furthermore, it has to be said that the error function is not a physically correct description of the transmission, but rather a numerical approximation to be able to qualitatively compare the simulation data. Note that for a complete study on systematic uncertainties, a Monte-Carlo study investigating the effect of every parameter that is connected to an uncertainty would need to be carried out. These parameters include e.g. the randomized variables such as initial kinetic energy and momentum vector or the position of the Hillen coil. For this, many transmission

functions would have needed to be simulated. Although computing was performed on the institute's local cluster using up to 100 cores simultaneously, computation times of one plot are on the order of multiple days. Therefore, error bars are left out in this and all following plots that show transmission function simulations.

The impact of the non-axial coil setup can also be seen in this case. Due to the zero angle shift (compare figure 5.2), the functions are asymmetric around 0°. This is especially visible for the vertical scan with $U_{\mathrm{acc}} = 11\,\mathrm{kV}$ because this simulation was not influenced by other effects affecting the transmission. Both simulations with $U_{\mathrm{acc}} = 8\,\mathrm{kV}$ have exactly one transmission edge where electrons are absorbed by the frontplate ($-12°$ vertical, 12.5° horizontal), indicated by the colored areas in figure 5.3. These electrons are unable to exit the electron source through the frontplate slit, meaning that these settings cannot be used to investigate the full 90° range of the spectrometer. Exemplary particle tracks, which demonstrate the point of impact on the wide side of the frontplate slit using $U_{\mathrm{acc}} = 8\,\mathrm{kV}$ and $\alpha = -14°$ (vertical) are depicted in appendix A.2.

The simulation with $U_{\mathrm{acc}} = 11\,\mathrm{kV}$ indicates that this problem can be avoided by setting a larger acceleration voltage. This curve is significantly narrower than the others which demonstrates that an increase of U_{acc} leads to larger pitch angles after the acceleration process. Therefore, the full 90° range can be scanned before electrons begin to hit the frontplate. The angle at which the frontplate is first hit is $-10°$ in this setting. Since this value is lower than the respective value for $U_{\mathrm{acc}} = 8\,\mathrm{kV}$, a contribution of the $\vec{E} \times \vec{B}$-drift, which is proportional to the electric field strength, is indicated. The corresponding velocity $\vec{v}_E$ is calculated with [Jac99]

$$\vec{v}_E = \frac{\vec{E} \times \vec{B}}{B^2}, \tag{5.3}$$

where $\vec{E}$ is the electric field vector and $\vec{B}$ is the magnetic field vector. From the simulation output an estimate on the total $\vec{E} \times \vec{B}$-drift distance can be calculated. At $U_{\mathrm{acc}} = 8\,\mathrm{kV}$ and $\alpha = -14°$ (vertical) and an estimated drift time of 0.78 ns, a drift distance of $\approx 2.7\,\mathrm{mm}$ in x-direction can be inferred. This value is smaller than the width of the frontplate slit of about 3.5 mm, thus this effect cannot be solely reduced to the $\vec{E} \times \vec{B}$-drift. The corresponding particle tracks show that a cyclotron motion can already be observed between front- and backplate. From the simulation output a cyclotron radius of approximately 1 mm is calculated. The sum of $\vec{E} \times \vec{B}$-drift distance with the cyclotron radius is in agreement with the observed total drift in x-direction of 3.7 mm. Therefore, it can be concluded that the combination of cyclotron motion and $\vec{E} \times \vec{B}$-drift is likely the reason for the observed termination of electrons on the frontplate.

Looking at the angular width (σ_+, σ_-) one finds not only a significant reduction at $U_{\mathrm{acc}} = 11\,\mathrm{kV}$

in comparison to the pure magnetic reflection edges of $U_{\mathrm{acc}} = 8\,\mathrm{kV}$ but also an increased transmission width when electrons hit the frontplate. These values, however, are highly dependent on the underlying start parameters of electrons at the photocathode. As these can differ from the simulated distributions, the absolute values shall only be seen as a reference that can predict a general trend.

The cutoff angles at $U_{\mathrm{acc}} = 11\,\mathrm{kV}$ can also be used to calculate the zero angle: With $\alpha_0 = (\alpha_+ + \alpha_-)/2 = (2.79 \pm 0.01)^\circ$ one can conclude that it matches with the zero angle calculation from the previous chapter (compare table 5.1) within 3σ.

Table 5.2: Fit values of magnetic cutoff simulation for different electron source installations and acceleration voltages U_{acc}. Here, α_+ and σ_+ are the magnetic cutoff angle and transmission width for positive plate angles, whereas α_- and σ_- are the respective parameters for negative plate angles.

U_{acc} (kV)	Tilt direction	α_+ (°)	σ_+ (°)	α_- (°)	σ_- (°)
8	Horizontal	(13.00 ± 0.01)	(0.27 ± 0.01)	(-14.75 ± 0.01)	(0.41 ± 0.01)
	Vertical	(13.99 ± 0.01)	(0.37 ± 0.01)	(-12.24 ± 0.01)	(0.27 ± 0.01)
11	Vertical	(9.84 ± 0.01)	(0.17 ± 0.01)	(-4.26 ± 0.01)	(0.20 ± 0.01)

Finally, it can be said that the 32 keV electron source is capable of scanning the whole angular range up to 90° at the given magnetic field settings. Thereby, larger acceleration voltages are to be favored as transmission can be limited by the electron source itself. Furthermore, the impact of the off-axis coil setup, which results in a shifted zero angle, can also be tracked using the magnetic reflection simulation.

5.2.3 Transmission function shifts

The previous sections already gave a brief overview of the pitch angle creation mechanisms of the electron source. Pitch angles can be varied not only via the plate angle but also by variation of the acceleration voltage at a constant plate angle. Both mechanisms were investigated during the commissioning measurements at the MoS. Hence, corresponding simulations at $U_{\mathrm{back}} = -18.6\,\mathrm{kV}$ were computed and are presented in the following.

Transmission function simulations at constant $U_{\mathrm{acc}} = 12\,\mathrm{kV}$ and dipole voltage 2500 V with varying plate angles from 0° to 9.5° are depicted in figure 5.4. The step size of 1.9° corresponds to 1 mm offset of the motor that steers the plates. For one transmission scan, the retarding potential U_{ret} is changed in 0.1 V steps. Hence, the transmission ratio is given as a function of the surplus energy $E_{\mathrm{surp}} = qU_{\mathrm{back}} - qU_{\mathrm{ret}}$. The transmission functions are fit with a single error function:

$$f(E_{\mathrm{surp}}) = A \cdot \left[1 - \frac{1}{2}\left(1 + \mathrm{erf}\left(\frac{\mu - E_{\mathrm{surp}}}{\sqrt{2}\sigma}\right)\right)\right], \tag{5.4}$$

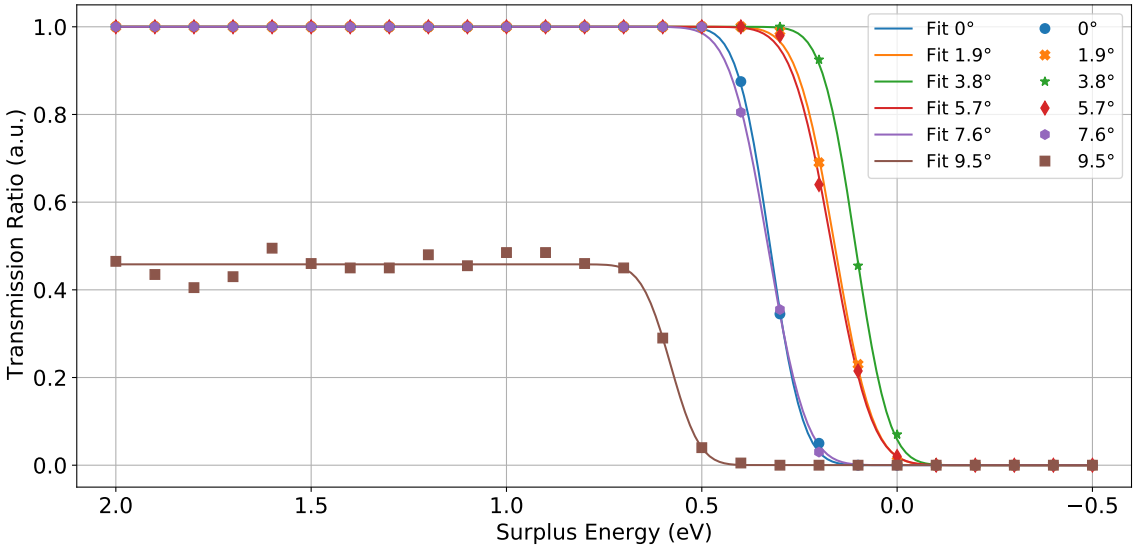

Figure 5.4: Simulated transmission function scans for different plate angles α at $U_{\mathrm{acc}} = 12\,\mathrm{kV}$ with corresponding fit. Per retarding potential 200 electrons were simulated. The dipole voltage was set to 2500 V. A plateau of the transmission ratio at larger surplus energies indicates magnetic reflection. The electron source was installed vertically.

where μ is the position of the transmission edge and σ is the transmission width. The amplitude parameter A is only free when a plateau smaller than 1 at $E_{\mathrm{surp}} > \mu$ is reached. Otherwise, this parameter is set to 1. The corresponding fit values are depicted in table 5.3. The transmission curves show a clear dependency on the plate angle. Higher plate angles correspond to larger shifts of the transmission function. However, due to the non-corrected large zero angle, the transmission corresponding to $\alpha = 3.8°$ shows the smallest shift. As the transmission edge for 0° overlaps with 7.6° as well as 1.9° with 5.7° and a symmetric distribution around the zero angle is assumed, one can conclude that the zero angle in this case, where $U_{\mathrm{acc}} = 12\,\mathrm{kV}$, is $\approx 3.8°$. This value is significantly larger than the zero angle of $(3.06 \pm 0.06)°$, which was observed in table 5.1. This indicates that the acceleration voltage also has an influence on the zero angle in the inhomogeneous magnetic field of the monitor spectrometer. In perfectly homogeneous conditions, the zero angle is expected to be independent of this property.

At 9.5° a plateau of the transmission ratio at large surplus energies is visible. Here, some electrons are magnetically reflected so that the transmission ratio cannot reach 1, even at high surplus energies. The observable fluctuations at large surplus energies originate from the randomized starting parameters in combination with the total number of simulated electrons. The angle at which magnetic reflection happens is in accordance with the results from figure 5.3.

Table 5.3: Fit values of transmission functions with varying plate angle α. The underlying simulations were computed with a vertically installed source, as well as $U_{\mathrm{acc}} = 12\,\mathrm{kV}$ and dipole voltage 2500 V. Here, μ is the position of the transmission edge and σ is the transmission width. The amplitude parameter A is only free when a plateau smaller than 1 at surplus energies $E_{\mathrm{surp}} > \mu$ is reached.

Plate angle (°)	μ (eV)	σ (eV)	A
0	(0.325 ± 0.001)	(0.066 ± 0.001)	1
1.9	(0.160 ± 0.001)	(0.077 ± 0.001)	1
3.8	(0.106 ± 0.001)	(0.068 ± 0.001)	1
5.7	(0.167 ± 0.001)	(0.081 ± 0.002)	1
7.6	(0.331 ± 0.001)	(0.077 ± 0.001)	1
9.5	(0.580 ± 0.006)	(0.059 ± 0.009)	(0.458 ± 0.005)

Table 5.4: Fit values of transmission functions with varying acceleration voltage U_{acc}. The underlying simulations were computed with a vertically installed source, as well as $\alpha = 9.5°$ and dipole voltage 2500 V. Here, μ is the position of the transmission edge and σ is the transmission width. The amplitude parameter A is only free when a plateau smaller than 1 at surplus energies $E_{\mathrm{surp}} > \mu$ is reached.

U_{acc} (kV)	μ (eV)	σ (eV)	A
3	(-0.102 ± 0.001)	(0.080 ± 0.001)	1
5	(-0.113 ± 0.001)	(0.073 ± 0.001)	1
7	(0.167 ± 0.001)	(0.084 ± 0.002)	1
9	(0.399 ± 0.001)	(0.076 ± 0.002)	1
11	(0.550 ± 0.002)	(0.072 ± 0.002)	(0.955 ± 0.002)
13	(0.534 ± 0.081)	(0.027 ± 0.062)	(0.050 ± 0.002)

The maximum distance between transmission functions of approximately 0.5 eV is smaller than the energy resolution of the MoS, which was 0.93 eV in this setting. This is expected due to the uncorrected zero angle.

In figure 5.5 transmission scans with constant plate angle 9.5° show that a shift can also be induced by varying U_{acc}. The data is again fit with equation (5.4) and the corresponding fit values are presented in table 5.4. The shift of the transmission functions is thereby proportional to U_{acc}, meaning that larger acceleration voltages lead to shifts of the transmission edge towards larger surplus energies. This, however, is only valid until $U_{\mathrm{acc}} = 5\,\mathrm{kV}$ as the corresponding curve shows a strong overlap with the transmission curve for $U_{\mathrm{acc}} = 3\,\mathrm{kV}$. At 13 kV and 11 kV magnetic reflection occurs, limiting transmission at high surplus energies. Therefore, it can be concluded that the voltage difference between front- and backplate has a significant impact on the produced pitch angles. The maximum distance between transmission functions in this study is about 0.6 eV. Although this value is larger compared to the

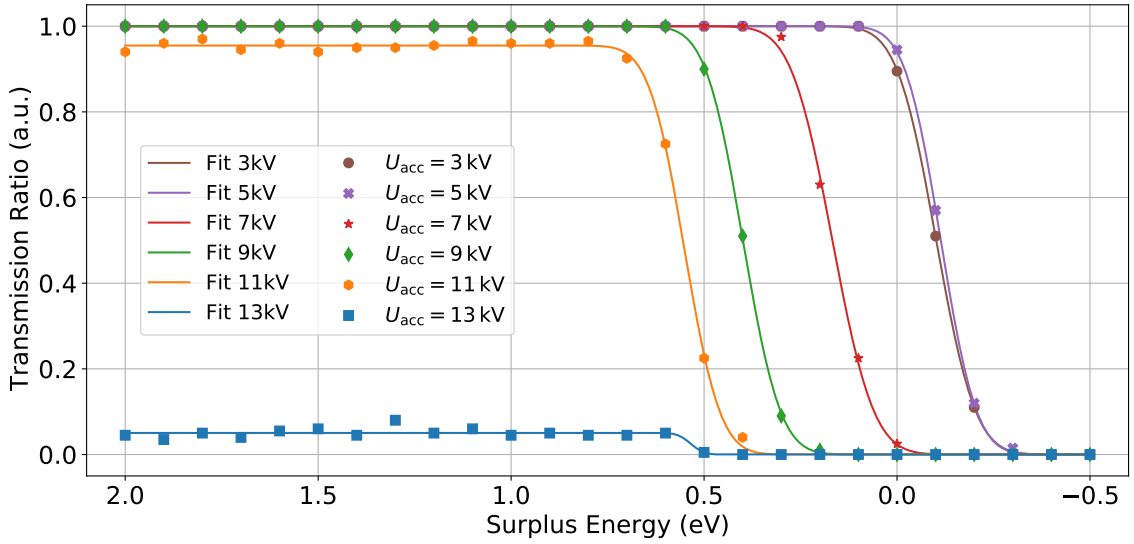

Figure 5.5: Simulated transmission function scans with constant plate angle $\alpha = 9.5°$ for different acceleration voltages U_{acc} with corresponding fit. The dipole voltage was set to 2500 V. Per retarding potential 200 electrons were simulated. A plateau of the transmission ratio at larger surplus energies indicates magnetic reflection. The electron source was installed vertically.

total shift observed in figure 5.4, it still does not cover the whole transmission width of the spectrometer.

The transmission widths are mostly determined by the energy distribution of electrons at the photocathode. In the simulation a Gaussian energy distribution with a width of 0.075 eV is used, which is close to the obtained fit values in tables 5.3 and 5.4. The values fluctuate when varying α and U_{acc}, however no proportionality can be inferred. For more conclusive studies on this parameter, simulations should be performed using either a larger total amount of electrons or more setpoints.

Moreover, the simulation data suggests that the width is reduced when magnetic reflection occurs. The more transmission is dominated by magnetic reflection, which is indicated by a small amplitude parameter A, the smaller the transmission width. However, this is also connected to a larger uncertainty.

The transmission scan simulations show a clear picture of what is to be expected from measurements. However, the experimental situation can differ from the assumptions made in the simulation. Therefore, in the next section the presented results are put into context by comparison with the corresponding measurements.

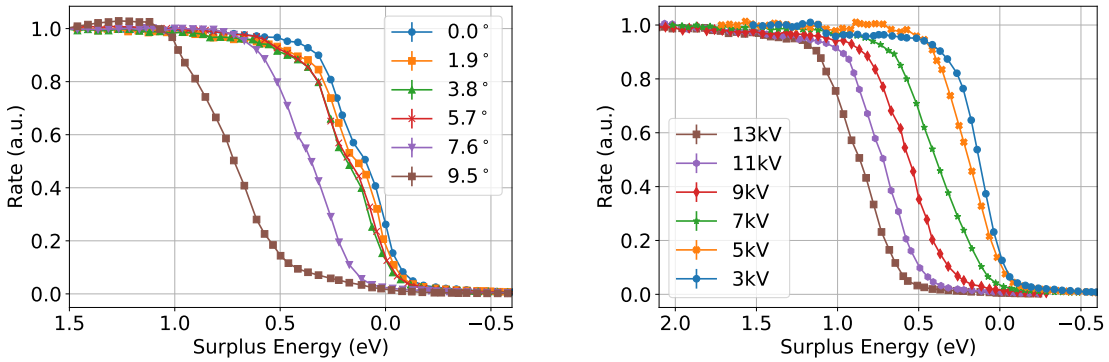

(a) (b)

Figure 5.6: Measured transmission functions for different plate angles α at $U_{\mathrm{acc}} = 12\,\mathrm{kV}$ (a) and with constant plate angle $\alpha = 9.5°$ for different acceleration voltages U_{acc} (b). The corresponding simulations are found in figure 5.4 and figure 5.5. Figures adapted from [Sch+21].

5.3 Discussion and comparison with experimental results

Some exemplary measurement sets of transmission function scans performed at the monitor spectrometer are depicted in figure 5.6(a), which shows the transmission properties for varying plate angles, and figure 5.6(b), which presents these for varying U_{acc} at 9.5° plate angle. The respective settings correspond to the simulation results presented in the previous section.

Beginning with figure 5.6(a), it is again easy to spot a shift of the transmission functions depending on the plate angle. At $\alpha = 9.5°$ the largest shift can be seen, while in this case $\alpha = 0°$ shows the smallest shift. The functions with angles between $\alpha = 0°$ and $\alpha = 5.7°$ lie close together within 0.1 eV. Furthermore, a plateau due to magnetic reflection at large plate angles does not occur. This is partially due to the normalization procedure in this case, as the depicted rate is given relative to the rate at the largest surplus energy. Therefore, the rate can also obtain values larger than 1. Furthermore, magnetic reflection measurements showed, that a rate drop is spotted only at plate angles larger than 10°. This is, although it is slightly larger, in accordance with the simulation results. Since the width of the transmission function at $\alpha = 9.5°$ is comparable with the width of the other transmission functions, it is probable that magnetic reflection did not occur here.
Generally, the transmission shift of plate angles $\alpha \geq 5.7°$ is in agreement with simulation results. The largest difference is obtained for $\alpha = 0°$ which now has the smallest shift, indicating a zero angle close to $\alpha = 0°$. This, however, contradicts the observation that the transmission functions of $\alpha = 5.7°$ and $\alpha = 3.8°$ overlap and lie close to the transmission

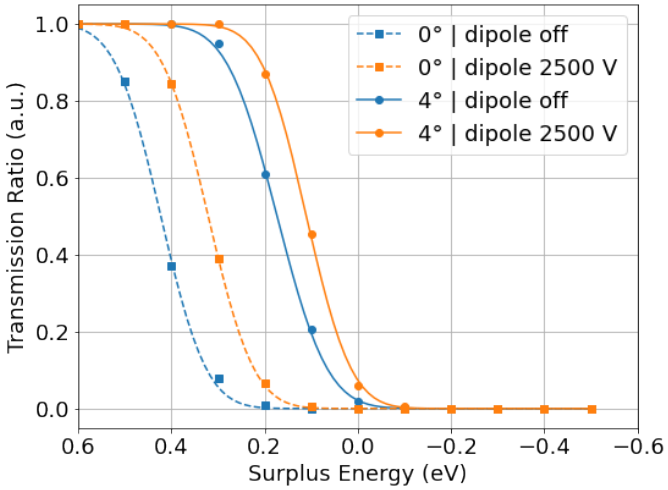

Figure 5.7: Comparison of simulated transmission functions with different dipole voltages at 0° and 4° plate angle. Per retarding potential, 200 electrons were simulated. The electron source was installed vertically and set to $U_{\mathrm{acc}} = 12\,\mathrm{kV}$ with $U_{\mathrm{back}} = -18.6\,\mathrm{kV}$.

functions of $\alpha = 0°$ and $\alpha = 1.9°$, as simulations indicate an increased shift for larger distances to the zero angle. The reason for that is likely a defect of the tilting mechanism of the electron source, which was later discovered. As this caused ambiguous plate angles at different motor positions, the main discrepancies between measurement and simulation could be explained by this.

However, there are other possible explanations that could cause deviations from the simulations, e.g. a difference between the simulated and experimental electromagnetic conditions. Although a different position of the Hillen coil would effectively only affect the zero angle, the dipole electrode could introduce significant deviations from the expected behavior. In figure 5.7 a comparison of the impact of the dipole electrode for different plate angles is shown. The dipole electrode primarily affects the position of the transmission function. While at $\alpha = 4°$ the transmission function shift between 0 V and 2500 V is only 0.06 eV, the shift is 0.1 eV at $\alpha = 0°$. Therefore, transmission is affected differently by the dipole electrode depending on the plate angle. It is possible, that the experimental geometry is not represented perfectly in the simulation which could allow the measured behavior. A mechanical issue or other electromagnetic influences that are not included in the simulation can also not be ruled out.

Focusing on figure 5.6(b), simulations and measurement are generally in good agreement with each other. Transmission function shifts for the different acceleration voltages are consistent with 3 kV and 5 kV having the smallest shift while 13 kV has the largest shift. Again,

magnetic reflection was not seen during measurement which is in agreement with the measured magnetic cutoff angle of 12° [Sch+21].
The width of the measured transmission functions is generally larger than in the simulation. This can, among other things, be connected to the wavelength of the light source, as well as the work function of the photocathode. As these parameters have not been adapted for the new electron source, a discrepancy in this regard is expected but does not significantly change the qualitative transmission behavior.

In conclusion, simulation of the transmission properties for this novel off-axis coil configuration could characterize the expected behavior of the setup for different configurations. The shift of the flux tube to hit the detector, which was placed off-axis, is in principle a useful mechanic. However, the resulting highly inhomogeneous magnetic field needs to be carefully corrected to be able to do precise measurements whilst understanding all systematic effects. Based on the simulation results, the setup was modified for a second measurement campaign. Featuring an axially symmetric magnetic field, a more comprehensive characterization could be performed.

6 Electron tracking simulations for the aTEF test setup

It was discussed in chapter 3 that background electrons originating from the ionization of highly excited (Rydberg) atoms are currently one of the most dominant background processes of KATRIN. A feasible approach to mitigate the impact of this component on the neutrino mass sensitivity of KATRIN might be the implementation of an active transverse energy filter (aTEF). Prototypes based on Si p-i-n diodes are currently investigated in Münster. To be able to reliably test the aforementioned prototypes, a good understanding of the characteristics of the test setup is required. Therefore, the work presented in this chapter aims to not only provide accurate simulation results for the analysis and interpretation of measurement data but also to optimize the experimental conditions.
The measurement idea and general properties of the test setup are discussed in section 6.1. A method the verify the simulation accuracy along with the corresponding results is presented in section 6.2. Section 6.3 aims to explain the obtained results while several ways to improve the test environment are presented in section 6.4 .

6.1 How to examine angular selective detection properties

An overview of the aTEF test setup is given in figure 6.1. First introduced in [Sal19], it was originally designed for time-of-flight measurements in relation to KATRIN [Ful+20; Ste+13]. Recently, it has successfully been used for proof-of-principle measurements of MCPs acting as transverse energy filters [Oel21; Kön21]. The 3 m long setup mainly consists of two beam tubes that are surrounded by several coils that define a guiding magnetic field for electron transport. In the following, important elements of the setup will be presented, starting at the electron source and ending at the detector.
At the left end of the setup, an angular-selective monoenergetic photoelectron source as it was presented in section 3.4 is mounted. In the scope of this thesis, both the 32 keV source as

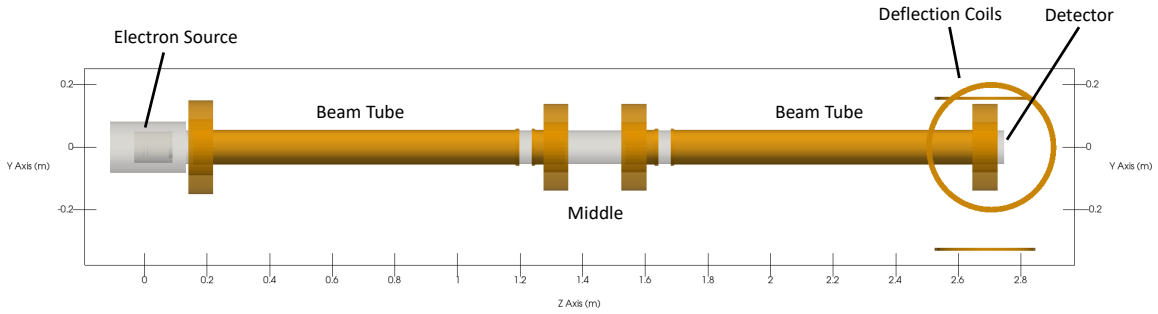

Figure 6.1: Overview of the aTEF test setup in Münster showing the geometry as it is used in the particle tracking simulations. An angular-selective monoenergetic photoelectron source is placed in the source chamber at $z \approx 0\,\mathrm{m}$. Various coils (orange) create a guiding magnetic field for the propagation of electrons through the beam tubes. Around the detector, four deflection coils are placed allowing to steer electrons towards the detector at the end of the setup. The x-axis points out from the depicted plane.

well as the 18 keV source were used at some point. One of four anoxal®[1] (anodized oxidized aluminum) coils is placed at the entrance of the first 1.23 m long beam tube to create the source magnetic field B_{src}. Further two anoxal® coils are located around the middle of the setup, where a cubical vacuum chamber with a pressure gauge, a vacuum pump and an additional port for exchangeable components is located. For the aforementioned proof-of-principle measurements the filter MCP was placed in the center of that chamber. The last coil of this type is situated around the detector at the right end of the second beam tube and delivers the magnetic field B_{det}. This configuration allows to adiabatically control the pitch angle θ, so that, according to equation (3.13), the pitch angle at the detector is defined via

$$\theta_{\mathrm{det}} = \arcsin\left(\sin(\theta_{\mathrm{src}})\sqrt{\frac{B_{\mathrm{det}}}{B_{\mathrm{src}}}}\right), \tag{6.1}$$

where θ_{src} is the pitch angle inside the source magnet. Thus, by tuning the magnetic field ratio $B_{\mathrm{det}}/B_{\mathrm{src}}$ and choosing an appropriate plate angle of the electron source, the desired pitch angles can be produced.
Furthermore, to control the magnetic field and, thus, preserve adiabatic conditions in the regions between the anoxal® coils a solenoid coil is wound around each beam tube (chamber coils). A small gap towards the middle of the setup indicates the position of two CF40 flanges.

The detector prototypes are installed inside a dedicated holding structure which is directly connected to a charge-sensitive preamplifier [Jöh13] and can hold up to two diodes. An

[1] Umwelttechnik Wesselmann GmbH, Auf dem Knuf 21, 59073 Hamm, Germany

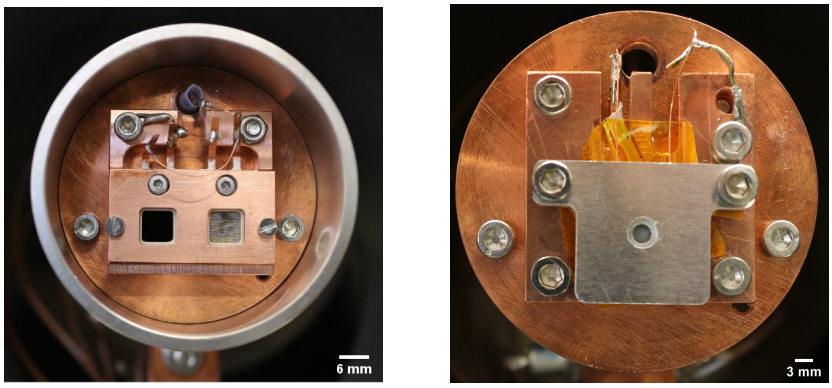

(a) (b)

Figure 6.2: Pictures of the holding structures used to mount the diodes to the preamplifier system. With the structure shown in a), up to two diodes can be installed side by side. The quadratic apertures feature side lengths of 6 mm. The circular aperture for a single diode shown in b) has a diameter of 3 mm. Images taken by K. Gauda.

aperture in front of the detector ensures that only the microstructured regions can be hit by electrons. Two of these holding structures are depicted in figure 6.2.
To overcome the difficulty to hit the small active surface area, a total of four additional deflection coils are located around the detector to actively steer incoming electrons towards the diodes. As depicted in figure 6.3, these coils are grouped into two pairs (vertical and horizontal) that are rotated by 90° with respect to each other. The coils of each pair are oriented such that their primary magnetic field component is parallel to their symmetry axis. Hence, in the detector plane, electrons can be steered both in x- and y-direction. Although each coil of a pair has the same hardware parameters such as total windings, thickness and radius, both groups differ in these parameters. The parameters of both groups are listed in table 6.1. Another important aspect is the placement of the coils relative to the detector position. The vertical coils are situated symmetrically around the y-z-plane at $x = \pm 0.22\,\mathrm{m}$. The horizontal deflection coils, however, do not feature the same distance to the x-z-plane. The upper coil is located at $y = 0.156\,\mathrm{m}$ whereas the lower coil is located at $y = -0.326\,\mathrm{m}$. Experimentally, this was unavoidable due to limited space at the detector section.

To summarize, this test setup, due to the angular-selective electron source and its tunable guiding magnetic field, is able to produce electrons with variable pitch angles to probe the Si-aTEF prototypes. For the correct interpretation of measurement data, precise knowledge about the pitch angle at the detector is necessary. As the involved processes, such as the non-adiabatic acceleration inside the electron source or the impact of the deflection coils are non-trivial, electron tracking simulations are required. Before the results of these can be discussed, thorough investigations that examine the simulation accuracy were necessary. This

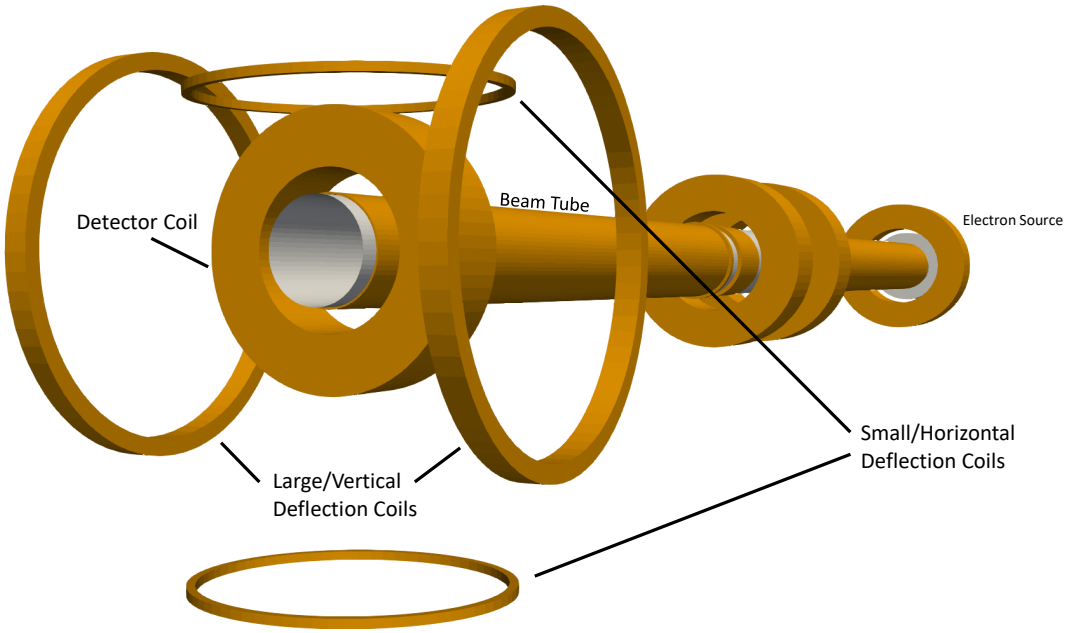

Figure 6.3: Simulation geometry of the aTEF test setup focused on the detector section (compare figure 6.1). Four deflection coils located around the detector are used to manipulate the magnetic field so that electrons are guided towards the detector. The coils are grouped into pairs: Two large (vertical) and two small (horizontal) deflection coils.

has been done via comparison of simulation results with dedicated measurement data and will be presented in the following chapter.

Table 6.1: Parameters of the deflection coils.

Coil Group	Parameter	Value
Large Deflection Coils	Inner radius	0.190 m
	Outer radius	0.208 m
	Length	0.026 m
	Total windings	252
	Max. current	±5 A
Small Deflection Coils	Inner radius	0.153 m
	Outer radius	0.162 m
	Length	0.009 m
	Total windings	35.7
	Max. current	±13 A

6.2 Comparison of measured fieldmaps with simulated data as probe for simulation accuracy

The key idea towards verifying the simulation accuracy is the comparison of measurements with corresponding simulations. If electrons are experimentally detected for different configurations with constant detector position, the corresponding simulated particle tracks should terminate at roughly the same position in the detector plane as well.
The final position of electrons arriving at the detector is strongly dependent on the phase of the cyclotron motion. This becomes apparent when looking at the cyclotron radius in the detector plane for a typical setting: Assuming a pitch angle of 30° with a kinetic energy of 14 keV the cyclotron radius at the detector with $B_{\mathrm{det}} = 25\,\mathrm{mT}$ would amount to $r_c \approx 8\,\mathrm{mm}$ (compare equation (3.6)). This size is of the same order as the side length of the microstructured part of the aTEF prototypes so that comparison of simulation with measurement data is only feasible if the magnetic field which primarily affects the electron's phase is modeled correctly. Therefore, before simulations were performed, not only the precise representation of the geometry in the simulation was verified as discussed in section 4.2.3 but also the power supplies used to power the coils of the setup were checked. A total of six power supplies of the type SM 15-200 D and SM 30-100 D by Delta Elektronika[2] were used. The first number in the name indicates the maximum voltage (in V) while the second number gives information about the maximum current (in A). Both types also feature a voltage and current readout with different sensitivities (SM 15-200 D: 0.01 V and 1 A; SM 30-100 D: 0.1 V and 0.1 A). A calibration cross-check of the current output of all power supplies was performed using a Fluke 8846 A precision multimeter[3]. Furthermore, as the two middle and chamber coils were connected in a parallel circuit to their respective power supply, the resistance of these coils was measured to be able to calculate the individual current through each coil. The respective resistances used for the simulation of these coils can be found in appendix A.3.

To check the positional consistency of the simulations, field scans were performed by systematically varying the currents at the deflection coils and measuring the corresponding electron count rate on the detector. The corresponding experimental work was performed by K. Gauda and S. Schneidewind and will be covered in their respective doctoral theses. Therefore, this section only covers the most important experimental details. Field scans for measurements with the 32 keV electron source at plate angles $\alpha = 0°$ and $\alpha = 8°$ are depicted on the left side in figure 6.5. The source was set to a backplate voltage of $U_{\mathrm{back}} = -17\,\mathrm{kV}$ with the frontplate being set to $U_{\mathrm{front}} = U_{\mathrm{back}} \cdot 0.57 = -9690\,\mathrm{V}$. For each setting, the count

[2]Delta Elektronika B.V., Vissersdijk 4, 4301 ND Zierikzee, Netherlands
[3]Fluke Corporation, 6920 Seaway Blvd, Everett, WA 98203

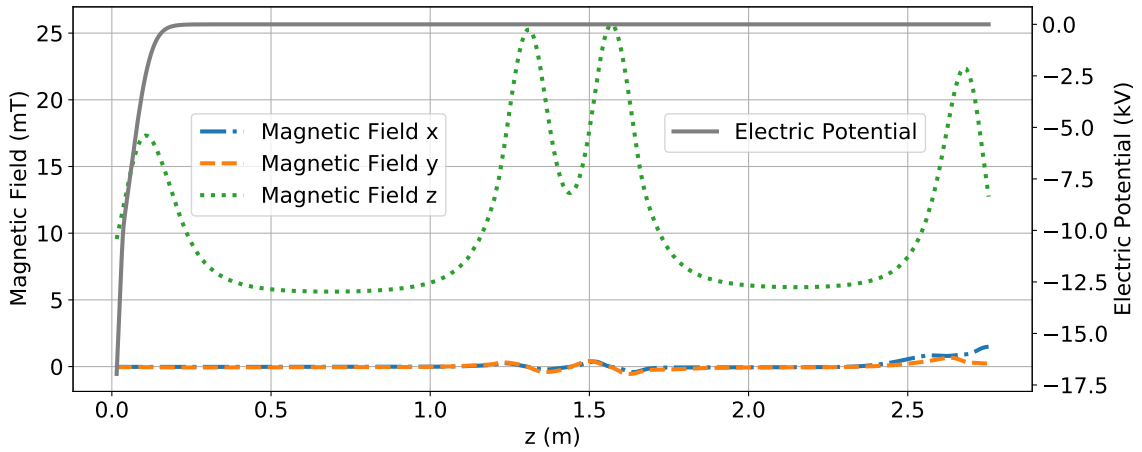

Figure 6.4: Simulated electromagnetic field configuration of the configuration used for the field scans with the 32 keV electron source (see figure 6.5). The electric potential (solid gray line) and the magnetic field components in x (dash-dot, blue), y (dashed, orange) and z-direction (dotted, green) that an electron with photoelectron source settings $\alpha = 0°$, $U_{\text{back}} = -17\,\text{kV}$ and deflection coil setting 7 A (horizontal) and 1.95 A (vertical) experiences are shown.

rate was measured in dependency on the current of the horizontal and vertical deflection coils. Iteration over the parameter space consisting of the two currents could be performed automatically. The electron source was operated with a pulsed light source at 1 kHz which could be used to suppress background arising from e.g. electrical noise. For this, the detector was operated in a gated mode, so that the light pulses act as trigger gates for the signal detection. The electromagnetic field configuration in this setting is depicted in figure 6.4. As $B_{\text{src}} = 17\,\text{mT}$ is only slightly smaller than $B_{\text{det}} = 22\,\text{mT}$, adiabatic enlargement of the pitch angle is not expected. Furthermore, the detector is located 3 cm outside of the center of the detector coil (in z-direction). This is a result of the the inner radius of the detector coil being too small to move it over the detector chamber flange. Therefore, the magnetic field drops below 15 mT in the detector plane, which effectively reduces the pitch angle at the detector. In fact, the simulation output shows that $\theta < 2.5°$ for $\alpha = 0°$ and $\theta < 5.7°$ for $\alpha = 8°$.
Vertical coil currents $I_{\text{v}} > 0\,\text{A}$ indicate a rightwards shift of the beam towards larger x-values while horizontal coil currents $I_{\text{h}} > 0\,\text{A}$ indicate an upwards shift towards larger y-values. This can also be seen in figure 6.4, where $I_{\text{v}} = 1.95\,\text{A}$ and $I_{\text{h}} = 7\,\text{A}$. Towards the detector section at $z \sim 2.7\,\text{m}$ both, the magnetic field component in x-direction as well as in y-direction take on values $> 0\,\text{mT}$.
All field scans show a distinct count rate maximum indicating that the electron beam hits the detector with the particular deflection coil settings. The impact of the varied plate angle can be seen as a change of the position of the count rate maximum in the deflection coil parameter

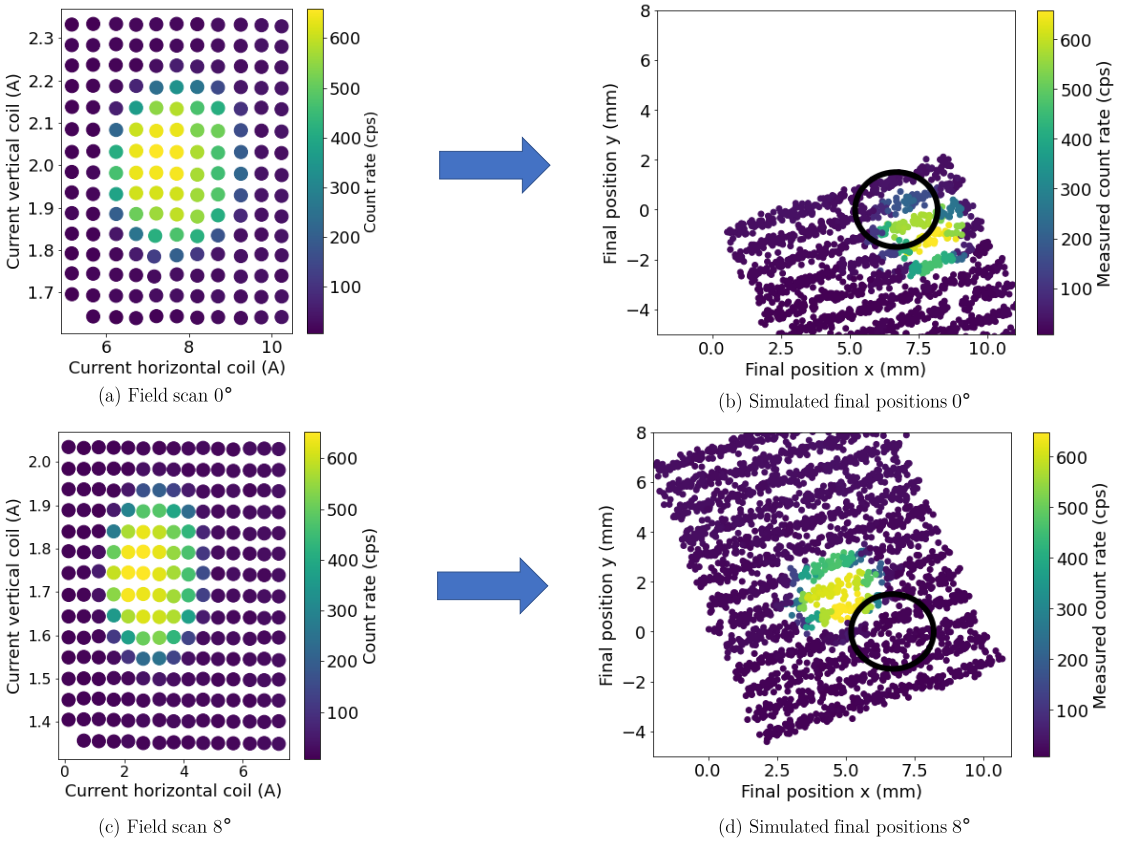

(a) Field scan 0°

(b) Simulated final positions 0°

(c) Field scan 8°

(d) Simulated final positions 8°

Figure 6.5: Measured field scans using the 32 keV source with plate angles $\alpha = 0°$ (a), 8° (c) and kinetic energy of 17 keV in combination with the corresponding simulated final electron positions in the detector plane (b, d). The measured field scans illustrate the count rate dependency of the deflection coil setting. The count rate maximum indicates that the detector is hit by the electron beam. The position of the maximum in this 2D-plane shifts when using a different plate angle. The information of the count rate of each setting is carried over to the plot showing the simulated final position of the electrons. The black circle indicates the measured physical position of the detector. Its center is located at $x = 6.7$ mm and $y = 0$ mm. The circular aperture with radius 1.5 mm from figure 6.2 was used.

space. The size of the beamspots does not vary significantly between measurements.

To be able to draw conclusions about the simulation accuracy, these field scans are now translated into the simulation coordinate system. In more detail, for each deflection coil setting of the field scan, ten Monte-Carlo generated electrons are simulated from the backplate of the electron source to the detector plane. Their final position in the detector plane is then recorded in a plot which can be seen on the right side in figure 6.5. The small number of electrons increases clarity but still allows to draw conclusions about the positional consistency of the simulations. The single aperture with radius 1.5 mm as seen in figure 6.2 was used here. Its position inside the vacuum chamber was measured and is depicted in these plots via a black circle to give a reference to the measurements. Its center is located at $x = 6.7$ mm

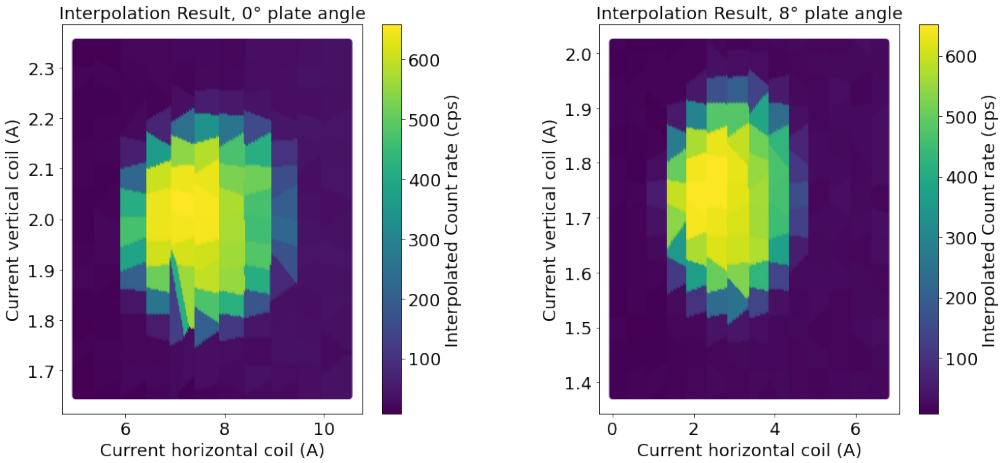

(a) (b)

Figure 6.6: Interpolation of the measured field scans with $\alpha = 0°$ (a) and $\alpha = 8°$ (b) (see figure 6.5) which is used to obtain the respective colormap of the simulated final position plots. The calculation is based on the `RBFInterpolator` function from the scipy package.

and $y = 0\,\text{mm}$. As each electron is associated with a particular setting that is connected to a measured count rate (see corresponding plot on the left side), each electron carries about the same color as the corresponding measurement setting. However, the deflection coil settings do not generally match the simulation settings. Therefore, the appropriate count rate for the particular simulation setting is inferred from two-dimensional interpolation with the values from each measurement as basis. For this, the `RBFInterpolator` function from the scipy package [Vir+20] is used which calculates the interpolation based on radial basis functions (RBF):

In general, a function $\varphi : [0, \infty) \to \mathbb{R}$ is called radial, when its evaluation at a given point $\vec{r}$ yields $\varphi(\vec{r}) = \varphi(\|r\|)$. A function $s(\vec{x})$ can now be approximated for a given set of data $(x_i, f_i$ with $i = 1, 2, ..., N)$ where $s(x_i) = f_i$. The function can be approximated via a linear combination of N radial functions forming a basis:

$$s(\vec{x}) = \sum_{i=1}^{N} \lambda_i \varphi(\|\vec{x} - \vec{x_i}\|). \tag{6.2}$$

Solving this equation yields the parameters λ_i so that s can be evaluated at any point x. For the fieldmaps a linear radial basis function of the type $\varphi(r) = r$ is used. Calculation is only performed using the nearest data point.

This technique in particular is beneficial for this use case as the input data in the two-dimensional deflection coil space is not perfectly structured due to the data being obtained from a direct measurement of the current. The interpolation result using the measurement

data from figure 6.5 is depicted in figure 6.6. In both figures rectangular plateaus at the positions of the data points are revealed. Their dimensions correspond to the step size between deflection coil settings. On these plateaus the function value is roughly constant so that at the edges a distinct step can be seen. This is an effect of the small number of nearest data points used for the calculation and is ideal for this case as this does not create an artificial bias. The step-like interpolation gives a very close resemblance of the simulation to the data, since discrete current steps were also used in the measurement. More specifically, if each data point from the respective measurement is seen as a pixel with a certain value, the interpolation effectively enlarges the pixel without adding an unnecessary interpretation of the underlying structure. A higher number of nearest data points for the calculation would induce artifacts or other unwanted behavior into the interpolation.
In figure 6.6(a), only a small distortion at the lower left corner of the count rate maximum is visible. This is probably due to the data points not being evenly spaced. However, as the maximum itself can easily be distinguished, this is going to have only a minor effect when comparing field scans to evaluate the simulation accuracy.

Looking at the basic structure of the simulated final positions in figure 6.5, one can spot multiple rows of particle endpoints. The spacing between them indicates the step size of the horizontal deflection coil setting. In the simulations the horizontal coil current was varied between $-2\,\mathrm{A}$ and $10\,\mathrm{A}$ in $1\,\mathrm{A}$ steps. In x-direction no distinct spacing is visible. The vertical coil current, which is responsible for the translation of the electron beam in x-direction, was varied between $1.2\,\mathrm{A}$ and $2.4\,\mathrm{A}$ in $0.05\,\mathrm{A}$ steps. However, one can see that each row is inclined towards the x-axis. Variation of the vertical coil current therefore does not only shift the beam in x-direction but also in y-direction. The same feature can be spotted for variation of the horizontal coil current. Increasing this current shifts the beam in positive y-direction and negative x-direction.
Due to the absence of track endpoints between rows which are separated by about $1\,\mathrm{mm}$ it can be concluded that the beamspot within each deflection coil setting is small compared to the size of the aperture with radius $1.5\,\mathrm{mm}$. Hence, the count rate maximum can easily be identified and its shape and size matches the properties of the aperture. This is also a reason why the count rate for areas apart from the maximum with count rates up to around $600\,\mathrm{cps}$ show a significant drop below $50\,\mathrm{cps}$. Further, the maximum does not change its value significantly between measurements.
Both simulation results show a small deviation from the measured detector position. For $\alpha = 0°$, the count rate maximum is shifted towards the lower right with the center being located at around $x = 7.6\,\mathrm{mm}$ and $y = -1\,\mathrm{mm}$ while at $\alpha = 8°$ the maximum can be found

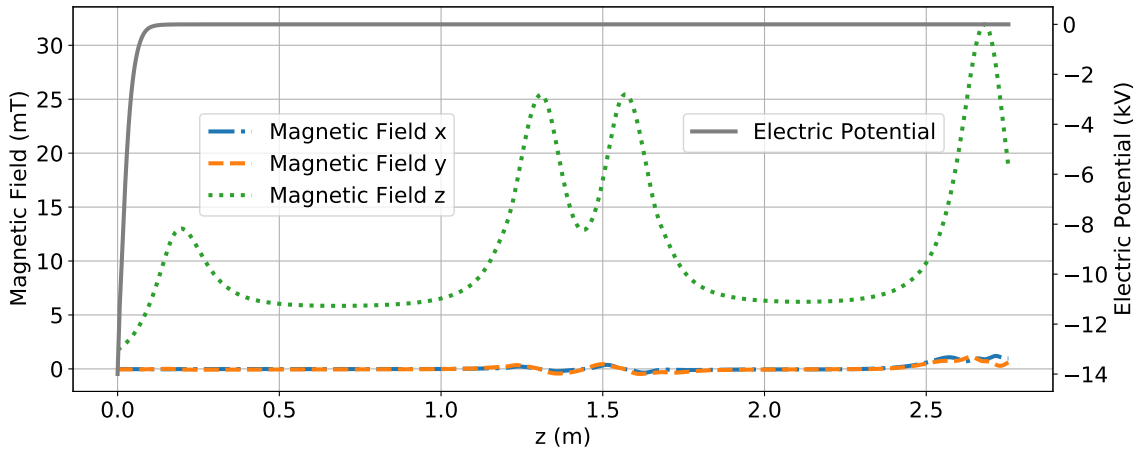

Figure 6.7: Simulated electromagnetic field of the configuration used for the field scans with the 18 keV electron source (see figure 6.8). The electric potential (solid gray line) and the magnetic field components in x (dash-dot, blue), y (dashed, orange) and z-direction (dotted, green) that an electron with $\alpha = 0°$, $U_{\text{back}} = -14\,\text{kV}$ and deflection coil setting 12 A (horizontal) and 1.9 A (vertical) experiences are shown.

at $x = 5\,\text{mm}$ and $y = +1\,\text{mm}$. Hence, a shift of 3 mm between simulations is observed.

Overall, the results show that the described method to verify the simulation accuracy can be applied and conclusions towards the applicability of simulations can be drawn. In this case, simulations of the field scans with $\alpha = 0°$ and $8°$ show good agreement between each other in terms of shape and size of the count rate maximum in the detector plane. Between the two simulations a discrepancy of the final electron positions of around 3 mm was found. Further, these spots are both within a distance of 2 mm to the measured detector position. The observed offset is on the same order as the cyclotron radius for an electron with $\theta = 5°$ and $E = 17\,\text{keV}$ which amounts to about 3 mm.
However, it should be noted that it was later found that the plate angles of the 32 keV electron source were not reproducible due to a hardware failure which affected the tilting mechanism of the source. The plate angle that was set during the measurements presented above is therefore not properly defined and should be seen with an enlarged error margin. The measurements presented in the following therefore use the 18 keV source.

For the development of the aTEF, comparison of measured count rates for electron angles in a range between 0° and 51° (magnetic cutoff angle at KATRIN) is aimed at. Therefore, field scans were repeated for a modified magnetic field configuration which allows larger pitch angles at the detector. The magnetic field configuration for these field scans can be seen in

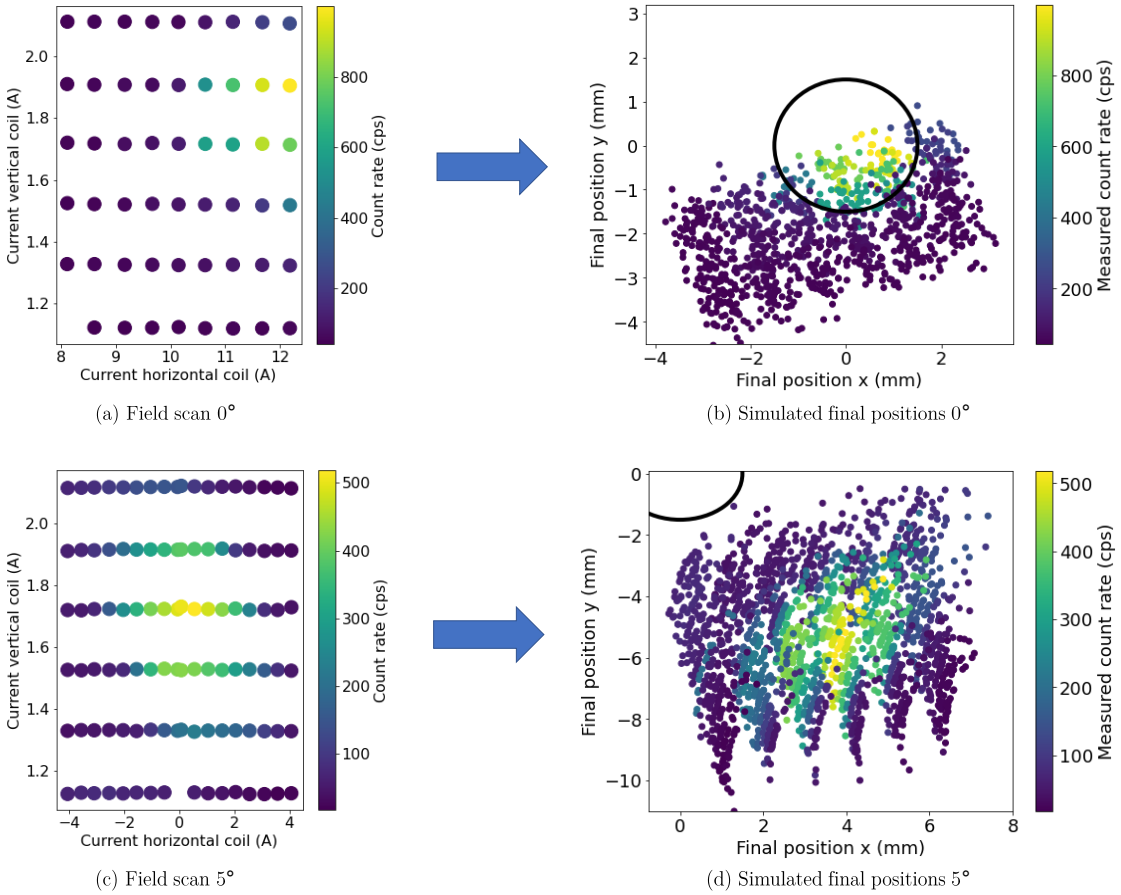

(a) Field scan 0°

(b) Simulated final positions 0°

(c) Field scan 5°

(d) Simulated final positions 5°

Figure 6.8: Measured field scans using the 18 keV source with plate angles $\alpha = 0°$ (a), 5° (c) and kinetic energy of 14 keV in combination with the corresponding simulated final electron positions in the detector plane (b, d). The black circle indicates the measured position of the detector. This graphic is analogous to figure 6.4.

figure 6.7. Most notably, the ratio $B_{\text{det}}/B_{\text{src}} = 31\,\text{mT}/13\,\text{mT}$ was modified to generate larger pitch angles at the detector. A drop of the magnetic field towards the detector plane can again be observed, however the remaining field of 19 mT is now larger than B_{src}. Furthermore, the source coil has been moved by 4 cm in z-direction, which results in a further increase of the pitch angle. The source was set to a backplate voltage of $U_{\text{back}} = -14\,\text{kV}$ with the frontplate being set to $U_{\text{front}} = U_{\text{back}} \cdot 0.75 = -10500\,\text{V}$.

Field scans that were measured in this magnetic field configuration with plate angles $\alpha = 0°$ and 5° are shown in figure 6.8. Here, 20 electrons are simulated per setting. Simulated pitch angles in the detector plane do not exceed 8° at $\alpha = 0°$ and 20° at $\alpha = 5°$. In the simulations the vertical coil current was varied between 1.12 A and 2.1 A in 0.2 A steps while the horizontal coil current was iterated from 8 A to 12 A in 0.5 A steps with plate angle 0° and from −4 A to 4 A in 0.5 A steps with plate angle 5°.

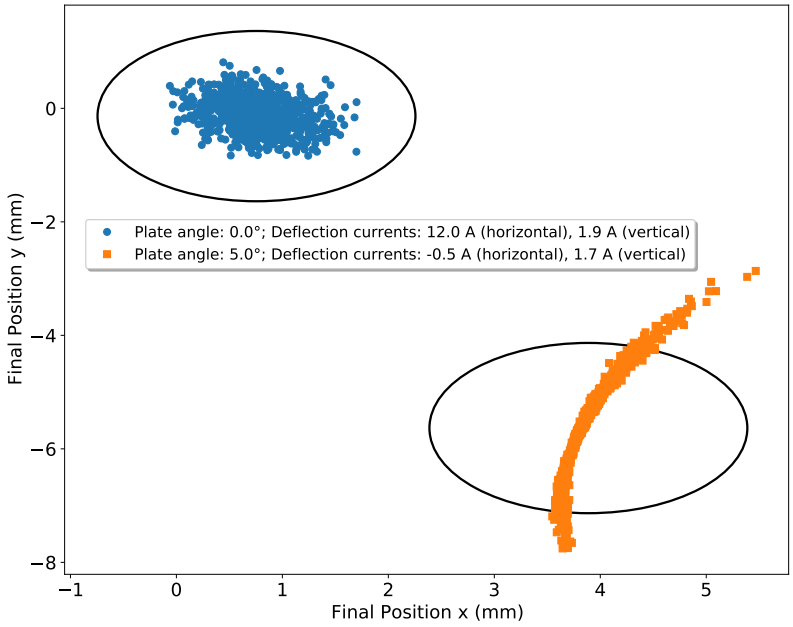

Figure 6.9: Simulated final track positions of electrons for plate angles $\alpha = 0°$ (blue) and 5° (orange) and one particular deflection coil setting which yielded the maximum count rate in figure 6.8. A total of 1000 electrons were simulated in each setting. The black circle indicates the size of the aperture in front of the detector ($r = 1.5\,\text{mm}$). Its position is chosen here so that its center equals the arithmetic medium value of the corresponding track endpoints.

Focusing on the 0° plate angle field scan, one finds that the maximum could not be covered entirely as the current limit of the horizontal coil was reached. This is largely due to the influence of the earth magnetic field. Its component in negative y-direction of $B_y = -45 \times 10^{-3}\,\text{mT}$ bends the magnetic field lines slightly downwards. Yet, a maximum count rate of 999 cps could be observed.

The corresponding simulated final positions indicate a good agreement with the measured detector position. Track endpoints of settings with large count rate lie within this area. Furthermore, the plot shows that only about half of the detector region is covered which is in accordance with the observation that not the whole count rate maximum could be covered by the field scan measurement.

In contrast, the measured field scan with plate angle 5° could obtain the whole beamspot. Indicated by the different colorbar, the scan shows a reduced maximal count rate of 518 cps which yields a reduction of 48% compared to the 0° setting.

Looking at the simulated final positions one finds an offset of the count rate maximum to the detector position by more than 5 mm to the lower right.

Distinct spaces where no track endpoints are located as it was the case in figure 6.4 cannot be seen. Instead, endpoints from different settings overlap, indicating an increased beamsize

in each setting. Further investigations on the beamsize are depicted in figure 6.9. This plot shows the final track positions of two particular settings from figure 6.8 with a total of 1000 Monte-Carlo generated electrons. The chosen settings exhibited the largest count rate for $\alpha = 0°$ and 5°, respectively. As a reference, the size of the aperture is again indicated via a black circle which is positioned at the arithmetic medium value of the corresponding track endpoints. For $\alpha = 0°$, track endpoints form a patch where all electrons are terminated within the aperture's radius. At $\alpha = 5°$, this patch is transformed into an elliptic structure which exceeds the boundaries of the aperture. The shape is in accordance with the cyclotron radius of 7 mm. Hence, it is likely that the shape and size originate from phase differences between single electron tracks with slightly different start parameters such as energy, angle and position at the backplate. The resulting angular and energy spread causes slight variations of the cyclotron radius between the emitted electrons. As the increased current at the detector in comparison to the settings used with the 32 keV source directly increases the cyclotron frequency, electrons travel a longer distance, causing these phase differences to build up. Therefore, this effect is only relevant when reviewing larger pitch angles. This however, is not ideal for investigations of aTEF prototypes. For this, one generally wants to look at the detector efficiency, in other words the measured count rate in dependence of the pitch angle. Beamsizes exceeding the size of the detection area therefore complicate the analysis.

Although the results demonstrate a mismatch between measurement and simulation at large pitch angles, the impact of the deflection coils on the pitch angle can in principal be investigated. For this, the mean final angle corresponding to each deflection coil setting used for the field scans shown before, are presented in figure 6.10. Instead of the final electron position, the focus now lies on the electron's angle relative to the magnetic field vector as well as to the z-axis.

Initially, the impact of the deflection coils on the pitch angle, which is depicted in figure 6.10(a) and (c) will be discussed. First of all, the angular range has to be noted. For $\alpha = 0°$, pitch angles from 6.8° to 7.8° are observed while the field scan with $\alpha = 5°$ results in pitch angles between 18.0° and 18.9°. Both plots show smaller fluctuations between single points. However, these lie within the statistical uncertainty of about $\pm 0.5°$. Especially in figure 6.10(a), higher pitch angles are generally connected to larger deflection coil currents which is in accordance with adiabaticity predictions. Assuming a magnetic field of $B = 19\,\mathrm{mT}$ and a magnetic moment of $\mu = 1.8 \times 10^{-15}\,\mathrm{Am}^2$ (corresponding to 7.1° at 14 keV), then a field increase by 2 mT due to the contribution of the deflection coils (compare figure 6.7) results in a pitch angle increase of 0.4°. This is not completely represented in the plot below with $\alpha = 5°$. Initial expectations would result in a symmetry axis at $I_\mathrm{h} = 0\,\mathrm{A}$. However,

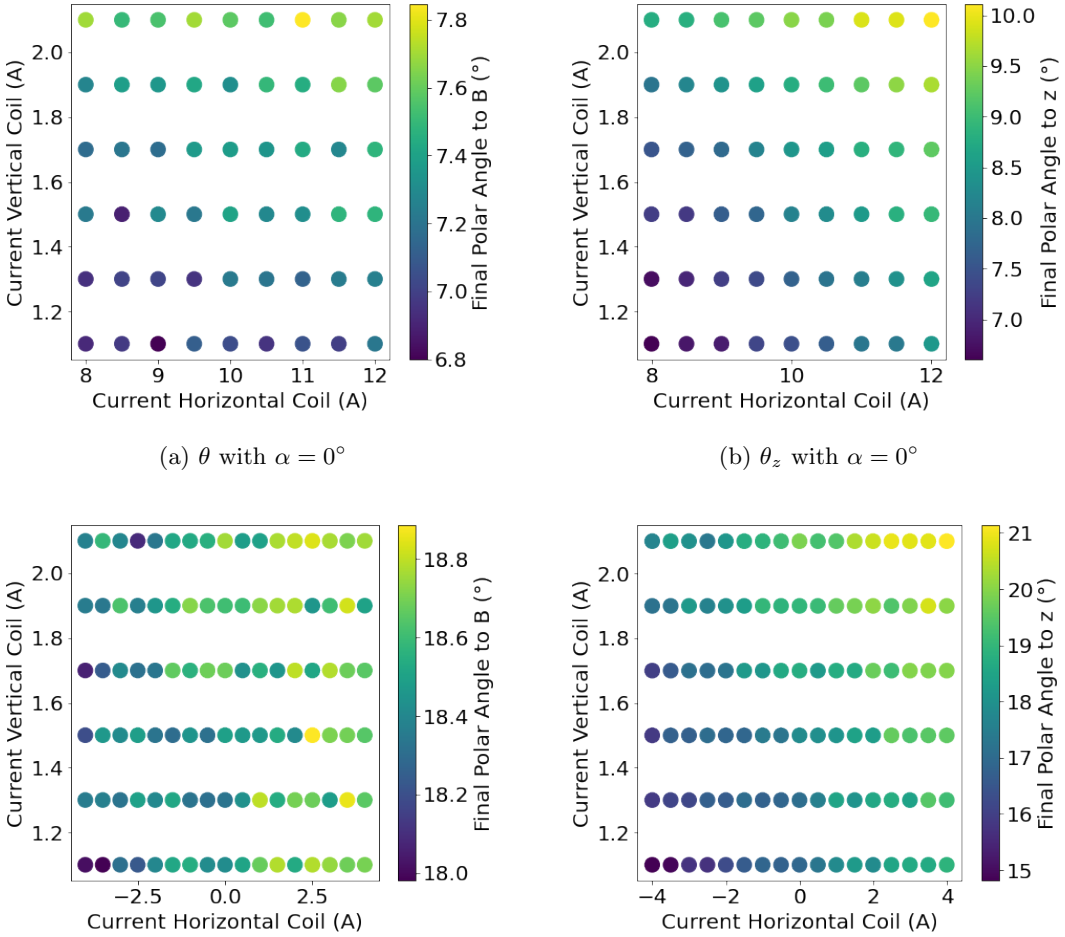

(a) θ with $\alpha = 0°$

(b) θ_z with $\alpha = 0°$

(c) θ with $\alpha = 5°$

(d) θ_z with $\alpha = 5°$

Figure 6.10: Angular distribution as a function of the deflection coil setting using the simulation results from figure 6.8. The angle is given relative to the magnetic field (a,c) and to the z-axis (b,d) for plate angles 0° (a,b) and 5° (c,d).

the distribution presents larger angles towards positive I_h. The reason for this is likely the position of the electron beam and the asymmetric geometric setup of the horizontal coils (compare figure 6.3). As the beam is shifted further downwards for negative I_h, not only the total magnetic field contribution by the horizontal coil pair is reduced. The beam also moves further out of the magnetic flux of the vertical coil pair, which in turn reduces the contribution of the vertical coil pair.

In contrast to the previously discussed angles relative to the magnetic field, figure 6.10(b) and (d) show the angles θ_z towards the z-axis. This relation is interesting when viewed in the context of the aTEF as in the setup, the detector is mounted with the channel axis parallel to the z-axis. The direct observable is therefore not the pitch angle but θ_z. It is immediately visible that the plots differ from the corresponding colormaps on the left, indicating

the significant influence of the deflection coils on the magnetic field lines. The difference between pitch angle θ and angle to the z-axis directly yields the angle of the magnetic field lines relative to the z-axis

$$\delta_z = \theta_z - \theta. \tag{6.3}$$

However, as these angles are invariant when rotating around either axis, one cannot directly infer the direction to which the field lines are bent. In these two exemplary situations, δ_z amounts to up to 2° for $\alpha = 0°$ and 5°, as well as -0.2° for $\alpha = 0°$ and -3° for $\alpha = 5°$. Furthermore, the distribution is skewed. An increase of θ_z can be found towards positive I_h and larger I_v, which can be observed by the maxima in the top right corners.
The presented results showcase the influence of the deflection coils on the electron angle. Each setting affects both θ and θ_z. Due to the spatial variance of the magnetic field which does not follow symmetry arguments, the behavior depending on the setting cannot be easily calculated. Moreover, there are multiple coils involved with different orientations so that the problem is highly non-trivial. In total, this demonstrates the importance of precise electron tracking simulations for the analysis of measurement results.

In conclusion, when using small pitch angles below 8°, the field scans show good agreement between simulation and measurement. However, larger pitch angles reveal an offset of final electron positions in simulations. The constant detector position in the (x,y)-plane is not represented. Further results suggest that the observable is directly influenced by the deflection coils. Moreover, since the magnetic field has a spatial dependence and the observable directly depends on the magnetic field strength, the electron angle from simulations entails an unknown uncertainty. Therefore, in the following, further simulations are performed to investigate possible sources for the discrepancy of the field scans and how the electron angle is affected.

6.3 Adiabaticity violation and its impact on electron angles

In [Sal19] the impact of adiabaticity violation in the setup was first discovered and discussed. As this effect has a direct influence on the pitch angle and therefore on several other parameters such as the cyclotron radius, adiabaticity was the main focus of the following investigation.
For this, it is important to recall the adiabaticity condition (see equation (3.8))

$$\left| \frac{1}{B} \frac{\mathrm{d}B}{\mathrm{d}t} \right| \ll \frac{\omega_c}{2\pi}, \tag{6.4}$$

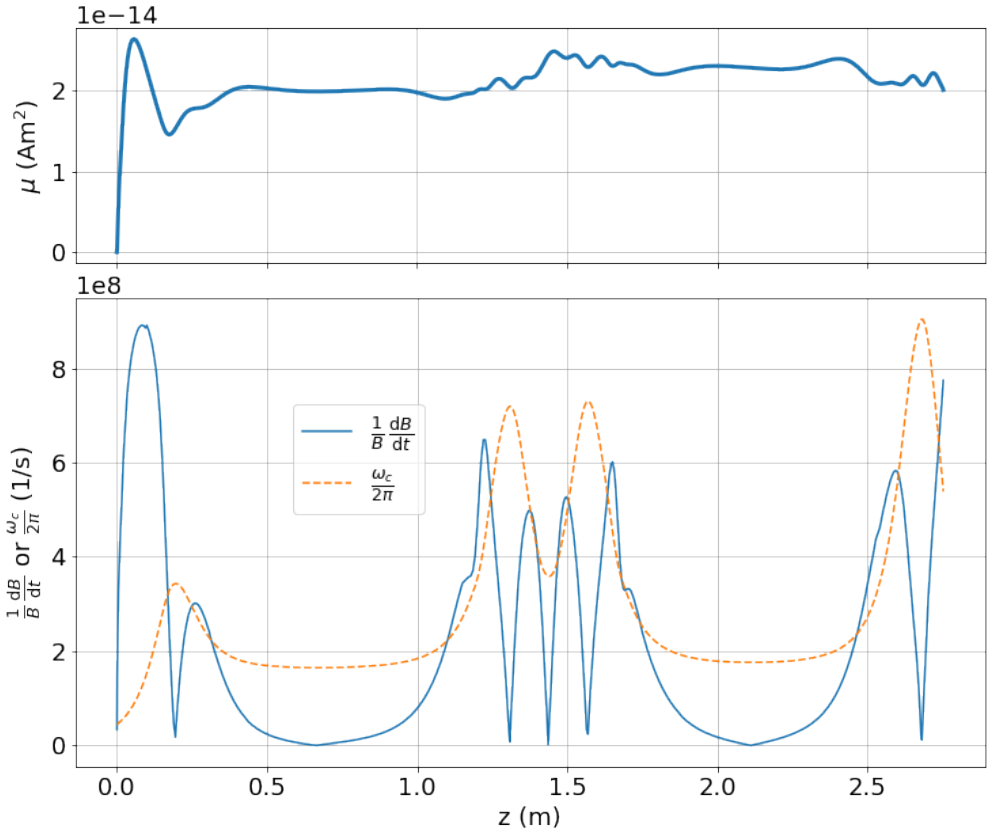

Figure 6.11: Adiabaticity condition of the setup visualized (bottom) showing the absolute value of the change of the magnetic field (blue) in comparison to the cyclotron frequency (orange) and evolution of orbital magnetic moment μ for one electron track with $\alpha = 8°$ (top). The depicted setting is the same as in figure 6.8 with no contribution of the deflection coils.

which is depicted in the bottom plot of figure 6.11. Three sections can be identified, where this condition is not fulfilled: At the start of the setup, in the middle and at the detector. These sections are all governed by the larger anoxal® coils creating a large but local magnetic field, meaning that a fast increase and drop of the magnetic field before and after these coils can be seen. Propagation inside the beam tubes can generally be assumed to be adiabatic. Furthermore, as the acceleration process is expected to be non-adiabatic, the focus will lie on the influence of the adiabaticity violation in the middle and at the end of the setup.

The top plot in figure 6.11 shows the evolution of the adiabatic invariant for one exemplary electron track. The orbital magnetic moment μ, defined in equation (3.10), ought to be constant after the acceleration process. However, in this configuration, a step of the magnetic moment between the first beamtube ($z = 0.5\,\mathrm{m}$ to $1\,\mathrm{m}$) and the second beamtube ($z = 1.9\,\mathrm{m}$

to 2.4 m) as well as at the detector towards $z > 2.55\,\mathrm{m}$ is visible. This directly corresponds to the area where the adiabaticity condition is not satisfied.
One can therefore calculate the change of the magnetic moment

$$\Delta\mu_{ij} = \mu_i - \mu_j \tag{6.5}$$

between different sections i and j of the setup. Here, $i, j \in \{1, 2, 3\}$ where 1 represents the first beamtube, 2 the second beamtube and 3 the detector area. Knowing the magnetic field B_{det} at the detector one can further calculate the impact that this step has on the measured angle θ

$$\mu = \frac{E_\perp}{B} = \frac{E \cdot \sin^2\theta}{B} \tag{6.6}$$

$$\Rightarrow \Delta\theta_{ij} = \theta_i - \theta_j = \arcsin\left(\sqrt{\frac{\mu_i \cdot B_{\mathrm{det}}}{E}}\right) - \arcsin\left(\sqrt{\frac{\mu_j \cdot B_{\mathrm{det}}}{E}}\right). \tag{6.7}$$

Further investigations now aim to investigate how the violation evolves depending on the setup configuration. For this, a magnetic field configuration comparable to figure 6.7 was set as a base setting. In this setting, the source coil is set to $I_{\mathrm{S}} = 4\,\mathrm{A}$, the chamber coils to a total of $I_{\mathrm{C}} = 20\,\mathrm{A}$, the middle coils to a total of $I_{\mathrm{M}} = 19\,\mathrm{A}$ and the detector coil to $I_{\mathrm{D}} = 13\,\mathrm{A}$. From this, the behavior of the adiabaticity violation was investigated as a function of the source coil and middle coil current via simulation. For comparison, this was performed with two different positions of the source coil at $z = 14\,\mathrm{cm}$ and 10 cm. Each iteration includes simulation of 1000 Monte-Carlo generated electrons with a kinetic energy of $E = 14\,\mathrm{keV}$. A plate angle of $\alpha = 8°$ was set.

The results are depicted in figure 6.12. Here, the step of the adiabatic moment is transformed to the change of the pitch angle at the detector according to equation (6.7). As there are two steps of the magnetic moment (between first and second beamtube and towards the detector), both $\Delta\theta_{21}$ (light color) as well as $\Delta\theta_{31}$ (dark color) are included.
In all cases, the data shows an oscillating behavior with the curves of the two coil positions revealing a phase shift between each other. Amplitude and phase length, however, show no significant differences. Due to $\Delta\theta_{31}$ including both steps of the magnetic moment, the corresponding curves show more deviations from a true sinusoidal behavior than the ones only including $\Delta\theta_{21}$. This is especially apparent in the lower plot where the current of the two middle coils is varied.

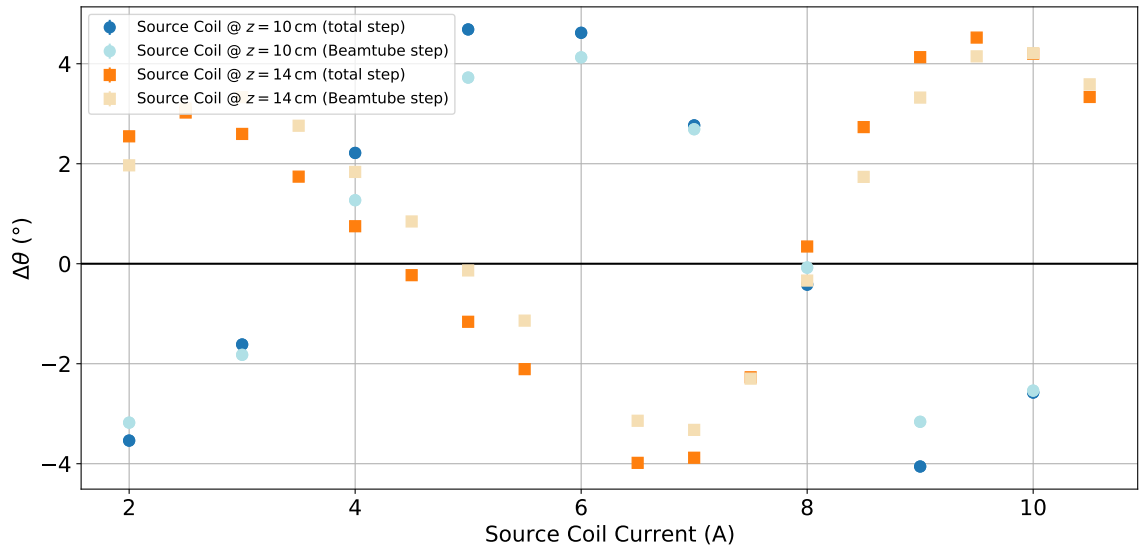

(a)

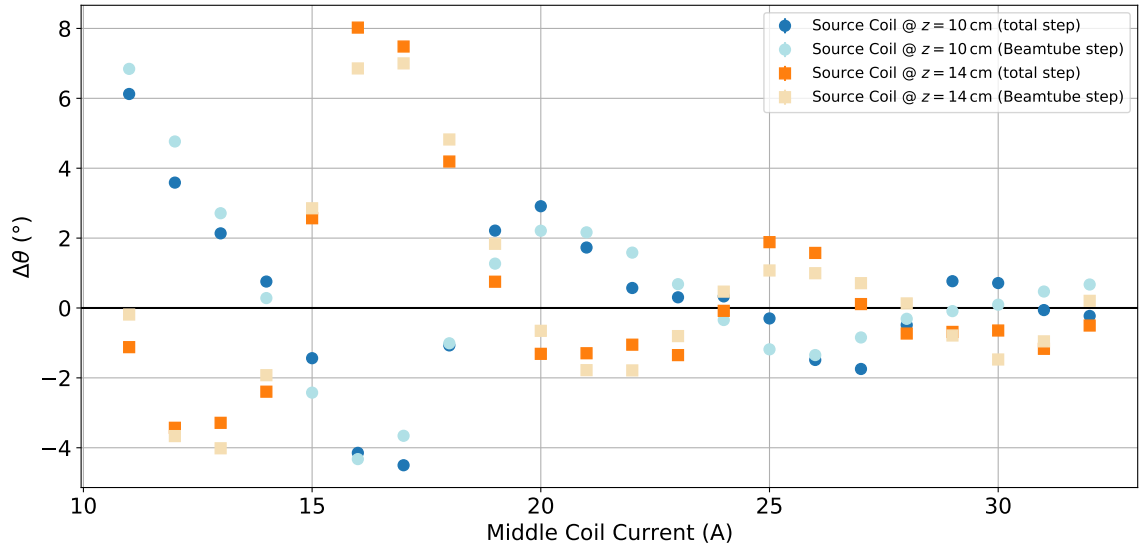

(b)

Figure 6.12: Impact of adiabaticity violation on the pitch angle at the detector depending on the source (a) and middle coil current (b). Two different configurations where the position of the source coil was varied between $z = 10\,\text{cm}$ (blue circles) and $z = 14\,\text{cm}$ (orange squares) are shown. The lightly colored points only include the step between first and second beamtube whereas the full color points also include the step of the magnetic moment at the detector. The observed oscillatory behavior indicates a phase dependency of the adiabaticity violation. Error bars, indicating the standard deviation from the arithmetic mean, are included. However their size is smaller than the markersize.

For the variation of the source magnetic field, $\Delta\theta$ can take on values up to around $+5°$ and $-4°$. The amplitude shows no significant change inside the simulated range. In contrast to this, an increase of the middle coil current slowly decreases the amplitude. For currents up to 16 A amplitudes are as high as $-4°$ and $+8°$. A doubled current reduces the amplitudes to $\pm 1°$ indicating better adiabatic conditions.

The observed characteristics lead to the assumption that the magnitude and sign is correlated to the phase of the electrons. Especially the shift of the curves when changing the z-position of the source coil, which has no impact on the magnetic conditions in the middle of the setup where the adiabaticity violation is observed, is a clear indicator for this. Hence, in figure 6.13 $\Delta\mu_{21}$ is shown as a function of the mean azimuthal angle Φ to the x-axis in the middle of the setup. Each data point corresponds to a specific source coil current from figure 6.12(a). The azimuth angle here is a result of the modulo operation, therefore $\Phi < 360°$. If a simulation run includes values with $360° - \epsilon < \Phi < 360°$ and $0° < \Phi < 0° + \epsilon$, values that fulfill the former relation are subtracted by 360°. This explains, why data points can be slightly smaller than 0°.
Figure 6.13 reveals a strong correlation between adiabaticity violation and the electron's phase. The shape is comparable to an inverted oscillation, where $\Phi \leq 150°$ is connected to $\Delta\mu_{21} < 0$, while $\Delta\mu_{21} > 0$ for $\Phi > 150°$, and is the same for both coil positions. The pitch angle and, thus, also the cyclotron radius and therefore the absolute position of the electrons in the middle of the setup changes with different currents and coil positions. This is likely the reason, why the data points are not perfectly compatible with each other.
The presented non-adiabatic behavior has also been shown by [HHT69]. This numerical study is based on charged particles trapped in a linear multipole magnetic field. When traversing the mid-plane where the magnetic field is minimal, Hastie et al. also observed a rapid change of the magnetic moment up to third order (compare equation (3.11)). With the simple model of the multipole field, they were able to approximate an analytic expression for the change of the magnetic moment which depends on the kinetic energy, the pitch angle and the phase (azimuthal angle). The latter was described as a distorted cosine with maxima displaced from $\pi/2$ and $3\pi/2$ which originates from the use of local variables instead of the guiding center approximation. While the data in figure 6.13 does not clearly indicate a distortion, the cosine behavior is directly identifiable. The analytical approach further demonstrates the importance of precise knowledge of the magnetic field at any given point of the system. Combined with the fact that the phase does not provide exact information about the electron's position and the corresponding magnetic field vector, characteristics such as the observed asymmetric amplitude are not unexpected.

In conclusion, the phase-dependent non-adiabaticity of the setup along with the non-matching field scans complicate the interpretation of measurement results. Especially the latter indicate that the electron phase or the magnetic field properties differ from experimental conditions, so that the predictability of electron propagation is no longer given. As the information on the electron angle is essential for the analysis of aTEF spectra, optimization of the setup or its magnetic field configuration is required. Thus, in the following, analysis on possible setup optimizations is presented.

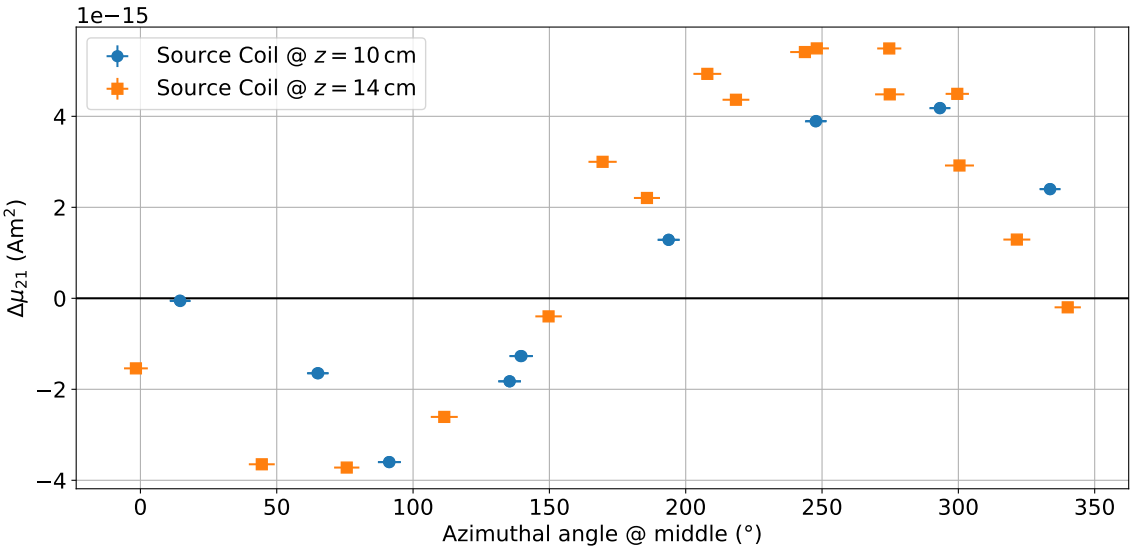

Figure 6.13: Adiabaticity violation $\Delta\mu_{21}$ as a function of the phase (azimuth angle) at the magnetic field minimum between the middle coils. To change the phase of the electrons, different source coil currents were applied. Two different configurations where the position of the source coil was varied between $z = 10\,\mathrm{cm}$ (blue circles) and $z = 14\,\mathrm{cm}$ (orange squares) are shown.

6.4 Discussion and next generation aTEF test setup

Although the magnetic adiabatic guiding of electrons in the setup seemed to allow for large pitch angles at the detector by enlarging the magnetic field ratio, the simulations revealed the non-predictable behavior for larger pitch angles. Therefore, this section is going to discuss several options to improve the setup for the aTEF development. This includes considerations that aim to improve the adiabaticity condition via an enhanced magnetic field, and other possibilities that change the setup's geometry.

One possible approach to counter the adiabaticity violation in the aTEF setup would be to

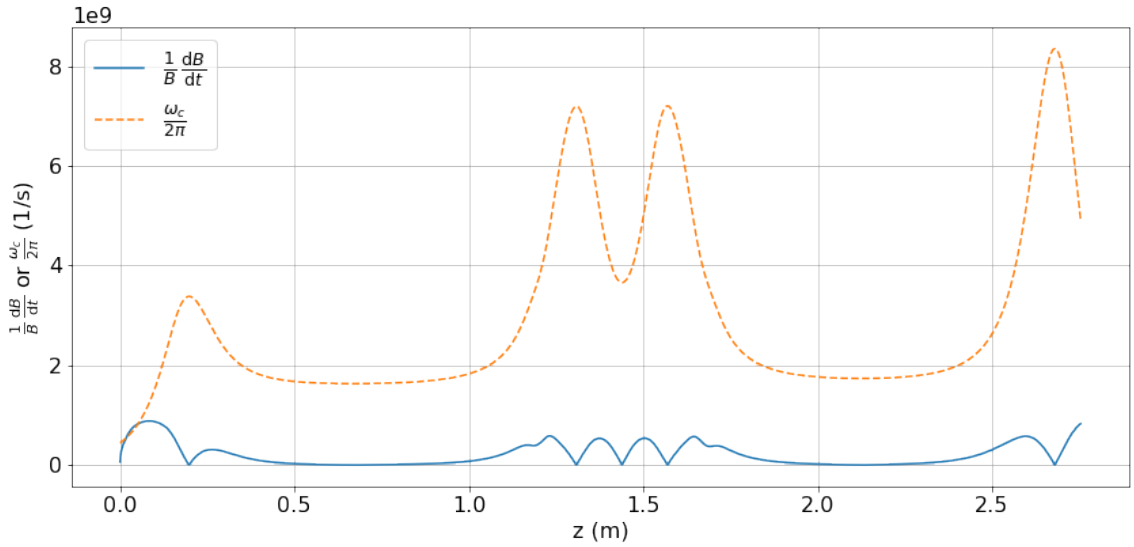

Figure 6.14: Adiabaticity condition for the aTEF test setup if 10 times higher currents would be applied to the magnetic coils. In more detail, this corresponds to 40 A entry coil, 200 A chamber coils, 190 A middle coils and 120 A detector coil.

apply a higher magnetic field strength. The adiabaticity condition (see equation (6.4)) for a hypothetical setting in which a ten times higher current is applied to the coils is depicted in figure 6.14. Since the cyclotron frequency is proportional to the magnetic field strength, this setting features a significant improvement regarding adiabaticity and leads to a near complete invariance of the magnetic moment. Furthermore, due to the high field strength, the cyclotron radius and therefore the beam spot could be reduced. Assuming a pitch angle of 40° using 14 keV electrons with a magnetic field of 200 mT the cyclotron radius would be 1.3 mm which is not only a significant reduction compared to the previously used settings but would also be smaller than the radius of the aperture (1.5 mm).
However, such a setting is experimentally not applicable, as the anoxal® coils, even with water-cooling, cannot sustain these high currents. Therefore, a different optimization strategy needs to be pursued.

Other strategies involve significant changes to the setup's geometry. As the main drawback of the current setup is the adiabaticity violation in the middle of the setup an apparent solution would be to reduce the size of the system. Therefore, a potential setup, which only includes the chamber of the electron source, the first beamtube and the detector, is depicted in figure 6.15(a). An exemplary magnetic field progression is shown below in figure 6.15(c). The two anoxal® coils from the second beamtube can be used in combination with the anoxal® coils of the first beamtube to create larger magnetic fields and better adiabatic conditions. In figure 6.16(a) it can be seen that with an improved detector position that lies inside the

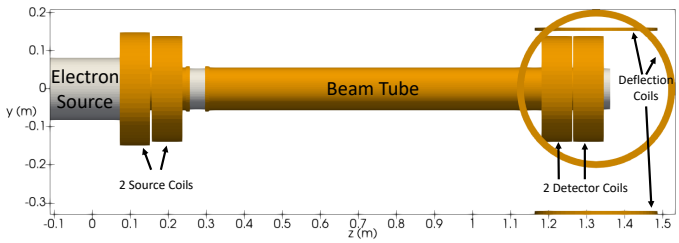

(a) Half-size setup

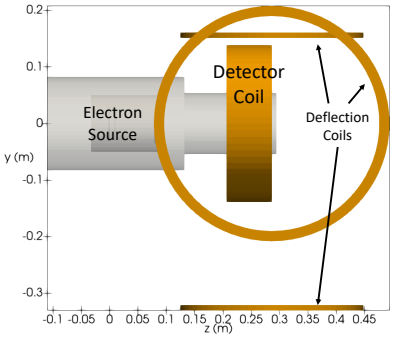

(b) Very short setup

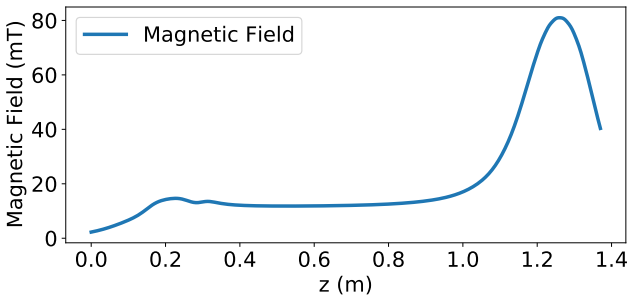

(c) Magnetic field of half-size setup

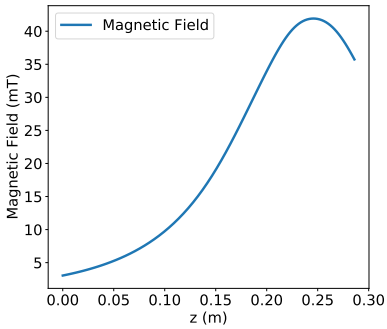

(d) Magnetic field of very short setup

Figure 6.15: Geometries and exemplary magnetic fields of considered setup optimizations. Cutting the setup in half (a, c) enables the possibility to reuse the anoxal® coils of the second beam tube so that two coils create the magnetic field at the source and the detector. This would enable higher magnetic fields but since these do not fit over the detector chamber flange, a drop of the magnetic field towards the detector is observed. Reducing the size of the setup even further (b, d) to a total length (from photocathode to detector) of 29 cm is also an option. Here, only one coil around the detector would be needed. In both simulations, a current of 20 A is applied to the detector coil/coils.

center of the magnetic field maximum of the detector coils, pitch angles up to 60° could in principle be generated. However, due to the magnetic field only reaching 40 mT around the detector one would again need to consider the size of the cyclotron radius. Assuming a pitch angle of 40° using 14 keV electrons with a magnetic field of 40 mT the cyclotron radius would be 6.4 mm. As the increased magnetic field (compared to the standard settings) and, thus, increased cyclotron frequency significantly enlarges the total path length of the electrons, phase differences develop again. This effect, which originates from the varying start conditions (such as direction and energy) was already discussed in section 6.2 and results in a large elliptic beamsize. This is indicated in figure 6.16(b), where electrons starting from the electron source with 8° plate angle create a beamspot that fills more than three quarters of a full ellipse. Although a reduction of the acceleration voltage would reduce this property due to

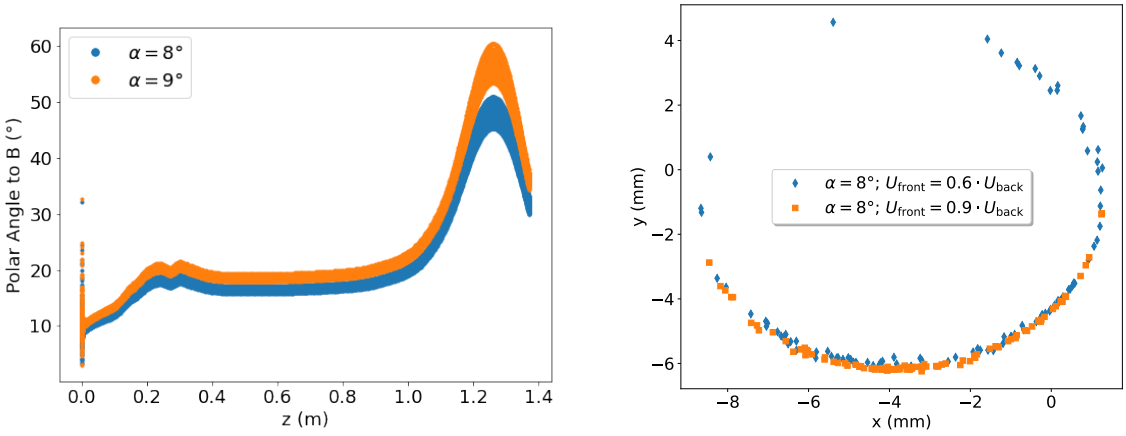

(a) (b)

Figure 6.16: Propagation of the pitch angle (a) through a hypothetical aTEF test setup with half the length and distribution of the final electron positions (b). Each setting is simulated using a total of 100 electrons. In (a) plate angles of 8° and 9° are considered, while in (b) a plate angle of 8° was set with varying frontplate voltages of 60% and 90% of the backplate voltage that was set to −14 kV. The maximum magnetic field inside the detector coil pair amounts to 81 mT and drops to 40 mT towards the detector plane.

the improved angular width, the beamsize would still exceed even the total size of the diode prototypes. Comparison of measured count rates would therefore still include uncertainties due to this.

To reduce the formation of phase differences and therefore large beamsizes, the total size of the setup could be reduced even further. As an example, a beam tube length of 15 cm is chosen, so that the detector is situated in a distance of roughly 29 cm from the backplate. The geometry of this setup, together with an exemplary magnetic field is depicted in figure 6.15(b) and (d). Due to the short length of this hypothetical setup, a coil positioned around the detector has a direct influence on the magnetic field at the source. Since, for adiabatic enlargement of the pitch angle, the ratio $B_{\mathrm{det}}/B_{\mathrm{src}}$ needs to be optimized, a single coil around the detector would be enough to create both B_{det} and B_{src}. Any further magnetic field at the source would yield a smaller ratio and therefore non-ideal test conditions.
However, not only does the detector coil now affect the magnetic field at the source but also the deflection coils do so. To investigate the impact of the deflection coils in this setup, a field scan was simulated again where a single anoxal® coil is positioned at the detector. The magnetic field of 42 mT inside the coil drops to about 3.5 mT at the backplate. The pitch angle as a function of the deflection coil setting is depicted in figure 6.17(a). This plot reveals, compared to the small angular range in figure 6.10, a significantly larger angular range

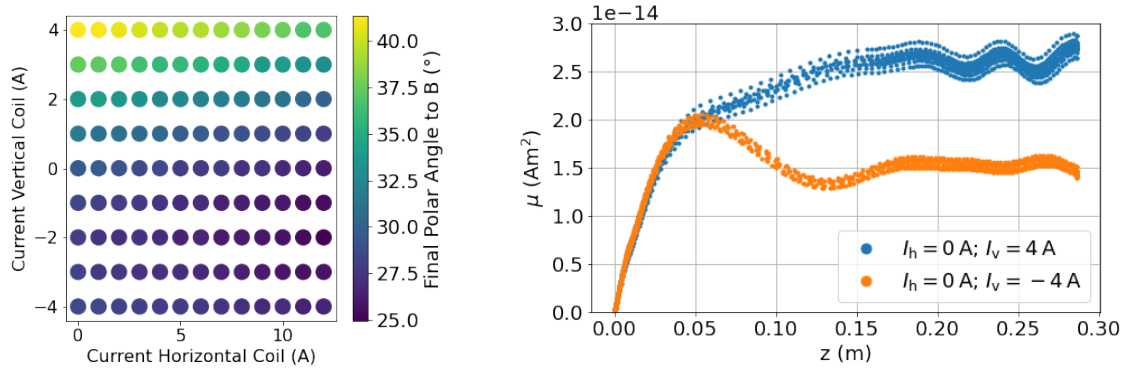

(a) (b)

Figure 6.17: Final pitch angles as a function of the deflection coil setting (a) and propagation of the magnetic moment μ in case of a hypothetical aTEF test setup with 29 cm length (b). A plate angle of $\alpha = 9°$ was set.

from 25° to as high as 41°. This hints towards an intervention of the magnetic field of the deflection coils in the evolution of the orbital magnetic moment μ. Hence, in figure 6.17(b) this property is plotted against the position for two different deflection coil settings which have the largest difference between each other. Until $z = 0.05\,\text{m}$ both settings present similar values for the magnetic moment. However, for $I_\text{h} = 0\,\text{A}$ and $I_\text{v} = 4\,\text{A}$ the magnetic moment continues to rise until $z = 0.15\,\text{m}$, while for $I_\text{h} = 0\,\text{A}$ and $I_\text{v} = -4\,\text{A}$ a maximum is reached at $z = 0.05\,\text{m}$. Its plateau starting behind $z = 0.15\,\text{m}$ is reduced by about 42% compared to the other setting. As no other parameters are changed between both simulations, the difference between the two curves is only caused by the change of the vertical deflection coil current. Due to the small magnetic field around the source, a perpendicular magnetic field component on the order of 1 mT is able to significantly alter the propagation of the electrons.
In that sense, one could in principle exploit this behavior to achieve higher pitch angles than initially expected under perfect adiabatic conditions. However, building this hypothetical setup with this effect in mind would include some risk, as this behavior has not been tested in measurements. A reliable setup that does not rely on the understanding of non-adiabatic effects is needed to avoid such difficulties.

All considerations lead to the following conclusion: The investigation of angular-sensitive detection principles such as the aTEF using adiabatic enlargement of the pitch angle results in several problems that find their origin in the cyclotron motion of the electrons. Namely, these are non-adiabatic electron propagation, cyclotron radii larger than the aperture size and concomitant with this large beamsizes. Therefore, all these considerations culminate in the final optimization of the setup. Instead of achieving angular selectivity via the pitch

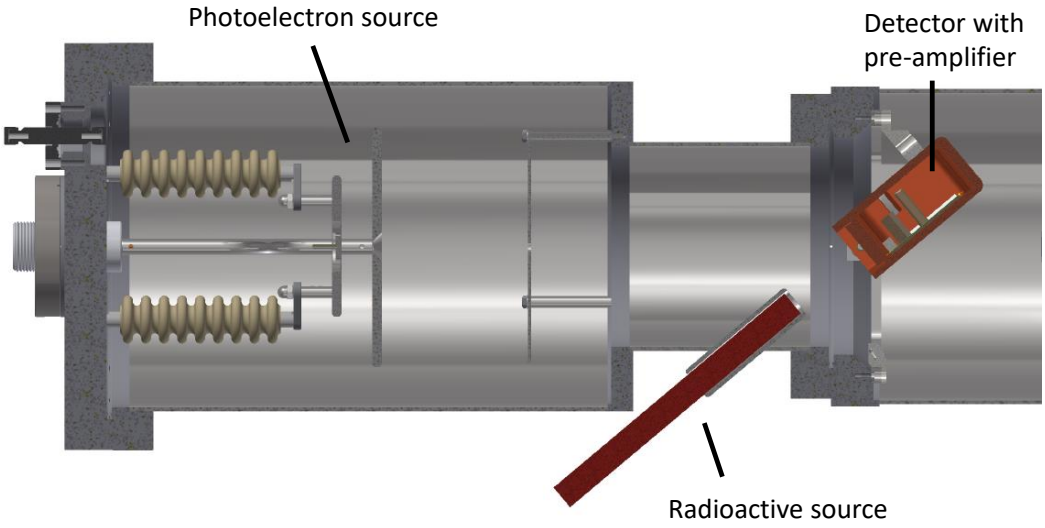

Figure 6.18: Proposed version for a new improved aTEF test setup. It features a fixed monoenergetic photoelectron source so that only electrons with minimal pitch angle are produced. The electrons propagate through a small beam tube towards the detector. The Si-aTEF prototypes including the preamplifier setup can be rotated around the detector surface by up to 60°. Furthermore, a radioactive source close to the detector can be used to perform calibration measurements. Image and design by H.-W. Ortjohann.

angle imprinted by non-adiabatic acceleration from the electron source, angular-selectivity is achieved via detector rotation. A CAD-drawing is depicted in figure 6.18. This new setup still features an angular-selective monoenergetic photoelectron source. However, it will only be operated with $\alpha = 0°$. These electrons are therefore emitted with a negligible angle towards the magnetic field, which now only serves the purpose to guide the electrons through a short beamtube towards the detector. The detector is mounted to a rotatable charge-sensitive preamplifier setup which can be precisely steered for each setting. The small pitch angle of the electrons results in a minimal cyclotron motion which has no impact on the beamsize. Furthermore, β- and γ-emitting sources can be used to calibrate the detection.
At the time of writing, the new setup is under construction. As it minimizes all uncertainties presented in the course of this chapter, it is well-suited for investigations of Si-aTEF prototypes.

7 Conclusion and outlook

The work presented in this thesis can be divided into two essential parts. On the one hand, particle tracking simulations were performed to analyze the measurement environment and the corresponding transmission properties for commissioning measurements of an upgraded monoenergetic and angular-selective electron source that can be operated at voltages up to −32 kV. On the other hand, simulations focusing on a test setup for the development of an active transverse energy filter could provide necessary information about systematic effects influencing the electron angle.

Particle tracking simulations were carried out using KATRIN's simulation framework Kassiopeia. To compute precise simulations, the advanced geometry of the 32 keV electron source was implemented and mesh optimizations enabled a high-accuracy electrostatic field computation. Since the simulation geometry of the source is modular, it can also easily be implemented in other simulations such as the KATRIN rear section or the aTEF test setup in Münster. The geometry of the monitor spectrometer was extended to include additional elements that were located near the electron source and, thus, had a strong influence on the shape of the electric field (elipot) or that were added for the commissioning measurements (e.g., dipole electrode). To attain faster computation times, the electrostatic field of the monitor spectrometer was divided into the source section and the spectrometer section. This ensured that the axial symmetry of the spectrometer could be used for faster calculation methods. The numerical accuracy of all simulations was optimized to provide energy conservation on a sub-meV level.

The commissioning measurements of the 32 keV electron source featured a special magnetic field configuration using an off-axis coil that was needed to hit the off-axis detector. However, this configuration has never been investigated before. The corresponding particle tracking simulations were able to characterize the impact of the off-axis configuration and are mostly in good agreement with measurement data. Therefore, the results could provide necessary evidence for the functionality of the electron source.
Most recently, the electron source has been successfully installed in the rear section of the

KATRIN experiment. First measurements provide evidence that the electron source is functional and can be used to investigate the energy loss function at energies above 21 keV, which was the limit of the previous electron source. This is going to ensure a further reduction of KATRIN's systematic uncertainty, bringing the experiment one step closer to the design goal.

Simulations regarding the aTEF test setup were computed to gain important information about the electron angle at the detector for the development of the aTEF. Therefore, the simulation geometry of the aTEF test setup was updated to match the measurement environment and the simulation accuracy was checked utilizing the deflection coils. Comparison of measurement data with the simulations revealed a discrepancy, which is likely caused by phase dependent adiabaticity violations. Furthermore, due to large cyclotron radii at the required kinetic energies, beamspots generally exceed the size of the detector. Hence, optimizations of the setup were discussed. It was found that magnetic adiabatic enlargement of electron angles in weak magnetic fields is not a viable approach to investigate the Si-aTEF prototypes with the needed precision.
Therefore, a new setup is in development, which achieves angular selectivity via detector rotation, thus omitting systematic effects such as adiabaticity or enlarged cyclotron radii. Providing an excellent environment to investigate prototypes at different electron impact angles, the new design is going to accelerate the development of the aTEF. If the current background model is correct, a functional aTEF would be able to significantly reduce the background of KATRIN by up to an order of magnitude. However, not being limited to KATRIN, any application that requires angular selective detection techniques in a large magnetic field could make use of the aTEF concept and optimize it for its needs.

A Appendix

A.1 Upgraded photoelectron source XML configuration

In the following, the XML-configuration that is used for Kassiopeia simulations of the 32 keV electron source is presented. The general backplate geometry, defined in lines 40-71, was implemented by S. Schneidewind. The mesh of the backplate, the frontplate defined in lines 74-129, the drift cage defined in lines 145-147, as well as the definition of the tree-structure in lines 150-181 were part of this work. In the code, several mesh-counts and mesh-powers have non-integer values. Up to kasper commit `f0e0f64b86b643a1af2eb632e0ab9d20f6222163` from December 2021, these values were rounded down. For newer kasper versions, non-integer values are no longer accepted and the non-integer values cause an error message.

```
1  <!-- XML geometry for the 32 keV rearsection EGun -->
2  <!-- shape parameters for the EGun geometry -->
3
4  <define name="rs_egun_plate_deburring_r" value="{15.e-4}"/>
5  <define name="rs_egun_plate_deburring_r2" value="{5.e-4}"/>
6  <define name="rs_egun_plate_inner_t" value="{5.24e-4}"/>
7  <define name="rs_egun_plate_distance" value="{2.0e-2}"/>
8  <define name="rs_egun_backplate_z" value="{0.0e-2}"/>
9  <define name="rs_egun_backplate_t" value="{[rs_egun_plate_inner_t]+2*[
       rs_egun_plate_deburring_r]}"/>
10 <define name="rs_egun_backplate_r" value="{3.0e-2}"/>
11 <define name="rs_egun_beamspot_r" value="{100.e-6}"/>
12 <define name="rs_egun_frontplate_z" value="{1.0e-3}"/>
13 <define name="rs_egun_frontplate_t" value="{[rs_egun_plate_inner_t]+2*[
       rs_egun_plate_deburring_r2]}"/>
14 <define name="rs_egun_frontplate_r" value="{5.0e-2}"/>
15 <define name="rs_egun_frontplate_hole_r" value="{7.5e-3}"/>
16 <define name="lx_slit" value="{1.7e-2}"/>
17 <define name="lx_slit_round" value="{2.5e-2}"/>
18 <define name="ly_slit" value="{8.02e-3}"/>
19 <define name="plate_thickness" value="{15.24e-4}"/>
20 <define name="rs_egun_opening_fine_r" value="{5.1e-4}"/>
```

```
<define name="rs_egun_opening_fine_z1" value="{7e-4}"/>
<define name="rs_egun_opening_fine_y1" value="{5e-4}"/>
<define name="rs_egun_opening_fine_z2" value="{11.8e-4}"/>
<define name="rs_egun_opening_fine_y2" value="{3.2e-4}"/>
<define name="rs_egun_opening_fine_r2" value="{5.35e-4}"/>
<define name="rs_egun_opening_fine_y3" value="{1.8e-4}"/>
<define name="rs_egun_driftcage_z" value="{-4.7e-2}"/>
<define name="rs_egun_driftcage_l" value="{9.5e-2}"/>
<define name="rs_egun_driftcage_r" value="{6.e-2}"/>
<geometry>
<!-- global meshing parameters for the EGun geometry -->
<define name="rs_egun_curvature_n" value="20"/>
<define name="rs_egun_opening_curvature_n" value="9"/>
<define name="rs_egun_arc_count" value="25"/>
<define name="rs_egun_mesh_scale" value="5"/>
<define name="rs_egun_mesh_power" value="1"/>

<!-- EGun backplate surface -->
<!-- reference point is front side of backplate-->
<tag name="electrode_tag" name="rs_egun_tag" name="all_tag" name="
    collision_tag">
    <tag name="rs_egun_backplate_system_tag" name="rs_egun_backplate_tag"
         name="back_voltage_tag">
        <rotated_poly_loop_surface name="rs_egun_backplate_surface"
            rotated_mesh_count="{2*[rs_egun_arc_count]}">
            <poly_loop>
                <start_point x="{[rs_egun_backplate_z]}" y="0."/>
                <next_line
                x="{[rs_egun_backplate_z]}"
                y="{[rs_egun_backplate_r]-[rs_egun_plate_deburring_r]}"
                line_mesh_count="{6*[rs_egun_mesh_scale]}"
                line_mesh_power="[rs_egun_mesh_power]"
                />
                <next_arc
                x="{[rs_egun_backplate_z]-[plate_thickness]}"
                y="{[rs_egun_backplate_r]}"
                radius="[rs_egun_plate_deburring_r]"
                right="true"
                short="false"
                arc_mesh_count="{[rs_egun_curvature_n]}"
                />
```

```
59                  <next_line
60                  x="{[rs_egun_backplate_z]-[rs_egun_plate_deburring_r]}"
61                  y="{0.0}"
62                  line_mesh_count="{0.4*[rs_egun_mesh_scale]}"
63                  line_mesh_power="{2/3*[rs_egun_mesh_power]}"
64                  />
65                  <last_line
66                  line_mesh_count="{0.4*[rs_egun_mesh_scale]}"
67                  line_mesh_power="{2/3*[rs_egun_mesh_power]}"
68                  />
69              </poly_loop>
70          </rotated_poly_loop_surface>
71      </tag> <!-- rs_egun_backplate_tag -->
72
73
74      <tag name="rs_egun_frontplate_tag" name="front_voltage_tag">
75
76          <shell_poly_line_surface name="rs_egun_frontplate_inner_side_1"
                angle_start="270" angle_stop="450" shell_mesh_count="{1.2*[
                rs_egun_arc_count]}" shell_mesh_power="[rs_egun_mesh_power]">
77              <poly_line>
78                  <start_point x="{-[plate_thickness]/2}" y="{[ly_slit]/2+[
                        rs_egun_opening_fine_y3]}"/>
79                  <next_line x="{-[plate_thickness]/2}" y="{[ly_slit]/2}"
                        line_mesh_count="{0.5*[rs_egun_mesh_scale]}"
                        line_mesh_power="[rs_egun_mesh_power]"/>
80                  <next_arc x="{-[plate_thickness]/2 + [
                        rs_egun_opening_fine_z1]}" y="{[ly_slit]/2 - [
                        rs_egun_opening_fine_y1]}" radius="{[
                        rs_egun_opening_fine_r]}" right="true" short="true"
                        arc_mesh_count="{[rs_egun_arc_count]}"/>
81                  <next_line x="{-[plate_thickness]/2 + [
                        rs_egun_opening_fine_z2]}" y="{[ly_slit]/2 - [
                        rs_egun_opening_fine_y2]}" line_mesh_count="{[
                        rs_egun_mesh_scale]}" line_mesh_power="[
                        rs_egun_mesh_power]"/>
82                  <next_arc x="{[plate_thickness]/2}" y="{[ly_slit]/2+[
                        rs_egun_opening_fine_y3]}" radius="{[
                        rs_egun_opening_fine_r2]}" right="true" short="true"
                        arc_mesh_count="{[rs_egun_arc_count]}"/>
83                  </poly_line>
```

```
84              </shell_poly_line_surface>
85              <shell_poly_line_surface name="
                    rs_egun_frontplate_inner_side_2" angle_start="270"
                    angle_stop="450" shell_mesh_count="{1.2*[
                    rs_egun_arc_count]}" shell_mesh_power="[
                    rs_egun_mesh_power]">
86              <poly_line>
87              <start_point x="{-[plate_thickness]/2}" y="{-[ly_slit
                    ]/2-[rs_egun_opening_fine_y3]}"/>
88              <next_line x="{-[plate_thickness]/2}" y="{-[ly_slit]/2}"
                    line_mesh_count="{0.5*[rs_egun_mesh_scale]}"
                    line_mesh_power="[rs_egun_mesh_power]"/>
89              <next_arc x="{-[plate_thickness]/2 + [
                    rs_egun_opening_fine_z1]}" y="{-[ly_slit]/2 + [
                    rs_egun_opening_fine_y1]}" radius="{[
                    rs_egun_opening_fine_r]}" right="false" short="true"
                    arc_mesh_count="{[rs_egun_arc_count]}"/>
90              <next_line x="{-[plate_thickness]/2 + [
                    rs_egun_opening_fine_z2]}" y="{-[ly_slit]/2 + [
                    rs_egun_opening_fine_y2]}" line_mesh_count="{[
                    rs_egun_mesh_scale]}" line_mesh_power="[
                    rs_egun_mesh_power]"/>
91              <next_arc x="{[plate_thickness]/2}" y="{-[ly_slit]/2 -[
                    rs_egun_opening_fine_y3]}" radius="{[
                    rs_egun_opening_fine_r2]}" right="false" short="true"
                    arc_mesh_count="{[rs_egun_arc_count]}"/>
92          </poly_line>
93      </shell_poly_line_surface>
94
95      <extruded_poly_line_surface name="rs_egun_frontplate_inner_side_3
            " zmin="{-[lx_slit]/2}" zmax="{[lx_slit]/2}"
            extruded_mesh_count="{[rs_egun_arc_count]}"
            extruded_mesh_power="[rs_egun_mesh_power]">
96          <poly_line>
97              <start_point x="{-[plate_thickness]/2}" y="{[ly_slit]/2+[
                    rs_egun_opening_fine_y3]}"/>
98              <next_line x="{-[plate_thickness]/2}" y="{[ly_slit]/2}"
                    line_mesh_count="{0.5*[rs_egun_mesh_scale]}"
                    line_mesh_power="[rs_egun_mesh_power]"/>
```

```
99                  <next_arc x="{-[plate_thickness]/2 + [
                        rs_egun_opening_fine_z1]}" y="{[ly_slit]/2 - [
                        rs_egun_opening_fine_y1]}" radius="{[
                        rs_egun_opening_fine_r]}" right="true" short="true"
                        arc_mesh_count="{[rs_egun_arc_count]}"/>
100                 <next_line x="{-[plate_thickness]/2 + [
                        rs_egun_opening_fine_z2]}" y="{[ly_slit]/2 - [
                        rs_egun_opening_fine_y2]}" line_mesh_count="{[
                        rs_egun_mesh_scale]}" line_mesh_power="[
                        rs_egun_mesh_power]"/>
101                 <next_arc x="{[plate_thickness]/2}" y="{[ly_slit]/2+[
                        rs_egun_opening_fine_y3]}" radius="{[
                        rs_egun_opening_fine_r2]}" right="true" short="true"
                        arc_mesh_count="{[rs_egun_arc_count]}"/>
102             </poly_line>
103         </extruded_poly_line_surface>
104
105         <extruded_poly_line_surface name="rs_egun_frontplate_inner_side_4
                " zmin="{-[lx_slit]/2}" zmax="{[lx_slit]/2}"
                extruded_mesh_count="{[rs_egun_arc_count]}"
                extruded_mesh_power="[rs_egun_mesh_power]">
106             <poly_line>
107                 <start_point x="{-[plate_thickness]/2}" y="{-[ly_slit
                        ]/2-[rs_egun_opening_fine_y3]}"/>
108                 <next_line x="{-[plate_thickness]/2}" y="{-[ly_slit]/2}"
                        line_mesh_count="{0.5*[rs_egun_mesh_scale]}"
                        line_mesh_power="[rs_egun_mesh_power]"/>
109                 <next_arc x="{-[plate_thickness]/2 + [
                        rs_egun_opening_fine_z1]}" y="{-[ly_slit]/2 + [
                        rs_egun_opening_fine_y1]}" radius="{[
                        rs_egun_opening_fine_r]}" right="false" short="true"
                        arc_mesh_count="{[rs_egun_arc_count]}"/>
110                 <next_line x="{-[plate_thickness]/2 + [
                        rs_egun_opening_fine_z2]}" y="{-[ly_slit]/2 + [
                        rs_egun_opening_fine_y2]}" line_mesh_count="{[
                        rs_egun_mesh_scale]}" line_mesh_power="[
                        rs_egun_mesh_power]"/>
111                 <next_arc x="{[plate_thickness]/2}" y="{-[ly_slit]/2 -[
                        rs_egun_opening_fine_y3]}" radius="{[
                        rs_egun_opening_fine_r2]}" right="false" short="true"
                        arc_mesh_count="{[rs_egun_arc_count]}"/>
```

```
112             </poly_line>
113         </extruded_poly_line_surface>
114
115     </tag>
116         <tag name="rs_egun_frontplate_base_tag">
117             <extruded_surface name="rs_egun_frontplate_base">
118                 <extruded_object z_min="{[rs_egun_plate_distance]}" z_max
                        ="{[rs_egun_plate_distance]+[plate_thickness]}"
                        longitudinal_mesh_count="60" longitudinal_mesh_power="
                        1." closed_form="1"  mesh_merge_distance="0">
119                     <inner_line x1="{-[lx_slit]/2}" y1="{[ly_slit]/2+[
                            rs_egun_opening_fine_y3]}" x2="{[lx_slit]/2}" y2="
                            {[ly_slit]/2+[rs_egun_opening_fine_y3]}"/>
120                     <inner_arc x1="{[lx_slit]/2}" y1="{[ly_slit]/2+[
                            rs_egun_opening_fine_y3]}" x2="{[lx_slit]/2}" y2="
                            {-[ly_slit]/2-[rs_egun_opening_fine_y3]}" radius="
                            {[ly_slit]/2+[rs_egun_opening_fine_y3]}"
                            positive_orientation="0"/>
121                     <inner_line x1="{[lx_slit]/2}" y1="{-[ly_slit]/2-[
                            rs_egun_opening_fine_y3]}" x2="{-[lx_slit]/2}" y2=
                            "{-[ly_slit]/2-[rs_egun_opening_fine_y3]}" />
122                     <inner_arc x1="{-[lx_slit]/2}" y1="{-[ly_slit]/2-[
                            rs_egun_opening_fine_y3]}" x2="{-[lx_slit]/2}" y2=
                            "{[ly_slit]/2+[rs_egun_opening_fine_y3]}" radius="
                            {[ly_slit]/2+[rs_egun_opening_fine_y3]}"
                            positive_orientation="0" />
123                     <outer_arc x1="[rs_egun_frontplate_r]" y1="0." x2="
                            {-[rs_egun_frontplate_r]}" y2="0" radius="[
                            rs_egun_frontplate_r]" positive_orientation="0"/>
124                     <outer_arc x1="{-[rs_egun_frontplate_r]}" y1="0" x2="
                            [rs_egun_frontplate_r]" y2="0" radius="[
                            rs_egun_frontplate_r]" positive_orientation="0"/>
125                 </extruded_object>
126             </extruded_surface>
127         </tag>
128     </tag>
129 </tag>
130
131 <tag name="rs_egun_backplate_system_tag" name="rs_egun_beamspot_tag" name
        ="beamspot_tag">
```

```
132     <rotated_line_segment_surface name="rs_egun_beamspot_surface"
            rotated_mesh_count="[rs_egun_arc_count]">
133         <line_segment
134         x1="{[rs_egun_backplate_z]}"
135         y1="{0.}"
136         x2="{[rs_egun_backplate_z]}"
137         y2="{[rs_egun_beamspot_r]}"
138         line_mesh_count="{0.3*[rs_egun_mesh_scale]}"
139         line_mesh_power="{1.}"
140         />
141     </rotated_line_segment_surface>
142 </tag> <!-- rs_egun_beamspot_tag -->
143
144
145 <tag name="front_voltage_tag" name="electrode_tag" name="collision_tag"
        name="driftcage_tag">
146     <cylinder_surface name="rs_egun_driftcage" z1="{[rs_egun_driftcage_z
            ]}" z2="{[rs_egun_driftcage_z]+[rs_egun_driftcage_l]}" r="[
            rs_egun_driftcage_r]" longitudinal_mesh_count="{2*[
            rs_egun_mesh_scale]}" longitudinal_mesh_power="[rs_egun_mesh_power
            ]" axial_mesh_count="{1.5*[rs_egun_arc_count]}"/>
147 </tag>
148
149
150 <space name="rs_egun_frontplate_assembly">
151     <surface name="rs_egun_frontplate_inner_side_1_assembled" node="
            rs_egun_frontplate_inner_side_1">
152         <transformation displacement="{[lx_slit]/2} 0. {[
                rs_egun_plate_distance]+[plate_thickness]/2}"/>
153     </surface>
154     <surface name="rs_egun_frontplate_inner_side_2_assembled" node="
            rs_egun_frontplate_inner_side_2">
155         <transformation displacement="{-[lx_slit]/2} 0. {[
                rs_egun_plate_distance]+[plate_thickness]/2}"/>
156     </surface>
157     <surface name="rs_egun_frontplate_inner_side_3_assembled" node="
            rs_egun_frontplate_inner_side_3">
158         <transformation displacement="0. 0. {[rs_egun_plate_distance]+[
                plate_thickness]/2}" rotation_euler="90. 90. 90."/>
159     </surface>
```

```
160     <surface name="rs_egun_frontplate_inner_side_4_assembled" node="
            rs_egun_frontplate_inner_side_4">
161         <transformation displacement="0. 0. {[rs_egun_plate_distance]+[
                plate_thickness]/2}" rotation_euler="90. 90. 90."/>
162     </surface>
163 
164     <surface name="rs_egun_frontplate_surface_assembled" node="
            rs_egun_frontplate_base"/>
165 
166 </space>
167 
168 <!-- rs_egun plate system assembly -->
169 <space name="rs_egun_plate_system_assembly">
170     <tag name="rs_egun_fiber_0_tag">
171         <surface name="rs_egun_fiber_0" node="rs_egun_beamspot_surface">
172             <transformation displacement="0. 0. 0."/>
173         </surface>
174     </tag>
175     <surface name="rs_egun_backplate" node="rs_egun_backplate_surface">
176         <transformation displacement="0. 0. 0."/>
177     </surface>
178     <space name="rs_egun_frontplate" tree="rs_egun_frontplate_assembly">
179         <transformation displacement="0. 0. 0."/>
180     </space>
181 </space>
182 
183 </geometry>
```

A.2 Electron absorption at the upgraded electron source in the monitor spectrometer environment

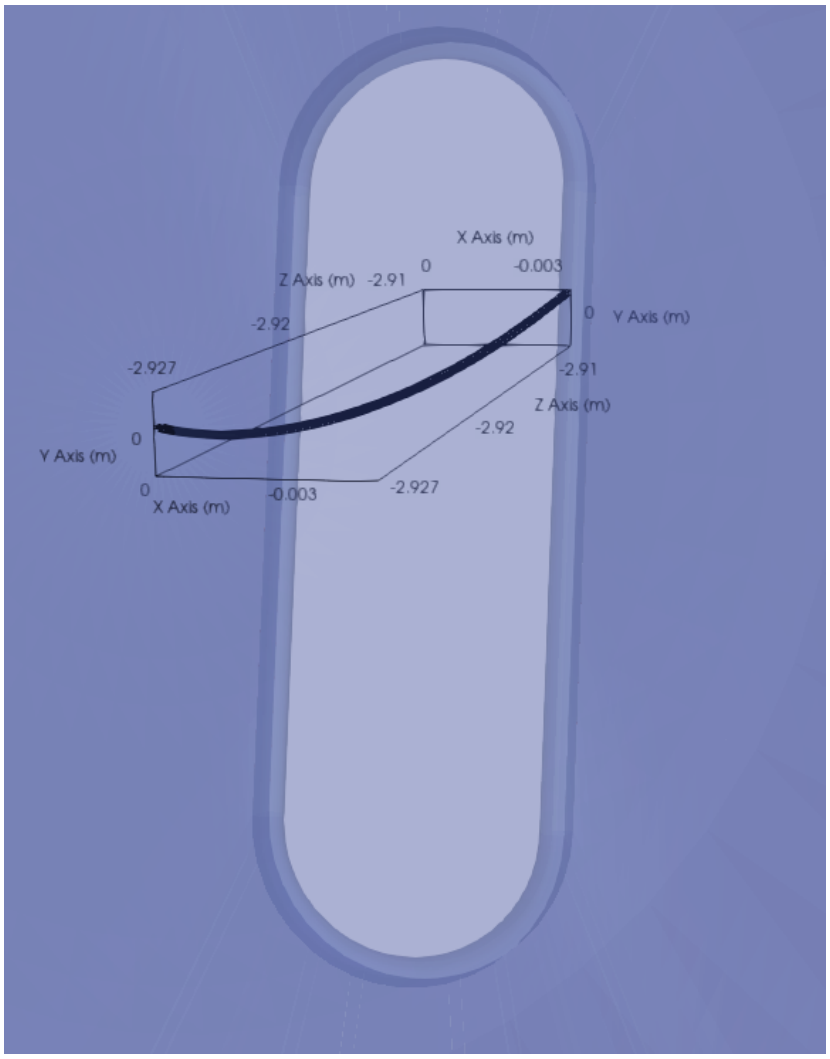

Figure A.1: Exemplary simulated electron tracks which hit the frontplate after emission from the photocathode. The point of view is located behind the backplate. The electron source settings are $U_{\mathrm{acc}} = 8\,\mathrm{kV}$ and $\alpha = -14°$. The source is installed vertically. The total magnetic field is 35 mT. Note the inverted x-axis in this picture.

The magnetic field vector used in the calculation in section 5.2.2 between front- and backplate is $\vec{B} = (-0.0006, -0.002, -0.034)\,\mathrm{T}$.
The corresponding electric field vector that was used, is $\vec{E} = (-1200, 95000, -385000)\,\mathrm{V/m}$. Both vectors are extracted from the simulation output. Corresponding tracks of electrons, which are emitted from the photocathode and terminated on the frontplate, are depicted in figure A.1.

A.3 Resistance of aTEF test setup coils

Most coils were connected in a series circuit, so that the set current could be directly translated towards the simulation configuration. However, the two chamber coils on each beam tube as well as the two anoxal® coils in the middle of the setup were connected in parallel to their respective power supply. As it cannot be assumed, that the resistance R_i of each coil i is the same, the resistance of each coil was measured independently with the readout of the particular power supply. From

$$I = I_1 + I_2 = U_1/R_1 + U_2/R_2 \tag{A.1}$$

where U_i and I_i are the measured voltages and currents it can be followed that the currents are split with the following ratio

$$\frac{I_2}{I} = \frac{1}{1 + \frac{R_2}{R_1}}. \tag{A.2}$$

The currents of each coil are then independently applied according to the experimentally set total current I in each simulation. The resulting resistances and corresponding current fractions are depicted in table A.1.

Table A.1: Values set for simulation of the magnetic field of the aTEF test setup obtained from resistance measurements of the middle and chamber coils. The numbers 1 and 2 indicate the position of the respective coil of the coil pair (1: located closer to the electron source, 2: located closer to the detector).

Coil pair	Resistance	I_2/I
Middle coils	$R_1 = 0.76\,\Omega$ $R_2 = 0.79\,\Omega$	0.49
Chamber coils	$R_1 = 1.23\,\Omega$ $R_2 = 1.18\,\Omega$	0.51

List of Figures

List of Tables

Bibliography

[Abd+09] JN Abdurashitov et al. "Measurement of the solar neutrino capture rate with gallium metal. III. Results for the 2002–2007 data-taking period". In: *Physical Review C* 80.1 (2009), p. 015807. DOI: 10.1103/PhysRevC.80.015807 (cit. on p. 5).

[Abg+21] N Abgrall et al. "LEGEND-1000 preconceptual design report". In: *arXiv preprint arXiv:2107.11462* (2021). DOI: 10.48550/arXiv.2107.11462 (cit. on p. 8).

[Agh+20] N Aghanim et al. "Planck 2018 results-I. Overview and the cosmological legacy of Planck". In: *Astronomy & Astrophysics* 641 (2020), A1. DOI: 10.1051/0004-6361/201833880 (cit. on p. 7).

[Ago+20] M Agostini et al. "Final results of GERDA on the search for neutrinoless double-β decay". In: *Physical Review Letters* 125.25 (2020), p. 252502. DOI: 10.1103/PhysRevLett.125.252502 (cit. on p. 8).

[Aha+13] B Aharmim et al. "Combined analysis of all three phases of solar neutrino data from the Sudbury Neutrino Observatory". In: *Physical Review C* 88.2 (2013), p. 025501. DOI: 10.1103/PhysRevC.88.025501 (cit. on p. 5).

[Ake+21a] M Aker et al. "Precision measurement of the electron energy-loss function in tritium and deuterium gas for the KATRIN experiment". In: *The European Physical Journal C* 81.7 (2021), pp. 1–16. DOI: 10.1140/epjc/s10052-021-09325-z (cit. on pp. 17, 18).

[Ake+21b] M Aker et al. "The design, construction, and commissioning of the KATRIN experiment". In: *Journal of Instrumentation* 16.08 (2021), T08015. DOI: 10.1088/1748-0221/16/08/T08015 (cit. on pp. 11, 12).

[Ams+15] JF Amsbaugh et al. "Focal-plane detector system for the KATRIN experiment". In: *Nuclear Instruments and Methods in Physics Research Section A: Accelerators, Spectrometers, Detectors and Associated Equipment* 778 (2015), pp. 40–60. DOI: 10.1016/j.nima.2014.12.116 (cit. on p. 12).

[Ang+05] J Angrik et al. *KATRIN design report*. Tech. rep. 51.54.01; LK 01. Forschungszentrum Jülich, 2005. DOI: 10.5445/IR/270060419 (cit. on pp. 1, 11).

[Ase+11] VN Aseev et al. “Upper limit on the electron antineutrino mass from the Troitsk experiment”. In: *Physical Review D* 84.11 (2011), p. 112003. DOI: 10.1103/PhysRevD.84.112003 (cit. on pp. 1, 9).

[Bab+12] M Babutzka et al. “Monitoring of the operating parameters of the KATRIN Windowless Gaseous Tritium Source”. In: *New Journal of Physics* 14.10 (2012), p. 103046. DOI: 10.1088/1367-2630/14/10/103046 (cit. on p. 11).

[Bas14] MS Basunia. “Nuclear data sheets for A= 210”. In: *Nuclear Data Sheets* 121 (2014), pp. 561–694. DOI: 10.1016/j.nds.2014.09.004 (cit. on p. 18).

[Beh+17] J Behrens et al. “A pulsed, mono-energetic and angular-selective UV photoelectron source for the commissioning of the KATRIN experiment”. In: *The European Physical Journal C* 77.6 (2017), pp. 1–20. DOI: 10.1140/epjc/s10052-017-4972-9 (cit. on pp. 13, 20, 22, 27).

[Beh17] J Behrens. “Design and commissioning of a monoenergetic photoelectron source and active background reduction by magnetic pulse at the KATRIN experiment”. PhD thesis. Institut für Kernphysik - Westfälische Wilhelms-Universität Münster, (2017) (cit. on pp. 26, 27, 30, 37).

[Cha14] J Chadwick. “Intensitätsverteilung im magnetischen Spectrum der β-Strahlen von Radium B + C”. In: *Verhandl. Dtsc. Phys. Ges.* 16 (1914), p. 383 (cit. on p. 3).

[Cle+98] BT Cleveland et al. “Measurement of the solar electron neutrino flux with the Homestake chlorine detector”. In: *The Astrophysical Journal* 496.1 (1998), p. 505. DOI: 10.1086/305343 (cit. on pp. 4, 5).

[Cor14] T Corona. “Methodology and application of high performance electrostatic field simulation in the KATRIN experiment”. PhD thesis. The University of North Carolina at Chapel Hill, (2014) (cit. on p. 25).

[Dan+62] G Danby et al. “Observation of high-energy neutrino reactions and the existence of two kinds of neutrinos”. In: *Physical Review Letters* 9.1 (1962), p. 36. DOI: 10.1103/PhysRevLett.9.36 (cit. on p. 4).

[De +02] MJ De Boer et al. “Guidelines for etching silicon MEMS structures using fluorine high-density plasmas at cryogenic temperatures”. In: *Journal of microelectromechanical systems* 11.4 (2002), pp. 385–401. DOI: 10.1109/JMEMS.2002.800928 (cit. on p. 23).

[Erh+14] M Erhard et al. “High-voltage monitoring with a solenoid retarding spectrometer at the KATRIN experiment”. In: *Journal of Instrumentation* 9.06 (2014), P06022. DOI: 10.1088/1748-0221/9/06/P06022 (cit. on p. 12).

[Fer+15] E Ferri et al. “The Status of the MARE Experiment with ^{187}Re and ^{163}Ho Isotopes”. In: *Physics Procedia* 61 (2015), pp. 227–231. DOI: 10.1016/j.phpro.2014.12.037 (cit. on p. 8).

[Fer34] E Fermi. “An attempt to a β rays theory”. In: *Il Nuovo Cimento* 1 (1934), p. 20 (cit. on p. 3).

[Frä+17] FM Fränkle et al. “Background processes in the KATRIN main spectrometer”. In: *Journal of Physics: Conference Series*. Vol. 888. 1. IOP Publishing. (2017), p. 012070. DOI: 10.1088/1742-6596/888/1/012070 (cit. on p. 17).

[Frä+22] FM Fränkle et al. “KATRIN background due to surface radioimpurities”. In: *Astroparticle Physics* 138 (2022), p. 102686. DOI: 10.1016/j.astropartphys.2022.102686 (cit. on pp. 2, 18).

[Ful+20] A Fulst et al. “Time-focusing time-of-flight, a new method to turn a MAC-E-filter into a quasi-differential spectrometer”. In: *The European Physical Journal C* 80.10 (2020), pp. 1–11. DOI: 10.1140/epjc/s10052-020-08484-9 (cit. on p. 49).

[Fur+17] D Furse et al. “Kassiopeia: a modern, extensible C++ particle tracking package”. In: *New Journal of Physics* 19.5 (2017), p. 053012. DOI: 10.1088/1367-2630/aa6950 (cit. on pp. 25, 26).

[Gal+00] M Galeazzi et al. “End-point energy and half-life of the ^{187}Re β-decay”. In: *Physical Review C* 63.1 (2000), p. 014302. DOI: https://doi.org/10.1103/PhysRevC.63.014302 (cit. on p. 8).

[Gan+11] A Gando et al. “Constraints on θ_{13} from a three-flavor oscillation analysis of reactor antineutrinos at KamLAND”. In: *Physical Review D* 83.5 (2011), p. 052002. DOI: 10.1103/PhysRevD.83.052002 (cit. on p. 6).

[Gas+17] L Gastaldo et al. “The electron capture in ^{163}Ho experiment – ECHo”. In: *The European Physical Journal Special Topics* 226.8 (2017), pp. 1623–1694. DOI: 10.1140/epjst/e2017-70071-y (cit. on p. 8).

[Gau+22] K Gauda et al. “An active transverse energy filter to differentiate low energy particles with large pitch angles in a strong magnetic field”. In: (Mar. 2022). arXiv: 2203.06085 [physics.ins-det] (cit. on pp. 19, 22–24).

[Geo] Helmholtz Centre Potsdam German Research Centre for Geosciences - GFZ. *IGRF Declination Calculator*. http://isdc.gfz-potsdam.de/igrf-declination-calculator/. Accessed: 2021-10-11 (cit. on p. 34).

[Gil+09] W Gil et al. “The cryogenic pumping section of the KATRIN experiment”. In: *IEEE transactions on applied superconductivity* 20.3 (2009), pp. 316–319. DOI: 10.1109/TASC.2009.2038581 (cit. on p. 12).

[Ham+99] W Hampel et al. “GALLEX solar neutrino observations: Results for GALLEX IV”. In: *Physics Letters B* 447.1-2 (1999), pp. 127–133. DOI: 10.1016/S0370-2693(98)01579-2 (cit. on p. 5).

[HH76] T Hsu and JL Hirshfield. “Electrostatic energy analyzer using a nonuniform axial magnetic field”. In: *Review of Scientific Instruments* 47.2 (1976), pp. 236–238. DOI: 10.1063/1.1134594 (cit. on p. 12).

[HHT69] RJ Hastie, GD Hobbs, and JB Taylor. “Non-adiabatic behaviour of particles in inhomogeneous magnetic fields”. In: *Plasma Physics and Controlled Nuclear Fusion Research. Proceedings of the Third International Conference on Plasma Physics and Controlled Nuclear Fusion Research. Vol. I.* (1969) (cit. on p. 67).

[Hil11] B Hillen. “Untersuchung von Methoden zur Unterdrückung des Spektrometeruntergrunds beim KATRIN-Experiment”. PhD thesis. Institut für Kernphysik - Westfälische Wilhelms-Universität Münster, (2011) (cit. on p. 36).

[HWS09] MD Henry, C Welch, and A Scherer. “Techniques of cryogenic reactive ion etching in silicon for fabrication of sensors”. In: *Journal of Vacuum Science & Technology A: Vacuum, Surfaces, and Films* 27.5 (2009), pp. 1211–1216. DOI: 10.1116/1.3196790 (cit. on p. 23).

[Jac99] JD Jackson. *Classical electrodynamics*. John Wiley & Sons, 1999, pp. 592–596. DOI: 10.1002/3527600434.eap109 (cit. on pp. 14, 41).

[Jan+09] HV Jansen et al. “Black silicon method X: a review on high speed and selective plasma etching of silicon with profile control: an in-depth comparison between Bosch and cryostat DRIE processes as a roadmap to next generation equipment”. In: *Journal of micromechanics and microengineering* 19.3 (2009), p. 033001. DOI: 10.1088/0960-1317/19/3/033001 (cit. on p. 23).

[Jöh13] R Jöhren. “Spectroscopy of the hyperfine transition in lithium-like bismuth at the ESR at GSI and an APD-based single-photon detector for laser spectroscopy on highly charged ions”. PhD thesis. Institut für Kernphysik - Westfälische Wilhelms-Universität Münster, (2013) (cit. on p. 50).

[KAT] The KATRIN Collaboration. *KATRIN Wiki - Resources*. https://ikp-katrin-wiki.ikp.kit.edu/katrin/index.php/Resources. Internal, Accessed: 2022-04-13 (cit. on p. 9).

[KAT22] The KATRIN Collaboration. “Direct neutrino-mass measurement with sub-electronvolt sensitivity”. In: *Nature Physics* 18.2 (2022), pp. 160–166. ISSN: 1745-2481. DOI: 10.1038/s41567-021-01463-1 (cit. on pp. 1, 9, 16, 17).

[Kle+19] M Kleesiek et al. “β-Decay spectrum, response function and statistical model for neutrino mass measurements with the KATRIN experiment”. In: *The European Physical Journal C* 79.3 (2019), pp. 1–24. DOI: 10.1140/epjc/s10052-019-6686-7 (cit. on p. 16).

[Kod+01] K Kodama et al. “Observation of tau neutrino interactions”. In: *Physics Letters B* 504.3 (2001), pp. 218–224. DOI: 10.1016/S0370-2693(01)00307-0 (cit. on p. 4).

[Kod+08] K Kodama et al. “Final tau-neutrino results from the DONuT experiment”. In: *Physical Review D* 78.5 (2008), p. 052002. DOI: 10.1103/PhysRevD.78.052002 (cit. on p. 4).

[Kön21] T König. “Simulations and measurements of angular selective electron transmission and detection for the KATRIN experiment”. Bachelor’s Thesis. Institut für Kernphysik - Westfälische Wilhelms-Universität Münster, (2021) (cit. on pp. 23, 49).

[Kra+05] Ch Kraus et al. “Final results from phase II of the Mainz neutrino mass searchin tritium β decay”. In: *The European Physical Journal C-Particles and Fields* 40.4 (2005), pp. 447–468. DOI: 10.1140/epjc/s2005-02139-7 (cit. on pp. 1, 9, 12).

[Lok+22] A Lokhov et al. “Background reduction at the KATRIN experiment by the shifted analysing plane configuration”. In: *The European Physical Journal C* 82.3 (2022), pp. 1–11. DOI: 10.1140/epjc/s10052-022-10220-4 (cit. on pp. 17, 19).

[Lu+20] H Lu et al. “Recent results from Daya Bay reactor neutrino Experiment”. In: *Journal of Physics: Conference Series*. Vol. 1342. 1. IOP Publishing. (2020), p. 012032. DOI: 10.1088/1742-6596/1342/1/012032 (cit. on p. 6).

[Mac20] MB Machatschek. “A phenomenological theory of KATRIN source potential systematics and its application in krypton-83m calibration measurements”. PhD thesis. Karlsruher Institut für Technologie (KIT), (2020) (cit. on pp. 1, 18).

[Mar+21] A Marsteller et al. “Neutral tritium gas reduction in the KATRIN differential pumping sections”. In: *Vacuum* 184 (2021), p. 109979. DOI: 10.1016/j.vacuum.2020.109979 (cit. on p. 12).

[MNS62] Z Maki, M Nakagawa, and S Sakata. "Remarks on the unified model of elementary particles". In: *Progress of Theoretical Physics* 28.5 (1962), pp. 870–880. DOI: 10.1143/PTP.28.870 (cit. on p. 5).

[Nc+12] A Nucciotti, MARE collaboration, et al. "Neutrino mass calorimetric searches in the MARE experiment". In: *Nuclear Physics B-Proceedings Supplements* 229 (2012), pp. 155–159. DOI: 10.1016/j.nuclphysbps.2012.09.025 (cit. on p. 8).

[Nob15] Nobelprize.org. *The Nobel Prize in Physics 2015 – Press Release*. Accessed: 2022-04-13. 2015. URL: https://www.nobelprize.org/prizes/physics/2015/press-release/ (cit. on p. 1).

[Nob95] Nobelprize.org. *The Nobel Prize in Physics 1995 – Press Release*. Accessed: 2022-04-13. 1995. URL: https://www.nobelprize.org/prizes/physics/1995/press-release/ (cit. on p. 1).

[Nor63] TG Northrop. "Adiabatic charged-particle motion". In: *Reviews of Geophysics* 1.3 (1963), pp. 283–304. DOI: 10.1029/RG001i003p00283 (cit. on p. 15).

[NT60] TG Northrop and E Teller. "Stability of the adiabatic motion of charged particles in the earth's field". In: *Physical Review* 117.1 (1960), p. 215. DOI: 10.1103/PhysRev.117.215 (cit. on p. 15).

[Nuc+18] A Nucciotti et al. "Status of the HOLMES experiment to directly measure the neutrino mass". In: *Journal of Low Temperature Physics* 193.5 (2018), pp. 1137–1145. DOI: 10.1007/s10909-018-2025-x (cit. on p. 8).

[Oel21] P Oelpmann. "Angular selective electron detection using microchannel plates for a possible background reduction at the KATRIN experiment". MA thesis. Institut für Kernphysik - Westfälische Wilhelms-Universität Münster, (2021) (cit. on pp. 23, 49).

[OW08] EW Otten and C Weinheimer. "Neutrino mass limit from tritium β decay". In: *Reports on Progress in Physics* 71.8 (2008), p. 086201. DOI: 10.1088/0034-4885/71/8/086201 (cit. on p. 24).

[Pau64] W Pauli. "Offener Brief an die Gruppe der Radioaktiven bei der Gauvereinstagung zu Tübingen (4. Dez. 1930)". In: *R. Kronig and V. Weisskopf, Collected Scientific Papers* 2 (1964), p. 1316. URL: https://cds.cern.ch/record/83282/files/meitner_0393.pdf (cit. on pp. 1, 3).

[Per+75] ML Perl et al. "Evidence for anomalous lepton production in e^+-e^- annihilation". In: *Physical Review Letters* 35.22 (1975), p. 1489. DOI: 10.1142/9789812795816_0006 (cit. on p. 4).

[Pon58] B Pontecorvo. “Mesonium and antimesonium”. In: *Soviet Journal of Experimental and Theoretical Physics* 6 (1958), p. 429 (cit. on p. 5).

[RC53] F Reines and CL Cowan Jr. “Detection of the free neutrino”. In: *Physical Review* 92.3 (1953), p. 830. DOI: 10.1103/PhysRev.92.830 (cit. on p. 3).

[Rob19] RGH Robertson. *Transverse Energy Filter*. Internal report. June 2019 (cit. on p. 22).

[Rod+22] C Rodenbeck et al. “Wideband precision stabilization of the 18.6 kV retarding voltage for the KATRIN spectrometer”. In: *arXiv preprint arXiv:2203.13153* (2022). DOI: 10.48550/ARXIV.2203.13153 (cit. on p. 17).

[Sac20] R Sack. “Measurement of the energy loss of 18.6 keV electrons on deuterium gas and determination of the tritium Q-value at the KATRIN experiment”. PhD thesis. Institut für Kernphysik - Westfälische Wilhelms-Universität Münster, (2020) (cit. on pp. 19, 28).

[Sal+21] PF de Salas et al. “2020 global reassessment of the neutrino oscillation picture”. In: *Journal of High Energy Physics* 2021.2 (2021), pp. 1–36. DOI: 10.1007/JHEP02(2021)071 (cit. on pp. 6, 7).

[Sal19] RWJ Salomon. “Development of a Setup to test Time-Of-Flight Methods for the KATRIN Experiment”. Bachelor’s Thesis. Institut für Kernphysik - Westfälische Wilhelms-Universität Münster, (2019) (cit. on pp. 27, 33, 34, 49, 63).

[Sch+21] S Schneidewind et al. “E-Gun characterisation at the monitor spectrometer, July 2021 - Results”. Internal document. 2021 (cit. on pp. 46, 48).

[Sch21] L Schimpf. “Characterisation of energy loss processes of 18.6 keV electrons inside the windowless tritium source of KATRIN”. PhD thesis. Karlsruher Institut für Technologie (KIT), (2021) (cit. on p. 13).

[Ste+13] N Steinbrink et al. “Neutrino mass sensitivity by MAC-E-Filter based time-of-flight spectroscopy with the example of KATRIN”. In: *New Journal of Physics* 15.11 (2013), p. 113020. DOI: 10.1088/1367-2630/15/11/113020 (cit. on p. 49).

[Tan+18] M Tanabashi et al. “Review of particle physics”. In: *Physical Review D* 98.3 (2018), pp. 390–395. DOI: 10.1016/j.physletb.2008.07.018 (cit. on p. 7).

[Tho13] M Thomson. *Modern particle physics*. Cambridge University Press, 2013, pp. 343–346. DOI: 10.1017/CBO9781139525367 (cit. on p. 6).

[Tro18] N Trost. “Modeling and measurement of Rydberg-State mediated Background at the KATRIN Main Spectrometer”. PhD thesis. Karlsruher Institut für Technologie (KIT), (2018) (cit. on pp. 2, 18, 22, 24).

[Vir+20] P Virtanen et al. “SciPy 1.0: Fundamental Algorithms for Scientific Computing in Python”. In: *Nature Methods* 17 (2020), pp. 261–272. DOI: 10.1038/s41592-019-0686-2 (cit. on pp. 37, 56).

[Zac15] M Zacher. “High-field electrodes design and an angular-selective photoelectron source for the KATRIN spectrometers”. PhD thesis. Institut für Kernphysik - Westfälische Wilhelms-Universität Münster, (2015) (cit. on p. 33).

Acknowledgments

Zuallererst möchte ich mich für die Betreuung dieser Arbeit bei Professor Christian Weinheimer bedanken.
Außerdem gilt mein Dank Professor Anton Andronic, der sich bereit erklärt hat, diese Arbeit als Zweitprüfer zu bewerten.

Mein ganz besonderer Dank gilt meiner Betreuerin Sonja Schneidewind, die sich wochen- wie feiertags, Tag und Nacht Zeit für meine Fragen nahm und sie in besonderer Ausführlichkeit beantwortete. Sie hat mich immer wieder unterstützt, selbstständig zu arbeiten und meine eigenen Entscheidungen zu treffen. Auch beim Korrekturlesen dieser Arbeit war ihre Hilfe von unschätzbarem Wert.
Ein ebenso großes Dankeschön geht an meinen Zweitbetreuer Kevin Gauda. Auch ihn konnte ich jederzeit mit Fragen löchern. Besonders genossen habe ich die Kaffeepausen, die einen auf andere Gedanken bringen konnten und auch sehr häufig angeregte Diskussionen zur Folge hatten. Auch ihm bin ich sehr dankbar, dass er sich ausführlichst Zeit genommen hat, diese Arbeit Kontrolle zu lesen.
Weiterhin möchte ich mich bei Volker Hannen und Alexey Lokhov bedanken, die immer ein offenes Ohr für mich hatten und mir in Vorbereitung auf zahlreiche Vorträge mit Rat und Tat beiseite standen. Besonders Volker machte es mir sehr einfach möglich (besonders am Anfang meiner Masterarbeit), in Zeiten der Corona Pandemie meine Arbeit von zuhause aus durchzuführen.
Nicht vergessen möchte ich Benedikt Bieringer, der mir bei allerlei Computer bezogenen Fragen immer weiterhelfen konnte. Auch die allgemeinen Gespräche im Büro haben immer sehr viel Spaß gemacht.

Zu guter Letzt möchte ich mich ganz speziell bei meinen Eltern und meiner Freundin Cassandra bedanken. Ihre liebevolle Unterstützung ist unvergleichbar. Dafür werde ich ewig dankbar sein.